NASA Contractor Report 3643

Assessment of Turbulence Models for Scramjet Flowfields

M. M. Sindir and P. T. Harsha

CONTRACT NAS1-15988
NOVEMBER 1982

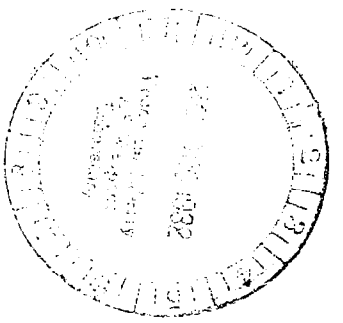

NASA

NASA Contractor Report 3643

Assessment of Turbulence Models for Scramjet Flowfields

M. M. Sindir and P. T. Harsha
Science Applications, Inc.
Chatsworth, California

Prepared for
Langley Research Center
under Contract NAS1-15988

NASA
National Aeronautics
and Space Administration

Scientific and Technical
Information Branch

1982

TABLE OF CONTENTS

TABLE OF CONTENTS, Contd.

LIST OF FIGURES

LIST OF FIGURES (Continued)

LIST OF FIGURES (Continued)

LIST OF FIGURES (Continued)

LIST OF TABLES

1. INTRODUCTION

In order to provide turbulence models useful for computations of the flowfields involved in advanced scramjet combustion systems, a number of features of these flowfields must be considered. These combustion systems involve supersonic flows with embedded subsonic regions and recirculation zones, and appropriate turbulence models for scramjet applications must address each of these. The geometry of advanced combustors is often three-dimensional, so that the effects of three-dimensionality in the flowfield on the turbulence characteristics must be taken into account. Moreover, the combustion process in a scramjet system is embedded within a highly turbulent flow, so that the effects of turbulence on chemical reaction rates must be considered, particularly, in the scramjet context, with respect to ignition phenomena. On the other hand, to be of maximum utility in scramjet combustor design, the turbulence modeling should be as simple and straightforward as is consonant with the requirements of overall accuracy. In this application, predictions of mean flowfield structure, the effects of heat release, and mean chemical reaction rates are of greatest importance: details of the turbulence structure itself can be approximated if the approximations introduced do not materially affect the prediction of overall mixing rate, chemical reaction rate, and parameters such as the wall skin friction distribution and flowfield pressure gradient. Since it can be expected that different effects may dominate in different regions of the flow: non-isotropy in recirculation regions; compressibility effects in high speed flow regions; and turbulence-chemistry interaction effects in regions in which fuel ignition is occurring, a modular approach may be the most efficient turbulence model overall. In such an approach, each module contains the turbulence model elements which best account for the dominant features of each region of the flowfield.

An assessment of turbulence models for scramjet applications was initiated in September 1979. During the first year of this work, as outlined in Ref. 1, the major effort involved the examination of the multiple dissipation length scale (MDLS) turbulence model, since this approach appeared to offer the

potential for greater generality than existing models in the context of scramjet-related flowfields. In addition to this work, other efforts carried out during the first year of this program included the definition of a technique for the estimation of the initial conditions required by field-equation turbulence models (Ref. 1), an examination of the use of a modified dissipation rate equation with the basic k-ε two-equation turbulence model (Refs. 1, 2), and the development of a supersonic-flow compressibility correction to the dissipation rate equation in the two-equation (or MDLS) approach (Refs. 1, 3).

Although the results of Ref. 1 indicated that the MDLS model is slightly more general than the basic k-ε model, the gain is not worth the added cost of solving two additional equations. Furthermore, the flowfields considered in the analyses reported in Ref. 1, while fundamental to and underlying many of the structures found in scramjet flows, did not involve large scale recirculation regions where the effects of stress nonisotropy become important. Accordingly, the focus of the second year's work shifted to an assessment of the performance of a variety of turbulence models in low-speed and high-speed recirculating flows. Thus, in the work described in this report, several turbulence models, including the basic two-equation model, the MDLS variant of the two-equation approach, and the algebraic stress model (ASM) first reported by Rodi (Ref. 4) and further developed by Sindir (Ref. 5) have been applied to the prediction of both supersonic jet and supersonic shear layer flows.

In complex flowfields it is difficult to separate some aspects of the turbulence modeling problem from the numerical problems inherent in different computational approaches for solving the governing equations describing the flow. These aspects include the treatment of wall boundary conditions, the algorithms used to generate the finite-difference form of the equations, and the algorithms used to provide the finite-difference solution of the governing equations for the particular turbulence model chosen. While not an integral part of the work carried out under the present program, several such problems were encountered and are discussed.

The basic features of the different turbulence models investigated during the current phase of the turbulence modeling assessment program are outlined in the next section. These models include the basic two-equation k-ε formulation,

the MDLS variant of the two-equation approach, the algebraic stress model (ASM), and modified versions of the k-ε and ASM approaches. Details of the formulation of each of these models are included in appendices. Following a description of the models, results of the work carried out to assess the performance of the models are given in Section 3. The discussion includes observations with respect to the interaction of the turbulence models with different numerical solution techniques. These techniques include a stream-function/vorticity approach for the computation of axisymmetric incompressible recirculating flows and a time-split MacCormack technique for planar supersonic recirculating flows. Comparisons of the predictions of different turbulence models with data and with each other are presented for both planar and axisymmetric low-speed recirculating flows. Also comparisons of the performance of a two-equation model with different eddy viscosity models are presented for a high-speed recirculating flow. Following this, conclusions drawn from the work described in this report are stated, and work planned to continue the turbulence modeling assessment and definition is outlined in Section 4.

NOMENCLATURE

A	area of control volume surface
A_τ	area through which the wall stress is applied
a	$-\overline{uv}/k$ (equation (17)); $k_p - ((k_p - k_E)/(y_p - y_E))y_p$ (equation (45)); coefficient in equation (73)
a_1, a_2	coefficients in equations (68) to (71)
b	exponent in equation (73)
c_1	coefficient in modeled form of $\phi_{ij,1}$ (equation (11))
c_2	coefficient in modeled form of $\phi_{ij,2}$ (equation (14))
c_1'	coefficient in modeled form of $\phi_{ij,1}'$ (equation (15))
c_2'	coefficient in modeled form of $\phi_{ij,2}'$ (equation (16))
c_2''	coefficient in equation (13)
c_f	skin friction coefficient, $\tau_w/0.5\ \rho\ U_{in}^2$
c_ℓ	coefficient in equation (44)
c_k	coefficient in modeled form of $\overline{u_i^2 u_j}$ (equation (25))
c_{P_1}	coefficient in equation (34)
c_{P_1}'	coefficient in equation (72)
c_{P_2}	coefficient in equation (34)
c_s	coefficient in equation (20)
c_s'	coefficient in equation (19)
c_{T_1}	coefficient in equation (34)
c_{T_2}	coefficient in equation (34)
c_μ	coefficient in equation (24)
c_{ε_1}	coefficient in modeled production term of ε (equation (30))
c_{ε_2}	coefficient in modeled destruction term of ε (equation (30))

c_{ε_3}	coefficient in modeled form of $\overline{\nu u_k (\partial u_i/\partial x_j)^2}$ (equation (30))
D	material derivative; also jet diameter
D_e	diameter of inlet flowfield, sudden expansion configuration
D_{ij}	term in modeled form of $\phi_{ij,2}$ (equation (13))
D	diffusive transport of (equation (22))
E	coefficient in logarithmic law of the wall
E*	exp $(\kappa^* Re_v)/Re_v$ (equation (40))
e	normalized anisotropies of Reynolds stresses, $(\overline{u_i u_j} - 2/3\delta_{ij}k)/k$ (equations (68) to (71))
f	length-scale function (equations (17) and (18))
h	distance of separation between two parallel walls (equation (18)); also step height
k	turbulent kinetic energy
k_P	production region turbulent kinetic energy
k_T	transfer region turbulent kinetic energy
ℓ	characteristic turbulence length scale
M	Mach number
n	unit normal vector
P	static pressure
P	production rate of turbulent kinetic energy (equation (23))
P_k	production rate of turbulent kinetic energy (equation (38))
P_{ij}	production rate of Reynolds stress tensor (equation (23))
p	instantaneous pressure fluctuations
R_o	radius of pipe before expansion
R_1	radius of pipe after expansion
Re	Reynolds number

Re_v	viscous sublayer Reynolds number (taken as a constant = 20)
r	position vector; also polar radius in axisymmetric flows
t	time
U	streamwise mean velocity
U_c	streamwise mean velocity along flowfield centerline
U_i	time averaged velocity component (i=1,2,3)
$\tilde{U}_i$	instantaneous velocity component (i=1,2,3)
U_{in}	maximum inlet velocity
U_o	streamwise mean velocity at dump plane (inlet velocity)
U_τ	friction velocity $\sqrt{\tau_w/\rho}$
$\overline{u^2}$	streamwise component of Reynolds normal stress
u_i	instantaneous velocity fluctuations
$\overline{u_i u_j}$	time-averaged components of Reynolds stress
$\overline{u_i u_j u_k}$	time-averaged triple velocity correlations
V	transverse mean velocity
$\overline{v^2}$	transverse component of Reynolds normal stress
$\overline{w^2}$	lateral component of Reynolds normal stress
x	streamwise distance
x_i	displacement vector
y	transverse distance

Greek Symbols

α	weighting factor in equation (8)
Γ	$2/3\rho k^2/\varepsilon$ (equations (68) to (71))
δ_{ij}	Kronecker delta
ε	dissipation rate of turbulent kinetic energy

ε_p	production region dissipation rate
ε_T	transfer region dissipation rate
ε_{ij}	dissipation rate tensor of Reynolds stresses
$\bar{\varepsilon}$	mean dissipation rate for near-wall kinetic energy budget (equation (45))
κ	the von Karman constant; also wave number
κ^*	$\kappa c_\mu^{1/4}$
λ	coefficient in algebraic stress formulation (equations (68) to (71))
λ_ε	coefficient in equation (45)
μ	dynamic viscosity of fluid
μ_t	turbulent viscosity
μ_T	total viscosity, $\mu_t + \mu$
ν	kinematic viscosity of fluid
ρ	density of fluid
σ	spreading parameter for jets
σ_k	Prandtl number for k transport equation (equation (26))
σ_ε	Prandtl number for ε transport equation (equation (31))
τ	shear stress
$\phi_{ij,1}$	fluctuating velocity part of pressure-strain correlation (equation (11))
$\phi_{ij,2}$	mean strain part of pressure-strain correlation (equation (14))
$\phi_{ij,1}'$	near-wall correction to $\phi_{ij,1}$ (equation (15))
$\phi_{ij,2}'$	near-wall correction to $\phi_{ij,2}$ (equation (16))
$\phi_{ij,w}$	near-wall effects in the pressure-strain correlation (equation (10))

ψ	stream function
Ω	vorticity

Subscripts

E	value at the node east of P
e	value at the cell boundary between E and P
N	value at the node north of P
P	value at the node where the control volume is centered
r	radial direction
S	value at the node south of P
T	total
t	turbulent
u	streamwise direction normal stress
uv	streamwise direction shear stress
v	value at the edge of the viscous sublayer; or transverse direction
W	value at the node west of P
w	value at the wall; or lateral direction normal stress
x	streamwise direction
y	transverse direction

2. FLOW EQUATIONS AND TURBULENCE MODELS

In this section, the theoretical framework used in the turbulent flow calculations is outlined. This is accomplished in ten subsections: Section 2.1 presents the mean flow equations and discusses the consequences of Reynolds time averaging; Section 2.2 introduces the Reynolds stress transport equation and summarizes the modeling efforts at this level of closure; Sections 2.3 and 2.4 present alternative closure schemes via the algebraic stress and k-ε models, respectively, and compare the relative advantages and drawbacks of each model; Sections 2.5 and 2.6 introduce, respectively, the k and ε transport equations and the derivation of the modeled forms of these equations for high Reynolds number flows; Section 2.7 discusses the modifications introduced to the ε transport equation; Section 2.8 provides a review of the multiple-dissipation length scale approach; Section 2.9 presents a new non-equilibrium wall-function treatment for near-wall velocity profiles, turbulent kinetic energy budgets and dissipation rates; and Section 2.10 gives the two-dimensional forms of the mean flow and turbulence model equations used in the computations.

2.1 MEAN FLOW EQUATIONS AND REYNOLDS TIME AVERAGING

The equations of motion in the absence of external force fields take the following tensorial form for uniform-density Newtonian fluids:

$$\frac{\partial \tilde{U}_i}{\partial t} + \frac{\partial}{\partial x_j} \tilde{U}_i \tilde{U}_j = - \frac{1}{\rho} \frac{\partial \tilde{P}}{\partial x_i} + \frac{\partial}{\partial x_j} \left[\frac{\mu}{\rho} \left(\frac{\partial \tilde{U}_i}{\partial x_j} + \frac{\partial \tilde{U}_j}{\partial x_i} \right) \right] \tag{1}$$

where $\tilde{U}_i$ is the component of instantaneous velocity in the x_i direction, $\tilde{P}$ is the static pressure, and ρ and μ are the fluid density and dynamic viscosity, respectively. These three equations coupled with the conservation of mass principle

$$\frac{\partial \tilde{U}_i}{\partial x_i} = 0 \tag{2}$$

form the Navier-Stokes equations that predict the dynamic behavior of turbulent as well as laminar flows. However, practical turbulent flows contain a cascade

of eddy sizes that represent a wide range of time and length scales. Hence any numerical scheme using equations (1) and (2) for turbulent flow simulations would require a grid fine enough to resolve even the smallest turbulent motions. This, at least with the current generation of digital computers, is not possible for the solution of practical problems. Since a description of the instantaneous flowfield is beyond our present computing capability, a good compromise would seem to be prediction of a mean flowfield which is either "time" or "ensemble" averaged. This approach, first proposed by Osborne Reynolds in the late 19th century, is the starting point for most of today's applied turbulence work.

Reynolds suggested a statistical average of the instantaneous velocity $\tilde{U}_i$ with respect to time such that

$$U_i \equiv \lim_{T \to \infty} \frac{1}{2T} \int_{-T}^{T} \tilde{U}_i \, dt \tag{3}$$

where T is a time interval which is long compared with the largest turbulence time scales, but shorter than the period over which the averaged flow quantities may vary. Inherent in this definition is the idea that the instantaneous velocity $\tilde{U}_i$ (or by the same token any other flow variable) can be divided into a mean, U_i, and a fluctuating component, u_i, as

$$\tilde{U}_i \equiv U_i + u_i \tag{4}$$

It follows, on taking the average of each side of (4), that the mean of the fluctuating component is identically zero

$$\lim_{T \to \infty} \frac{1}{2T} \int_{-T}^{T} u_i \, dt \equiv 0$$

Substituting definition (4) and its counterpart for the static pressure $\tilde{P}(\tilde{P} = P + p)$ into the instantaneous flow equations (1), and time averaging as shown in (3) leads to the mean flow equation known as the Reynolds equation

$$\frac{\partial U_i}{\partial t} + \frac{\partial U_j U_i}{\partial x_j} = -\frac{1}{\rho}\frac{\partial P}{\partial x_i} + \frac{\partial}{\partial x_j}\left[\frac{\mu}{\rho}\left(\frac{\partial U_i}{\partial x_j} + \frac{\partial U_j}{\partial x_i}\right) - \overline{u_i u_j}\right] \tag{5}$$

The only difference between the instantaneous flow equations and the Reynolds equation is the appearance of the fluctuating velocity correlation tensor, $\overline{u_i u_j}$ defined as

$$\overline{u_i u_j} \equiv \lim_{T \to \infty} \frac{1}{2T} \int_{-T}^{T} u_i u_j \, dt$$

This term, generally known as the Reynolds or turbulent stress, is actually the fluctuating velocity counterpart of the mean velocity local acceleration term $\partial U_j U_i / \partial x_j$. However, it is traditionally taken to the right-hand side and interpreted as a stress rather than an acceleration term. In this form this term completely overwhelms its viscous counterpart in most turbulent flows and becomes the sole mechanism for diffusive momentum transport. The Reynolds equation coupled with the time-averaged form of the continuity equation (2)

$$\frac{\partial U_i}{\partial x_i} = 0 \tag{6}$$

now becomes the governing set of equations for turbulent momentum transfer. This set of equations, however, is not "closed" due to the appearance of the Reynolds stress tensor $\overline{u_i u_j}$ which introduces six additional unknowns to raise the total number of variables in the four equations to ten (U_i, P, $\overline{u_i u_j}$). Thus additional relationships need to be developed to express $\overline{u_i u_j}$ in terms of known or calculable variables. These efforts constitute the subject of turbulence modeling.

2.2 REYNOLDS STRESS TRANSPORT EQUATION

An equation governing the transport of Reynolds stress, $\overline{u_i u_j}$, can be derived from the Navier-Stokes equations for a fluid of uniform properties and no external force fields by multiplying equation (1) by u_j and adding to it the same equation with suffixes i and j interchanged. Time averaging the resultant gives

$$\frac{\partial \overline{u_i u_j}}{\partial t} + U_k \frac{\partial \overline{u_i u_j}}{\partial x_k} = -\left\{ \overline{\partial u_i u_k} \frac{\partial U_j}{\partial x_k} + \overline{u_j u_k} \frac{\partial U_i}{\partial x_k} \right\} \quad \text{II}$$

$$\text{I} \qquad - 2\nu \overline{\frac{\partial u_i}{\partial x_k} \frac{\partial u_j}{\partial x_k}} - \nu \left(\overline{\frac{\partial u_i}{\partial x_k} \frac{\partial u_k}{\partial x_j}} + \overline{\frac{\partial u_j}{\partial x_k} \frac{\partial u_k}{\partial x_i}} \right) \quad \text{III}$$

$$+ \overline{\frac{p}{\rho} \left(\frac{\partial u_i}{\partial x_j} + \frac{\partial u_j}{\partial x_i} \right)} \quad \text{IV} \qquad (7)$$

$$- \frac{\partial}{\partial x_k} \left\{ \overline{u_i u_j u_k} + \delta_{jk} \frac{\overline{u_i p}}{\rho} + \delta_{ik} \frac{\overline{u_j p}}{\rho} \right.$$

$$\left. - \nu \left(\frac{\partial \overline{u_i u_j}}{\partial x_k} + \overline{u_j \frac{\partial u_k}{\partial x_i}} + \overline{u_i \frac{\partial u_k}{\partial x_j}} \right) \right\} \quad \text{V}$$

where p is the fluctuating component of the static pressure $\tilde{P}$ and the δ's are Kronecker deltas.

Equation (7) representing the transport of Reynolds stresses along a mean streamline can be divided into the five different terms shown above. Some of these terms are "exact" in the sense that they are expressed only in terms of the stresses and the mean strain rate, and thus do not require modeling (terms I and II); others, however, need to be modeled because they either include higher-order correlations (term V) or correlations between turbulence quantities that are not known or calculable (terms III, IV, and V). The goal of this section is to discuss each of these terms separately and provide the modeled forms, when needed, to lay the groundwork for the algebraic stress model, which is a special case of this transport equation.

A. Convective Transport, Term I

This term expresses the rate of change of the Reynolds stresses $\overline{u_i u_j}$ along a mean streamline. It is composed of a temporal change, $\partial \overline{u_i u_j}/\partial t$, and a local acceleration, $U_k \, \partial \overline{u_i u_j}/\partial x_k$, both of which contain only the stresses and the mean flowfield, and thus require no modeling. The temporal term represents a time-dependent variation over a period much longer than the interval used in the time-averaging and vanishes in a statistically stationary flow.

B. Production, Term II

This term represents the rate of generation of the Reynolds stress $\overline{u_i u_j}$ through the interaction of the stress with the mean strain rate. Since turbulence needs a continuous input of energy to maintain itself, this then can also be regarded as the energy drain from the mean flow to turbulence. Usually given the symbol P_{ij}, this term acts like a source in the $\overline{u_i u_j}$ transport equation and requires no modeling.

C. Viscous Dissipation, Term III

This term represents the destruction of the Reynolds stress correlation $\overline{u_i u_j}$ through viscous action. Being negative definite it behaves like a sink and couterbalances the gains in the level of $\overline{u_i u_j}$ due to the production P_{ij}. Traditionally expressed as ε_{ij} this term includes correlations between various fluctuating velocity gradients that are neither known or calculable. So far only two workable proposals have been made for modeling this term; both of these express ε_{ij} in terms of the dissipation rate of turbulent kinetic energy ε (which is the contracted form ($i = j$) of ε_{ij}) given as $\nu \overline{\partial u_i/\partial x_k (\partial u_i/\partial x_k + \partial u_k/\partial x_i)}$. Each proposal makes certain assumptions with respect to the character of the dissipating eddies in modeling ε_{ij}; therefore, depending on the nature of the flow one or the other of the proposals (or even a combination of them) may be desirable. The first proposal, by Daly and Harlow (Ref. 6), and Donaldson (Ref. 7), assumes that the dissipating motions have the same structure as the energy containing eddies (a hypothesis plausible for low Reynolds number flows), and relates ε_{ij} to ε through the coefficient $\overline{u_i u_j}/k$. The second proposal, first suggested by Rotta (Ref. 8), assumes that dissipating motions, at least for high Reynolds number flows, are isotropic in character and can be expressed as $2/3\delta_{ij}\varepsilon$. A more general representation is a combination of both proposals such as

$$\varepsilon_{ij} = \alpha 2/3\ \delta_{ij}\ \varepsilon + (1 - \alpha)\ \frac{\overline{u_i u_j}}{k}\ \varepsilon \qquad (8)$$

where α is assigned values between 0 and 1 depending on the nature of the flow, e.g., $\alpha = 1$ for high Reynolds number flows. It can also be shown that for high Reynolds number flows the term

$$\nu\left(\overline{\frac{\partial u_i}{\partial x_k}\frac{\partial u_k}{\partial x_j}} + \overline{\frac{\partial u_j}{\partial x_k}\frac{\partial u_k}{\partial x_i}}\right)$$

is negligibly small so that ε_{ij} and ε reduce to

$2\nu\,\overline{\frac{\partial u_i}{\partial x_k}\frac{\partial u_j}{\partial x_k}}$ and $2\nu\overline{\left(\frac{\partial u_i}{\partial x_k}\right)^2}$, respectively.

D. Pressure-Strain Correlation, Term IV

This term plays an influential role in the Reynolds stress transport equation and has to be modeled with care. The primary function of this correlation is to change the relative levels of the normal stresses, and to act as a source (or a sink) in the shear stress equations. Since it makes no direct contribution to the level of turbulence energy but merely redistributes it among the normal stresses, it is called a "redistributive" term.

The first step in modeling this correlation is to establish a Poisson equation for the fluctuating pressure. Following Chou (Ref. 9) this is done by taking the divergence $\partial/\partial x_\ell$ of the transport equation for u_ℓ:

$$\frac{\partial}{\partial x_\ell}\left\{\frac{\partial u_\ell}{\partial t} + U_m\frac{\partial u_\ell}{\partial x_m} = -\frac{1}{\rho}\frac{\partial P}{\partial x_\ell} - u_m\frac{\partial U_\ell}{\partial x_m} + \nu\frac{\partial^2 u_\ell}{\partial x_m^2} - \frac{\partial}{\partial x_m}\left(u_\ell u_m - \overline{u_\ell u_m}\right)\right\} \qquad (9)$$

and imposing the fluctuating velocity continuity constraint $\partial u_\ell/\partial x_\ell \equiv 0$ to obtain the Poisson equation

$$\frac{1}{\rho}\frac{\partial^2 P}{\partial x_\ell^2} = -2\frac{\partial u_m}{\partial x_\ell}\frac{\partial U_\ell}{\partial x_m} - \frac{\partial^2}{\partial x_\ell \partial x_m}\left(u_\ell u_m - \overline{u_\ell u_m}\right)$$

Integrating this equation over a region of fluid, multiplying by $(\partial u_i/\partial x_j + \partial u_j/\partial x_i)$ and time averaging yields the following expression for the pressure-strain correlation:

$$\frac{p}{\rho}\left(\overline{\frac{\partial u_i}{\partial x_j}+\frac{\partial u_j}{\partial x_i}}\right)=\frac{1}{4\pi}\int_{vol}\left\{\overline{\left(\frac{\partial^2 u_\ell u_m}{\partial x_\ell \partial x_m}\right)'\left(\frac{\partial u_i}{\partial x_j}+\frac{\partial u_j}{\partial x_i}\right)}+2\,\frac{\partial U'_\ell}{\partial x_m}\,\overline{\frac{\partial u'_m}{\partial x_\ell}\left(\frac{\partial u_i}{\partial x_j}+\frac{\partial u_j}{\partial x_i}\right)}\right\}\frac{dV}{\bar{r}}$$

$\phi_{ij,1}$ $\phi_{ij,2}$

$$+\frac{1}{4\pi}\int_{Area}\left\{\frac{1}{\vec{r}}\frac{\partial}{\partial n'}\,\overline{p'\left(\frac{\partial u_i}{\partial x_j}+\frac{\partial u_j}{\partial x_i}\right)}-\overline{p'\left(\frac{\partial u_i}{\partial x_j}+\frac{\partial u_j}{\partial x_i}\right)}\frac{\partial}{\partial n'}\,\frac{1}{\vec{r}}\right\}dS \qquad (10)$$

$\phi_{ij,w}$

where dV and dS denote, respectively, volume and surface elements about the given point, and $\partial/\partial n$ is the normal derivative at the surface. Prime superscripts indicate quantities evaluated at a distance r from the given point. This representation of the pressure-strain correlation can be broken down into three contributing terms. These are: $\phi_{ij,1}$ resulting from purely turbulence interactions, $\phi_{ij,2}$ involving interactions between the mean strain rate and turbulence, and $\phi_{ij,w}$ representing the effects of rigid boundaries on both $\phi_{ij,1}$ and $\phi_{ij,2}$. Modeling of the pressure-strain correlation thus reduces to the modeling of each of these terms, as summarized below. The constants appearing in the various models are given in Table 2.1, page 19.

Modeling of $\phi_{ij,1}$: The term $\phi_{ij,1}$ has long been identified as the only mechanism in the stress transport equation (7) that could promote a return to a state of isotropy. This can be best observed for decaying turbulence where there is no appreciable mean strain, and the only term left in equation (7) that could equalize the normal stress components and reduce the shear stress is $\phi_{ij,1}$. Also, when isotropic two-point correlations are substituted into the definition of $\phi_{ij,1}$ (equation 10), this term vanishes, providing further evidence of its function as a promoter of isotropy. The following linear form for $\phi_{ij,1}$ was first proposed in Ref. 8:

$$\phi_{ij,1}=-c_1\,\frac{\varepsilon}{k}\left(\overline{u_i u_j}-\frac{2}{3}\,\delta_{ij}k\right) \qquad (11)$$

where ε/k defines a time scale and c_1 is a constant to be determined from experiment. This simple linear form for $\phi_{ij,1}$ is widely accepted and used

despite the fact that, as shown by Bradshaw (Ref. 10), the actual "return to isotropy" process is highly non-linear. More sophisticated non-linear forms such as Lumley and Khajeh Nouri's proposal (Ref. 11) have been suggested, but these have shown no significant improvement over Rotta's proposal.

Modeling of $\phi_{ij,2}$: This term in the pressure-strain correlation represents the interactions between the mean strain rate and turbulence. Rotta (Ref. 8) obtained a simpler form by assuming symmetry properties for the two-point correlations and treating the mean velocity gradient $\partial U_\ell / \partial x_m$ as constant over the region of integration:

$$\phi_{ij,2} = -\frac{1}{2\pi} \frac{\partial U_\ell}{\partial x_m} \int \left[\frac{\overline{\partial^2 u_m' u_i}}{\partial r_\ell \partial r_j} + \frac{\overline{\partial^2 u_m' u_j}}{\partial r_\ell \partial r_i} \right] \frac{dV}{\vec{r}} \tag{12}$$

where r_ℓ and r_j are the Cartesian components of the position vector $\vec{r}$. A workable modeled form for this term was first devised by Launder (Ref. 12) and then further refined by Naot, Shavit and Wolfshtein (Ref. 13), and Launder, Reece, and Rodi (Ref. 14), who, working independently and using different analytical techniques, obtained the same expression for $\phi_{ij,2}$:†

$$\phi_{ij,2} = -\frac{(c_2'' + 8)}{11} (P_{ij} - \tfrac{2}{3} \delta_{ij} P) - \frac{(30\, c_2'' - 2)}{55} k \left(\frac{\partial U_i}{\partial x_j} + \frac{\partial U_j}{\partial x_i} \right)$$

$$- \frac{(8\, c_2'' - 2)}{11} (D_{ij} - \tfrac{2}{3} \delta_{ij} P) \tag{13}$$

where

$$P_{ij} \equiv -\left(\overline{u_i u_k} \frac{\partial U_j}{\partial x_k} + \overline{u_j u_k} \frac{\partial U_i}{\partial x_k} \right)$$

$$D_{ij} \equiv -\left(\overline{u_i u_k} \frac{\partial U_k}{\partial x_j} + \overline{u_j u_k} \frac{\partial U_k}{\partial x_i} \right)$$

$$P \equiv -\overline{u_i u_j} \frac{\partial U_i}{\partial x_j}$$

---

† When equations (11) and (13) are used values of 1.5 and 0.4 are recommended for c_1 and c_2'', respectively.

A simpler degenerate version that only includes the dominant first term in the above equation is also widely used (Gibson and Launder, Ref. 15, Samaraweera, Ref. 16). Since all three terms in equation (13) vanish under contraction, the redistributive nature of $\phi_{ij,2}$ is not destroyed by this approximation, given by

$$\phi_{ij,2} = - c_2 \left(P_{ij} - \frac{2}{3} \delta_{ij} P\right) \tag{14}$$

Modeling of $\phi_{ij,w}$: Rigid boundaries affect the flowfield by impeding the transfer of energy from the streamwise direction to that normal to the boundary, and also reduce the relative magnitude of the shear stress. As shown by Shir (Ref. 17) and Gibson and Launder (Ref. 15), these effects (contained in the surface integral in equation (10)) can be modeled in the form of near-wall correction terms $\phi'_{ij,1}$ and $\phi'_{ij,2}$:

$$\phi'_{ij,1} = c'_1 \frac{\varepsilon}{k} \left(\overline{u_k u_m}\, n_k n_m\, \delta_{ij} - \frac{3}{2} \overline{u_k u_j}\, n_k n_i - \frac{3}{2} \overline{u_k u_i}\, n_k n_j\right) f \left(\frac{\ell}{n_i r_i}\right)$$

near-wall correction to $\phi_{ij,1}$ (15)

$$\phi'_{ij,2} = c'_2 \left(\phi_{km,2}\, n_k n_m\, \delta_{ij} - \frac{3}{2} \phi_{ik,2}\, n_k n_j - \frac{3}{2} \phi_{jk,2}\, n_k n_i\right) f \left(\frac{\ell}{n_i r_i}\right)$$

near-wall correction to $\phi_{ij,2}$ (16)

where r_i is the position vector, ℓ is a characteristic turbulence length scale, f is the length scale function, and n is the unit normal vector to the surface. These terms diminish with distance from a rigid boundary and become negligible at great distances. This behavior is achieved by defining the length-scale function $f(\ell/n_i r_i)$ in such a way that it vanishes as $\ell/n_i r_i$ approaches zero. Here f is assumed to be directly proportional to ℓ/y, with ℓ interpreted as the dissipation length scale $k^{3/2}/\varepsilon$ and y is the normal distance from the rigid boundary. The constant of proportionality is chosen to render f of value unity in near-wall turbulence. Thus, for a single wall, f becomes

$$f = \frac{k^{3/2}/\varepsilon}{\kappa/a^{3/2} y} \tag{17}$$

where κ is the von Karman constant and $a = -\overline{uv}/k$. For flow between two parallel walls both of which influence the flow at a given point it is assumed that the effects are additive, i.e.

$$f = \frac{k^{3/2}/\varepsilon}{\frac{\kappa}{a^{3/2}}\left[\frac{1}{(1/y) + (1/h - y)}\right]} \tag{18}$$

where h is the distance of separation between the walls.

E. Diffusive Transport, Term V

As shown in equation (7) the diffusive transport process includes three mechanisms: transport through triple-velocity correlations, transport through pressure-fluctuating-velocity correlations, and molecular (viscous) transport. At high Reynolds numbers, molecular transport is usually insignificant and is not retained in the equation. Diffusive transport through the pressure-fluctuating-velocity correlations is also assumed to be negligible as a result of Irwin's study of self-preserving jets in adverse pressure gradients (Ref. 18), and Hanjalic and Launder's work on asymmetric plane channel flows. Even though Lumley has made some suggestions for modeling this term (Ref. 19), no proven models are as yet available. Within these approximations the diffusive transport term reduces to the triple-velocity correlation which has to be evaluated algebraically or from a transport equation. Hanjalic and Launder (Ref. 20) arrive at the following form for this correlation after introducing drastic simplifications to its transport equation:

$$\overline{u_i u_j u_k} = -c_s' \frac{k}{\varepsilon}\left(\overline{u_i u_\ell}\frac{\partial \overline{u_j u_k}}{\partial x_\ell} + \overline{u_j u_\ell}\frac{\partial u_k u_i}{\partial x_\ell} + \overline{u_k u_\ell}\frac{\partial \overline{u_i u_j}}{x_\ell}\right) \tag{19}$$

Daly and Harlow (Ref. 6) have proposed a considerably simpler representation for $\overline{u_i u_j u_k}$ that only retains the last term in the above equation

$$\overline{u_i u_j u_k} = -c_s \frac{k}{\varepsilon}\overline{u_k u_\ell}\frac{\overline{\partial u_i u_j}}{\partial x_\ell}^{\dagger} \tag{20}$$

---

†Values of 0.11 and 0.20 are recommended for c_s' and c_s,, respectively.

Thin shear flow calculations by Launder et al. (Ref. 14) and plane wall flow predictions by Reece (Ref. 21) show about equal success with data for both versions.

TABLE 2.1. Recommended Values for Turbulence Model Constants Reynolds Stress Transport Equations.

$$\kappa = 0.4187$$

$$c_\mu = 0.09$$

$$\sigma_k = 1.00$$

$$\sigma_\varepsilon = \kappa^2/(c_{\varepsilon_2} - c_{\varepsilon_1})c_\mu^{1/2}$$

$$c_{\varepsilon_1} = 1.44$$

$$c_{\varepsilon_2} = 1.92$$

$$c_k = 0.22$$

$$c_{\varepsilon_3} = 0.36\ (c_{\varepsilon_2} - c_{\varepsilon_1})$$

$$c_1 = 1.8$$

$$c_2 = 0.6$$

$$c_1' = 0.5$$

$$c_2' = 0.3$$

$$c_\ell = 2.55$$

2.3 ALTERNATIVE CLOSURE VIA THE ALGEBRAIC STRESS MODEL

An orthodox second-order closure would require the solution of a transport equation of the form of equation (7) for each of the stress components. Even for two-dimensional flows this can be a formidable task, since, in addition to the mean flow equations (equations (5) and (6)), five other transport equations (for $\overline{u^2}$, $\overline{v^2}$, $\overline{uv}$, k, and ε) need to be solved. Under certain assumptions, however, the stress transport equations can be reduced to a set of

algebraic expressions. This idea forms the basis of the algebraic stress model to be discussed in this section.

Following Rodi (Ref. 4) it is noted that the only terms containing gradients of Reynolds stresses in equation (7) are those responsible for convective and diffusive transport. Therefore, if these gradients can be eliminated, the Reynolds stress transport equation reduces to a set of algebraic equations of the general form

$$\overline{u_i u_j} = \overline{u_i u_j}\left(\overline{u_p u_q},\ \partial u_\ell/\partial x_m,\ \varepsilon,\ k\right)$$

The convective and diffusive transport of the stresses can be related to the turbulent kinetic energy transport rates by noting that

$$\frac{D\,\overline{u_i u_j}}{Dt} = \frac{\overline{u_i u_j}}{k}\frac{Dk}{Dt} + k\,\frac{D}{Dt}\,\frac{\overline{u_i u_j}}{k}$$

If the rate of variation of $\overline{u_i u_j}/k$ along a streamline is much lower than that of $\overline{u_i u_j}$ itself, then

$$\frac{D\,\overline{u_i u_j}}{Dt} = \frac{\overline{u_i u_j}}{k}\frac{Dk}{Dt} \tag{21}$$

Similarly,
$$D\overline{u_i u_j} = \frac{\overline{u_i u_j}}{k}\,D(k) + kD\left(\frac{\overline{u_i u_j}}{k}\right)$$

where the operator D stands for the net diffusion rate of the quantity in parentheses. If the spatial gradient of $\overline{u_i u_j}$ is large compared with that of $\overline{u_i u_j}/k$, then

$$D\,\overline{u_i u_j} = \frac{\overline{u_i u_j}}{k}\,D(k) \tag{22}$$

Also by definition (see Section 2.5)

$$\frac{Dk}{Dt} - D(k) = P - \varepsilon$$

Therefore, if equations (21) and (22) are solved for Dk/Dt and $D(k)$ and the results are substituted into the above expression, it becomes

$$\frac{k}{P - \varepsilon}\left\{\frac{D\overline{u_i u_j}}{Dt} - D(\overline{u_i u_j})\right\} = \overline{u_i u_j}$$

where the quantity in the brackets is nothing more than the sum of the production, dissipation, and pressure-strain terms in the full Reynolds stress transport equation, equation (7). Replacing these terms with their modeled forms from Section 2.3 (except for the production term, which is exact) produces a set of implicit algebraic expressions for the stresses in terms of the mean strain rate, turbulent kinetic energy k and its dissipation rate ε, and the stresses themselves. Hence the final form of the algebraic stress model (ASM) that includes near-wall corrections becomes

$$\overline{u_i u_j} = \frac{k}{(P - \varepsilon)}\left(P_{ij} - \frac{2}{3}\delta_{ij}\varepsilon + \phi_{ij,1} + \phi_{ij,2} + \phi'_{ij,1} + \phi'_{ij,2}\right) \qquad (23)$$

where

$P = -\overline{u_i u_k}\frac{\partial U_i}{\partial x_k}$, the production rate of kinetic energy

$P_{ij} = -\left(\overline{u_i u_k}\frac{\partial U_j}{\partial x_k} + \overline{u_j u_k}\frac{\partial U_i}{\partial x_k}\right)$, the production rate of individual Reynolds stresses

$\phi_{ij,1} = -c_1\varepsilon/k\,(\overline{u_i u_j} - 2/3\,\delta_{ij}\,k)$, the modeled form of the contribution of fluctuating quantities to the pressure-strain correlation, equation (11)

$\phi_{ij,2} = -c_2\,(P_{ij} - 2/3\,\delta_{ij}P)$, the modeled form of the contribution of mean strain effects to the pressure-strain correlation, equation (14)

$\phi'_{ij,1} = c'_1\,\varepsilon/k\,(\overline{u_k u_m}\,n_k n_m\,\delta_{ij} - 3/2\,\overline{u_k u_j}\,n_k n_i - 3/2\,\overline{u_k u_i}\,n_k n_j)\,f\left(\frac{\ell}{n_i r_i}\right)$, wall correction to $\phi_{ij,1}$, equation (15)

$\phi'_{ij,2} = c'_2\,(\phi_{km,2}\,n_k n_m\,\delta_{ij} - 3/2\phi_{ik,2}\,n_k n_j - 3/2\phi_{jk,2}\,n_k n_i)\,f\,(\ell/n_i r_i)$, wall correction to $\phi_{ij,2}$, equation (16)

Equation (23) is the version of ASM used in the work described in this report.

The algebraic stress model represents a significant simplification over the full Reynolds stress closure and yet it is versatile and is based on a plausible derivation. For two-dimensional elliptic flows it requires the solution of three implicit algebraic equations for the stresses and two transport equations for k and ε. However, the formulation usually entails a considerable amount of algebraic manipulation which can be tedious and costly. In addition, as discussed in Section 3, special care is needed in incorporating these stresses into the mean flow equations to ensure good stability and convergence characteristics.

2.4 ALTERNATIVE CLOSURE VIA THE k-ε MODEL

The k-ε model (also known as the two-equation model) developed by Jones and Launder (Ref. 22) introduces another degree of simplification to closure of the mean flow equations. This model achieves closure by relating the Reynolds stresses to the mean strain rate through the Boussinesq approximation.

$$-\rho \overline{u_i u_j} = \mu_t \left(\frac{\partial U_i}{\partial x_j} + \frac{\partial U_j}{\partial x_i} \right) - 2/3 \, \delta_{ij} \, \rho \, k \tag{24}$$

The effective (turbulent or eddy) viscosity appearing above, μ_t, is defined in terms of a characteristic length and velocity (an idea apparently borrowed from the kinetic theory of gases). If this length is taken as the turbulence length scale $k^{3/2}/\varepsilon$ and the velocity as $k^{1/2}$, μ_t can be expressed as

$$\mu_t \equiv c_\mu \, \rho \, k^2/\varepsilon$$

where c_μ is a constant of proportionality. Equation (24) is the version of the k-ε model used in the present calculations.

Conceptually the use of an effective viscosity for turbulent flows has many drawbacks. Firstly, contrary to the requirements of the kinetic theory of gases the large energy containing eddies are not rigid bodies which retain their identity, and also their "mean free paths" are usually not small compared with the flow dimensions. In addition the simple isotropic effective viscosity concept breaks down for complex turbulent flows where the shear stress and the velocity gradients may have opposite signs, and the effects of the non-equal

normal stress components and secondary strain rates may be substantial. However, despite all these shortcomings the k-ε model has been successful in predicting a wide range of thin shear flows and also some complex turbulent flows (with minor modifications to the basic form given in equation (24)). The simplicity of its formulation and excellent numerical stability characteristics have made this model popular in turbulent flow computations.

2.5 MODELING OF THE k TRANSPORT EQUATION

Both the k-ε viscosity and the ASM require evaluation of the turbulent kinetic energy and its dissipation rate to define turbulent time and length scales. This and the next section will present the modeled form of the k and ε transport equations, respectively.

The turbulent kinetic energy equation can be obtained from the Reynolds stress transport equation, equation (7), by setting i = j and dividing by 2

$$\frac{\partial k}{\partial t} + U_k \frac{\partial}{\partial x_k} k = - \overline{u_i u_k} \frac{\partial U_i}{\partial x_k} - \nu \overline{\frac{\partial u_i}{\partial x_k} \frac{\partial u_i}{\partial x_k}} - \nu \overline{\frac{\partial u_i}{\partial x_k} \frac{\partial u_k}{\partial x_i}}$$

$$+ \frac{\partial}{\partial x_k} \left\{ \nu \left(\frac{\partial k}{\partial x_k} + \frac{\partial \overline{u_i u_k}}{\partial x_i} \right) - \frac{\overline{u_i^2 u_k}}{2} - \frac{1}{\rho} \overline{p u_i} \, \delta_{ik} \right\}$$

This equation when modeled and reduced to its high Reynolds number form becomes

$$\frac{\partial k}{\partial t} + U_k \frac{\partial k}{\partial x_k} = - \overline{u_i u_k} \frac{\partial U_i}{\partial x_k} - \varepsilon + \frac{\partial}{\partial x_k} \left(\nu \frac{\partial k}{\partial x_k} + c_k \overline{u_i u_k} \frac{k}{\varepsilon} \frac{\partial k}{\partial x_i} \right) \qquad (25)$$

where within the high Reynolds number approximation ε is represented by $\nu \overline{\frac{\partial u_i}{\partial x_k} \frac{\partial u_i}{\partial x_k}}$; and $\overline{u_i^2 u_k}/2$ has been taken as $c_k \overline{u_i u_k} \frac{k}{\varepsilon} \frac{\partial k}{\partial x_i}$, the form proposed by Daly and Harlow (equation (20)). The terms $\nu \overline{\frac{\partial u_i}{\partial x_k} \frac{\partial u_k}{\partial x_i}}$ and $\overline{p u_i} \, \delta_{ik}$ have been neglected as discussed in Section 2.2, part E. This form of the k transport equation, suitable for use with the ASM, can be further simplified for

the k-ε model by introducing the additional postulate $\overline{u_i u_k} = 2/3\ \delta_{ik}\ k$ into the diffusion term to yield

$$\frac{\partial k}{\partial t} + U_k \frac{\partial k}{\partial x_k} = - \overline{u_i u_k} \frac{\partial U_i}{\partial x_k} - \varepsilon + \frac{\partial}{\partial x_k}\left(\nu \frac{\partial k}{\partial x_k} + \frac{\nu_t}{\sigma_k} \frac{\partial k}{\partial x_k}\right) \tag{26}$$

where $\sigma_k = 3/2 c_\mu / c_k$ is the turbulent kinetic energy Prandtl number.

2.6 MODELING OF THE ε TRANSPORT EQUATION

The dissipation rate of kinetic energy ε is evaluated from its transport equation formed by multiplying the u_i transport equation (equation (9)) by $2\nu\ \partial u_i/\partial x_j$ and time averaging:

$$\frac{D\varepsilon}{Dt} = \underbrace{-2\nu \frac{\partial U_i}{\partial x_k}\left(\overline{\frac{\partial u_i}{\partial x_j}\frac{\partial u_k}{\partial x_j}} + \overline{\frac{\partial u_j}{\partial x_i}\frac{\partial u_j}{\partial x_k}}\right)}_{a} \underbrace{- 2\nu\ \overline{u_k \frac{\partial u_i}{\partial x_j}} \frac{\partial^2 U_i}{\partial x_k \partial x_j}}_{b} \underbrace{- 2\nu \overline{\frac{\partial u_i}{\partial x_k}\frac{\partial u_i}{\partial x_j}\frac{\partial u_k}{\partial x_j}}}_{c}$$

$$\underbrace{-2\left(\nu \overline{\frac{\partial^2 u_i}{\partial x_k \partial x_j}}\right)^2}_{d} \underbrace{- \frac{\partial}{\partial x_k}\left(\overline{\nu u_k \left(\frac{\partial u_i}{\partial x_j}\right)^2} + \frac{2\nu}{\rho}\overline{\frac{\partial p}{\partial x_i}\frac{\partial u_k}{\partial x_i}} - \nu \frac{\partial \varepsilon}{\partial x_k}\right)}_{e} \tag{27}$$

Before this equation can be solved, however, all the terms appearing on the right-hand side have to be modeled in terms of known or calculable variables. This is a formidable task in itself since generally no measurements of these quantities are available.

Terms a and b represent, respectively, generation due to vortex stretching and secondary generation by the mean flow. Both of these terms are shown by Tennekes and Lumley (Ref. 23) to be of negligible importance at high Reynolds numbers, and are dropped from the equation. Terms c and d on the other hand serve as the primary source (generation due to vortex stretching by turbulence) and sink (destruction by viscous action), respectively, for this

correlation and become increasingly important at high Reynolds numbers. Most prefer to model the sum† of these terms as suggested by Launder et al. (Ref. 14).

$$c_{\varepsilon_1} \frac{\varepsilon}{k} P - c_{\varepsilon_2} \frac{\varepsilon^2}{k} \tag{28}$$

where c_{ε_1} and c_{ε_2} are two constants evaluated, respectively, by reference to near-wall turbulence and decay of grid turbulence. The currently recommended values for these constants are given in Table 2.1.

The diffusion term e is treated by neglecting the pressure-diffusion terms and modeling

$$\overline{\nu\, u_k \left(\frac{\partial u_i}{\partial x_j}\right)^2} \text{ as } -c_{\varepsilon_3} \frac{k}{\varepsilon} \overline{u_k u_i} \frac{\partial \varepsilon}{\partial x_i} \tag{29}$$

This form was proposed by Hirt (Ref. 24) and also was used by Hanjalic and Launder (Ref. 20). The constant c_{ε_3} can be expressed in terms of c_{ε_1} and c_{ε_2} as $0.36(c_{\varepsilon_2} - c_{\varepsilon_1})$.

When these approximations are introduced into equation (27) the modeled ε transport equation becomes

$$\frac{\partial \varepsilon}{\partial t} + U_k \frac{\partial \varepsilon}{\partial x_k} = c_{\varepsilon_1} \frac{\varepsilon}{k} P - c_{\varepsilon_2} \frac{\varepsilon^2}{k} + \frac{\partial}{\partial x_k}\left(\nu \frac{\partial \varepsilon}{\partial x_k} + c_{\varepsilon_3} \overline{u_i u_k} \frac{k}{\varepsilon} \frac{\partial \varepsilon}{\partial x_i}\right) \tag{30}$$

The form of the ε transport equation given by equation (30) is suitable for use with the ASM. The k-ε model version is obtained by approximating $\overline{u_i u_k}$ as $2/3\, \delta_{ik} k$ in the diffusion term to yield

$$\frac{\partial \varepsilon}{\partial t} + U_k \frac{\partial \varepsilon}{\partial x_k} = c_{\varepsilon_1} \frac{\varepsilon}{k} P - c_{\varepsilon_2} \frac{\varepsilon^2}{k} + \frac{\partial}{\partial x_k}\left(\nu \frac{\partial \varepsilon}{\partial x_k} + \frac{\nu_t}{\sigma_\varepsilon} \frac{\partial \varepsilon}{\partial x_k}\right) \tag{31}$$

where σ_ε is the turbulent kinetic energy dissipation rate Prandtl number equal to

---

†Each of these terms becomes infinitely large as the Reynolds number approaches infinity. However, they have opposite signs and their sum remains finite.

$$\frac{\kappa^2}{\left(c_{\varepsilon_2} - c_{\varepsilon_1}\right) c_\mu^{1/2}}$$

This follows directly from the definition of c_{ε_3}:

$$c_{\varepsilon_3} = -\frac{\left(c_{\varepsilon_2} - c_{\varepsilon_1}\right) c_\mu^{3/2}}{2/3\kappa^2}$$

2.7 MODIFICATION TO THE ε TRANSPORT EQUATION

Probably the weakest point in the closure by both the ASM and k-ε models is the determination of the turbulent kinetic energy dissipation rate. Lack of measurements make the modeling of the ε transport equation a challenging task. Since this equation is source dominated, the modeling of the source and sink terms is very critical. Equation (28) is an attempt to approximate the sum of these quantities by reference to the production rate of turbulent kinetic energy P[†], the dissipation rate ε, and a turbulent time scale k/ε. It has been argued by Pope (Ref. 25) and Hanjalic and Launder (Ref. 2) that the production term in the ε equation should be made more sensitive to irrotational straining. Both of these schemes propose to incorporate a new term into the ε-equation that could impart this characteristic. However, the success of these methods in some free shear flows did not carry over to more complex recirculating flow predictions.

A different approach has been taken by Hanjalic, Launder and Sindir (Ref. 5) who suggest replacing P $(= - \overline{u_i u_j}\ (\partial U_i/\partial x_j))$ in the ε transport equations (30) and (31) by

$$c_\mu\ k^2/\varepsilon \left(\frac{\partial U_i}{\partial x_j}\right)^2 \qquad (32)$$

[†]The plausibility of this proposal has long been debated since the fine scale motions ε represents are isotropic in character and should not be directly sensitive to the turbulent kinetic energy production rate (which involves large energy carrying eddies strained by the mean flow).

There is no compelling argument to suggest that the effects of mean strain should be accountable by a term exactly proportional to the kinetic energy generation rate. Equation (32) has been adopted because it displays greater sensitivity than the original to streamwise curvature - a characteristic that experiments have shown to be desirable. In a straight thin shear flow in local equilibrium the proposed form reduces very nearly to that of the "standard" ε equation. It was hoped that this modification would produce significant improvements in recirculating flow predictions where there is substantial streamwise curvature. As discussed in Section 3, this generally proved to be the case. The form given in equation (32) was used with both the ASM and the k-ε models. When equation (32) is used, the turbulence models will be referred to as the "modified" ASM and the "modified" k-ε, respectively, to differentiate from the standard versions of the models.

2.8 MULTIPLE-SCALE MODELING

Both the ASM and the k-ε approaches are single-point models which adopt a single time scale proportional to the turbulence energy turnover time, namely k/ε. However, it is overly simplistic, at least conceptually, to assume that a single time scale can successfully characterize the rates of progress of different turbulent interactions. This realization led Hanjalic, Launder and Schiestel (Ref. 3) to develop the multiple-scale approach that is discussed next.

The key to the new multiple-scale approach is the recognition that while the dissipation equation (equation (31)) and the kinetic energy equation (equation (26)) both contain production and dissipation terms, these processes occur in different spectral regions of the flow. That is, turbulence energy production occurs in the larger eddies in the flow, while dissipation phenomena involve primarily the smaller scales. Thus, there must be a transfer of energy from the larger scales to the smaller, and this transfer can, in certain situations, introduce a lag phenomenon, so that turbulence energy production and turbulence energy dissipation do not necessarily both increase or decrease in the same region of the flow as is implied by equations (26) and (31).

To introduce a model in which the evolution of the different scales appropriate to the large-eddy production region and the small-eddy dissipation region can be accounted for, Launder and co-workers introduced a partitioning of the turbulence energy and its dissipation rate, as shown schematically in Figure 2.1. In this figure, a partitioning into three regions is shown. For wave numbers less than κ_1, a production region is defined, characterized by a turbulent kinetic energy k_p and a dissipation rate ε_p. This dissipation rate controls the transfer of energy through the transfer region $\kappa_1 < \kappa < \kappa_2$. For wave numbers higher than κ_2, turbulence energy is dissipated as heat. A separate kinetic energy and dissipation rate equation is written for the transfer region, characterized by k_T and ε_T, and the production term in the kinetic energy equation for the transfer region is equal to the dissipation rate ε_p in the production region.

The partitioning of the energy spectrum that is the key feature of the multiple-scale model can clearly be carried out as many times as computer capacity will allow, but in practice, a partitioning into three regions appears to be sufficient (Ref. 3). This requires two sets of transport equations, given the assumption (basic to most turbulence modeling) that the mechanisms involved in the final dissipation of turbulent kinetic energy into thermal energy are capable of accepting all of the energy transferred to them. This assumption is the reason that the physical fluid viscosity does not appear in the turbulence dissipation rate equations and is supported by the observed Reynolds number invariance of fully-turbulent flows. Further, in practice it also is observed that the exact point in the wave-number spectrum at which the energy spectrum is partitioned does not appear to exert much influence on the results; however, it does appear to be influential in initial condition determination (Ref. 1).

The model equations for the production and transfer region turbulent kinetic energy and dissipation rate are similar in form to the k and ε transport equations discussed in Sections 2.5 and 2.6, respectively. They are:

Production Region

$$\frac{\partial k_p}{\partial t} + U_k \frac{\partial k_p}{\partial x_k} = P_k - \varepsilon_p + \frac{\partial}{\partial x_k}\left(\left(\nu + \frac{\nu_t}{\sigma_k}\right)\frac{\partial k_p}{\partial x_k}\right) \tag{33}$$

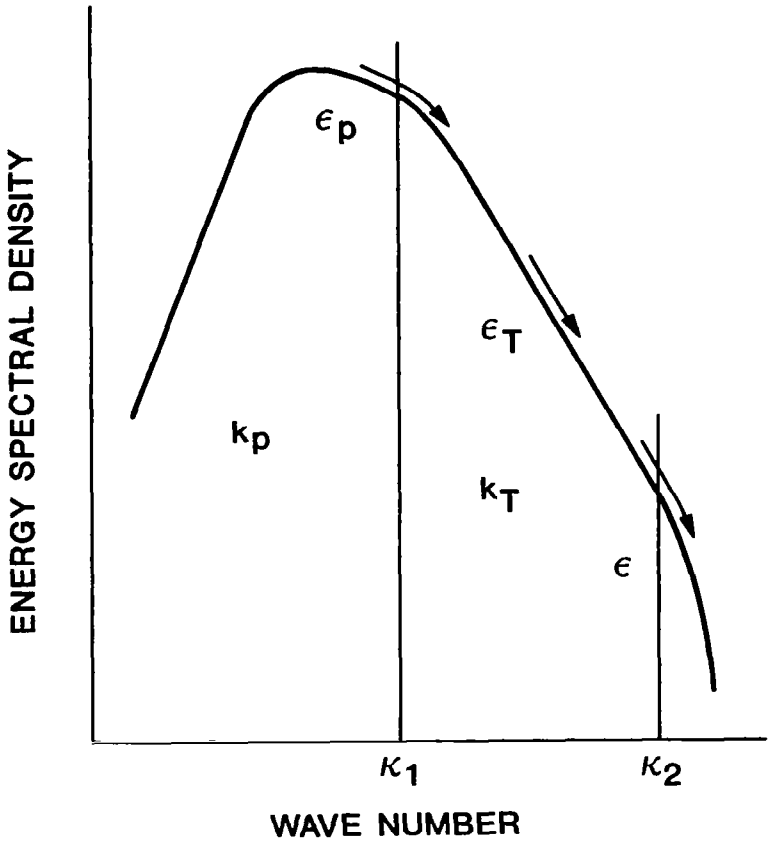

FIGURE 2.1. Spectral Division of Turbulence Energy and Dissipation Rate.

$$\frac{\partial \varepsilon_p}{\partial t} + U_k \frac{\partial \varepsilon_p}{\partial x_k} = c_{p_1} P_k \frac{\varepsilon_p}{k_p} - c_{p_2} \frac{\varepsilon_p^2}{k_p} + \frac{\partial}{\partial x_k}\left[\left(\nu + \frac{\nu_t}{\sigma_\varepsilon}\right)\frac{\partial \varepsilon_p}{\partial x_k}\right] \tag{34}$$

Transfer Region

$$\frac{\partial k_T}{\partial t} + U_k \frac{\partial k_T}{\partial x_k} = \varepsilon_p - \varepsilon_T + \frac{\partial}{\partial x_k}\left[\left(\nu + \frac{\nu_t}{\sigma_k}\right)\frac{\partial k_T}{\partial x_k}\right] \tag{35}$$

$$\frac{\partial \varepsilon_T}{\partial t} + U_k \frac{\partial \varepsilon_T}{\partial x_k} = c_{T_1} \frac{\varepsilon_p \varepsilon_T}{k_T} - c_{T_2} \frac{\varepsilon_T^2}{k_T} + \frac{\partial}{\partial x_k}\left[\left(\nu + \frac{\nu_t}{\sigma_\varepsilon}\right)\frac{\partial \varepsilon_T}{\partial x_k}\right] \tag{36}$$

in which the subscript p refers to the production region and T to the transfer region. In this formulation, the turbulent viscosity is given by

$$\mu_T = \rho c_\mu (k_p + k_T) \frac{k_p}{\varepsilon_p} \tag{37}$$

and

$$P_k = -\overline{u_i u_j} \frac{\partial U_i}{\partial x_j} \tag{38}$$

This formulation introduces five coefficients, compared to three for the two-equation model, but values for several of these coefficients can be inferred from two-equation model results and from examination of limiting cases. The procedure used to establish the coefficients is described in detail in Ref. 3; the results are

$$c_{p_1} = 2.2,\ c_{p_2} = 1.8 - 0.3\left(\frac{k_p}{k_T} - 1\right)\Big/\left(\frac{k_p}{k_T} + 1\right)$$

$$c_{T_1} = 1.08\frac{\varepsilon_p}{\varepsilon_T},\ c_{T_2} = 1.15,\ c_\mu = 0.09$$

2.9 WALL-FUNCTION TREATMENT

Most turbulence models including the present versions of the ASM and k-ε models) are devices for high Reynolds number flows. However, in the vicinity of

solid boundaries where the velocities are small, the low Reynolds number effects previously neglected become significant and should be accounted for. This can be accomplished either by solving the low Reynolds number form of the transport equations or by developing wall-functions that introduce these effects into the existing high Reynolds number models. Chieng and Launder (Ref. 26) found that the first option required vast amounts of computer time due to the slow convergence characteristics of the low Reynolds number models. On the other hand a new wall-function treatment proposed by the same authors was shown to incorporate these effects with practically no increase in computing time. An expanded version of this treatment is used in the present study.

A. Near-Wall Velocity Profile and Drag Law

In flows where the principal source of turbulence energy generation lies remote from the walls and the diffusion of energy is towards the surface two key approximations can be made in devising wall-functions. Firstly, the dominance of the walls on the near-wall length scale can be taken as complete, i.e., outside the viscous sublayer (where the flow is viscous but not laminar) the turbulence length scale is held to depend, for a limited region near a wall, only on the normal distance to the surface. Secondly, the viscous sublayer thickness y_v is assumed to adjust itself according to the external turbulence energy such that the sublayer Reynolds number $Re_v \equiv y_v k_v^{1/2}/\nu$ (where k_v is the turbulence kinetic energy at the edge of the viscous sublayer) is a universal constant equal to 20. Under these conditions Chieng and Launder (Ref. 26) propose a new wall-function treatment which is discussed below.

Figure 2.2a shows a typical near-wall scalar cell (bounded on the west side by a wall) on which the following discussions are based. The grid is so arranged that node P lies outside the viscous sublayer in the fully turbulent region. The shear stress at the wall is estimated by assuming that the mean velocity component parallel to the wall varies with height over the fully turbulent region as proposed by Launder and Spalding (Ref. 27)

$$\frac{U k_v^{1/2}}{(\tau_w/\rho)} = \frac{1}{\kappa^*} \ln E^* \frac{y k_v^{1/2}}{\nu} \qquad (39)$$

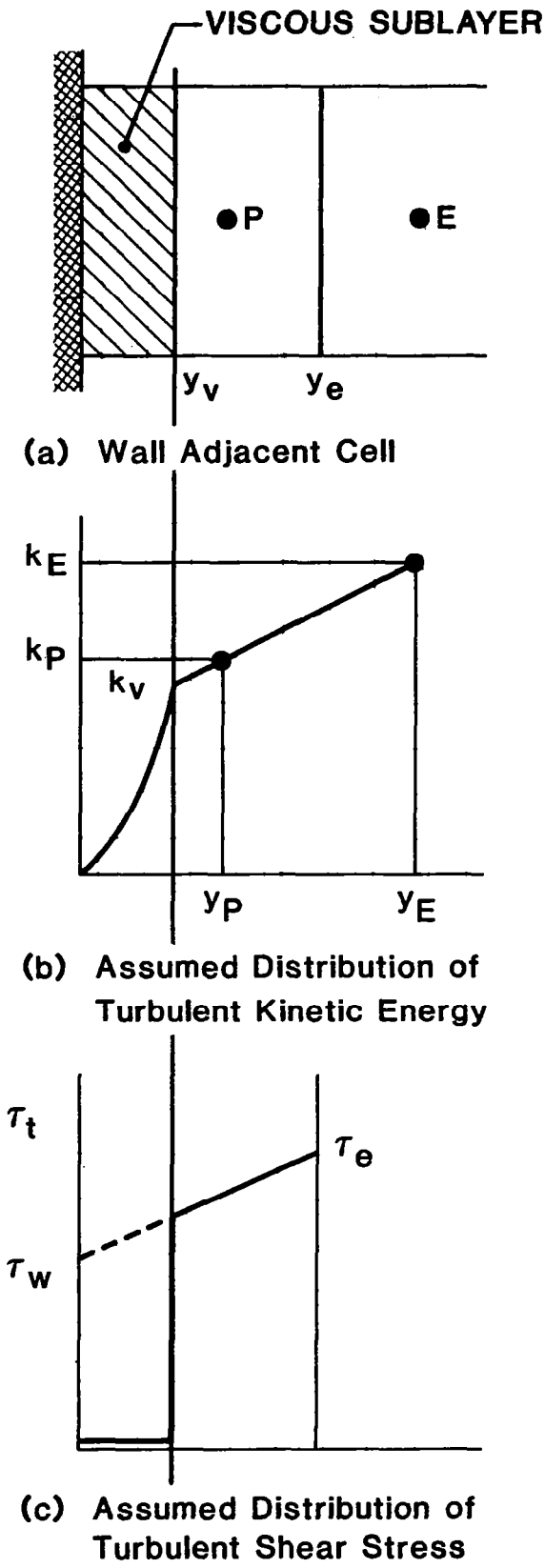

FIGURE 2.2. Near-Wall Physical Model.

with the exception that the kinetic energy is now evaluated at the edge of the viscous sublayer†. Solving this equation for τ_w and evaluating the resultant at node P produces the drag law for non-equilibrium turbulent flows

$$\tau_w = \kappa^* \rho U_p k_v^{1/2}/(\ell n\ E^* y_p k_v^{1/2}/\nu) \qquad (40)$$

where $\kappa^* = \kappa c_\mu^{1/4}$ and $E^* = E c_\mu^{1/4}$. E^* can also be evaluated in terms of Re_v by matching the linear velocity profile in the viscous sublayer written as

$$\frac{U k_v^{1/2}}{\tau_w/\rho} = \frac{y k_v^{1/2}}{\nu}$$

with the fully turbulent velocity profile (equation (39)) at y_v to get $E^* = \exp(\kappa^* Re_v)/Re_v$.

B. Near-Wall Turbulent Kinetic Energy Budget and Dissipation Rate

The near-wall kinetic energy levels are obtained from the solution of the k transport equation (equations (25), (26)) modified to reflect these effects. The convection and diffusion terms require no changes and are treated in a standard way. The production and dissipation terms, however, need to be changed to include the near-wall effects.

The evaluation of the mean production rate of k requires specifying the local turbulent shear stress distribution over the near-wall cells. As shown in Figure 2.2c a piece-wise continuous shear stress variation is assumed.

---

†The conventional law-of-the-wall

$$\frac{U}{\sqrt{\tau_w/\rho}} = \frac{1}{\kappa} \ell n \frac{Ey\sqrt{\tau_w/\rho}}{\nu}$$

valid for flows in local equilibrium ($P = \varepsilon$) can be thought of as a limiting case of equation (39) obtained by replacing k_v with $\tau_w/\rho c_\mu^{1/2}$ (the local equilibrium value of k). This also shows that $\kappa^* = \kappa c_\mu^{1/4}$ and $E^* = E c_\mu^{1/4}$.

$$\tau_t = \begin{cases} 0 & 0 \leq y < y_v \\ \tau_w + (\tau_e - \tau_w)y/y_e & y_v \leq y \leq y_e \end{cases} \tag{41}$$

This way the stress vanishes in the viscous sublayer, increases abruptly at the edge ($y = y_v$), and then varies linearly over the remainder of the cell. The mean production rate of k per unit volume can then be evaluated by integrating $\tau_t(\partial U/\partial y + \partial V/\partial x)$ over the surface of the cell

$$\text{Mean Production Rate} = \frac{1}{y_e} \int_{y_v}^{y_e} \tau_t \left(\frac{\partial U}{\partial y} + \frac{\partial V}{\partial x}\right) dy.$$

Substituting equation (41) for τ_t and equation (39) for U and integrating, this expression reduces to its final form

$$\frac{\tau_w(U_e - U_v)}{y_e} + \frac{\tau_w(\tau_e - \tau_w)}{\kappa^* \rho k_v^{1/2} y_e}(1 - y_v/y_e) + \tau_w \frac{\partial V}{\partial x}\left(1 - \frac{y_v}{y_e}\right) + (\tau_e - \tau_w)\frac{\partial V}{\partial x}\left[1 - \left(\frac{y_v}{y_e}\right)^2\right] \tag{42}$$

The mean dissipation rate of kinetic energy is evaluated by integrating the ε distribution over the volume of the cell. In the viscous sublayer the dissipation rate is shown to be equal to $2\nu(\partial k^{1/2}/\partial y)^2$ by Pope and Whitelaw (Ref. 28), and this expression, when coupled with the assumed parabolic variation of $k^{\dagger}$ ($= k_v(y/y_v)^2$) in the same region becomes

$$\varepsilon = 2\nu k_v / y_v^2 \tag{43}$$

In the fully turbulent region, following Spalding (Ref. 29), ε is taken to vary as

$$\varepsilon = k^{3/2}/c_{\ell} y \tag{44}$$

---

†This variation of k corresponds to a linear increase of fluctuating velocities with distance from the wall, and also has a zero gradient at the surface.

where c_ℓ is a universal constant given in Table 2.1 as 2.55. The mean dissipation rate can now be evaluated by integrating (43) over the viscous sublayer and equation (44) over the fully turbulent region (assuming a linear k variation as shown in Figure 2.2b), and averaging the resultant to obtain

$$\bar{\varepsilon} = \frac{1}{y_e} 2 \frac{k_v^{3/2}}{Re_v} + \frac{1}{y_e c_\ell} \left[\frac{2}{3} \left(k_e^{3/2} - k_v^{3/2} \right) + 2a \left(k_e^{1/2} - k_v^{1/2} \right) + \lambda_\varepsilon \right] \tag{45}$$

where

$$\lambda_\varepsilon = a^{3/2} \log \left[\frac{\left(k_e^{1/2} - \sqrt{a} \right)}{\left(k_e^{1/2} + \sqrt{a} \right)} \Bigg/ \frac{\left(k_v^{1/2} - \sqrt{a} \right)}{\left(k_v^{1/2} + \sqrt{a} \right)} \right] \quad \text{if } a \geq 0$$

$$\lambda_\varepsilon = 2(-a)^{3/2} \left[\tan^{-1} \frac{k_e^{1/2}}{\sqrt{-a}} - \tan^{-1} \frac{k_v^{1/2}}{\sqrt{-a}} \right] \quad \text{if } a < 0$$

and

$$a = k_p - \frac{(k_p - k_E)}{(y_p - y_E)} y_p \, .$$

In this equation k_p and k_E are the k values at nodes P and E, respectively, and k_e represents the value at the eastern boundary of the cell as depicted in Figure 2.2b.

The level of k_v is obtained by extrapolating the line through k_p and k_E to $y = y_v$, hence

$$k_v = k_p + \frac{y_p - y_v}{y_E - y_p} (k_E - k_p) \tag{46}$$

The thickness of the viscous sublayer y_v and the mean velocity at the location U_v are then expressed as

$$y_v = \nu Re_v / k_v^{1/2} \tag{47}$$

and

$$U_v = Re_v(\tau_w/\rho)/k_v^{1/2}$$

It should be noted that y_v appears in the above expression for k_v (equation (46)); hence to obtain a non-iterative solution the following cubic equation for k_v (obtained upon substituting for y_v from equation (47)) has to be solved:

$$k_v = k_p + \frac{y_p - \nu Re_v k_v^{-1/2}}{y_E - y_p}(k_E - k_p)$$

Alternatively, an iterative scheme that uses the previous iteration level value of y_v in (46) can be used to evaluate the current k_v values.

2.10 MEAN FLOW AND TURBULENCE MODEL EQUATIONS USED IN THE COMPUTATIONS

The transport and auxiliary equations† presented in the previous sections reduce, in the case of two-dimensional turbulent flows, to the following

A. k-ε Model

Conservation of Mass

$$\frac{\partial \rho}{\partial t} + \frac{\partial \rho U}{\partial x} + \frac{1}{r}\frac{\partial r\rho V}{\partial r} = 0 \qquad (48)$$

x-Momentum

$$\frac{\partial \rho U}{\partial t} + \frac{\partial \rho U^2}{\partial x} + \frac{1}{r}\frac{\partial r\rho UV}{\partial r} = -\frac{\partial P}{\partial x} + \frac{\partial}{\partial x}\left(2\mu_T \frac{\partial U}{\partial x}\right) + \frac{1}{r}\frac{\partial}{\partial r}\left[r\mu_T\left(\frac{\partial U}{\partial r} + \frac{\partial V}{\partial x}\right)\right] \qquad (49)$$

†These equations are written in a general form to accommodate both Cartesian and axisymmetric coordinates. For planar predictions r is set equal to 1 and the terms enclosed in boxes are omitted. For axisymmetric flows r equals to the polar radius.

r-Momentum

$$\frac{\partial \rho V}{\partial t} + \frac{\partial \rho UV}{\partial x} + \frac{1}{r}\frac{\partial r\rho V^2}{\partial r} = -\frac{\partial P}{\partial r} + \frac{\partial}{\partial x}\left[\mu_T\left(\frac{\partial V}{\partial x} + \frac{\partial U}{\partial r}\right)\right] + \frac{1}{r}\frac{\partial}{\partial r}\left(2r\mu_T\frac{\partial V}{\partial r}\right) - \boxed{2\mu_T\frac{V}{r^2}} \tag{50}$$

k Transport Equation

$$\frac{\partial \rho k}{\partial t} + \frac{\partial \rho Uk}{\partial x} + \frac{1}{r}\frac{\partial r\rho Vk}{\partial r} = \rho P - \rho\varepsilon + \frac{\partial}{\partial x}\left(\mu + \frac{\mu_t}{\sigma_k}\right)\frac{\partial k}{\partial x} + \frac{1}{r}\frac{\partial}{\partial r}\left(\mu + \frac{\mu_t}{\sigma_k}\right)\frac{\partial k}{\partial r} \tag{51}$$

ε Transport Equation

$$\frac{\partial \rho \varepsilon}{\partial t} + \frac{\partial \rho U\varepsilon}{\partial x} + \frac{1}{r}\frac{\partial r\rho V\varepsilon}{\partial r}$$

$$= \rho c_{\varepsilon_1}\frac{\varepsilon}{k}P - \rho c_{\varepsilon_2}\frac{\varepsilon^2}{k} + \frac{\partial}{\partial x}\left(\mu + \frac{\mu_t}{\sigma_\varepsilon}\right)\frac{\partial \varepsilon}{\partial x} + \frac{1}{r}\frac{\partial}{\partial r}\left(\mu + \frac{\mu_t}{\sigma_\varepsilon}\right)\frac{\partial \varepsilon}{\partial r} \tag{52}$$

where

$$P = \frac{\mu_t}{\rho}\left\{2\left[\left(\frac{\partial U}{\partial x}\right)^2 + \left(\frac{\partial V}{\partial r}\right)^2 + \boxed{\left(\frac{V}{r}\right)^2}\right] + \left(\frac{\partial U}{\partial r} + \frac{\partial V}{\partial x}\right)^2\right\} \tag{53}$$

Turbulence Model

$$\mu_t = c_\mu \rho \frac{k^2}{\varepsilon}$$

$$\sigma_k = \frac{3}{2}\frac{c_\mu}{c_k}$$

$$\sigma_\varepsilon = \frac{\kappa^2}{\left(c_{\varepsilon_2} - c_{\varepsilon_1}\right)c_\mu^{1/2}}$$

where

$$\mu_T = \mu_t + \mu$$

and the constants c_μ, c_k, c_{ε_1}, c_{ε_2} and κ are defined in Table 2.1.

B. Multi-Scale k-ε Model

Conservation of Mass

$$\frac{\partial \rho}{\partial t} + \frac{\partial \rho U}{\partial x} + \frac{1}{r}\frac{\partial r \rho V}{\partial r} = 0 \tag{54}$$

x-Momentum

$$\frac{\partial \rho U}{\partial t} + \frac{\partial \rho U^2}{\partial x} + \frac{\partial \rho U V r}{\partial r} = -\frac{\partial P}{\partial x} + \frac{\partial}{\partial x}\left(2\mu_T \frac{\partial U}{\partial x}\right) + \frac{1}{r}\frac{\partial}{\partial r}\left[r\mu_T\left(\frac{\partial U}{\partial r} + \frac{\partial V}{\partial x}\right)\right] \tag{55}$$

r-Momentum

$$\frac{\partial \rho V}{\partial t} + \frac{\partial \rho U V}{\partial x} + \frac{\partial \rho V^2 r}{\partial r} = -\frac{\partial P}{\partial r} + \frac{\partial}{\partial x}\left[\mu_T\left(\frac{\partial V}{\partial x} + \frac{\partial U}{\partial r}\right)\right] + \frac{1}{r}\frac{\partial}{\partial r}\left(2\mu_T r \frac{\partial V}{\partial r}\right) - \boxed{2\mu_T \frac{V}{r^2}} \tag{56}$$

k Transport Equations

$$\frac{\partial \rho k_p}{\partial t} + \frac{\partial \rho U k_p}{\partial x} + \frac{\partial r \rho V k_p}{\partial r} = \rho P - \rho \varepsilon_p + \frac{\partial}{\partial x}\left[\left(\mu + \frac{\mu_t}{\sigma_k}\right)\frac{\partial k_p}{\partial x}\right] + \frac{1}{r}\frac{\partial}{\partial r}\left[r\left(\mu + \frac{\mu_t}{\sigma_k}\right)\frac{\partial k_p}{\partial r}\right] \tag{57}$$

$$\frac{\partial \rho k_T}{\partial t} + \frac{\partial \rho U k_T}{\partial x} + \frac{\partial r \rho V k_T}{\partial r} = \rho \varepsilon_p - \rho \varepsilon_T + \frac{\partial}{\partial x}\left[\left(\mu + \frac{\mu_t}{\sigma_k}\right)\frac{\partial k_T}{\partial x}\right] + \frac{1}{r}\frac{\partial}{\partial r}\left[r\left(\mu + \frac{\mu_t}{\sigma_k}\right)\frac{\partial k_T}{\partial r}\right] \tag{58}$$

ε Transport Equations

$$\frac{\partial \rho \varepsilon_p}{\partial t} + \frac{\partial \rho U \varepsilon_p}{\partial x} + \frac{\partial r \rho V \varepsilon_p}{\partial r} = c_{p_1} P \frac{\varepsilon_p}{k_p} - c_{p_2}\frac{\varepsilon_p^2}{k_p} + \frac{\partial}{\partial x}\left[\left(\mu + \frac{\mu_t}{\sigma_\varepsilon}\right)\frac{\partial \varepsilon_p}{\partial x}\right] + \frac{1}{r}\frac{\partial}{\partial r}\left[r\left(\mu + \frac{\mu_t}{\sigma_\varepsilon}\right)\frac{\partial \varepsilon_p}{\partial r}\right] \tag{59}$$

$$\frac{\partial \rho \varepsilon_T}{\partial t} + \frac{\partial \rho U \varepsilon_T}{\partial x} + \frac{\partial r \rho V \varepsilon_T}{\partial r}$$

$$= c_{T_1} \frac{\varepsilon_p \varepsilon_T}{k_T} - c_{T_2} \frac{\varepsilon_T^2}{k_T} + \frac{\partial}{\partial x}\left[\left(\mu + \frac{\mu_t}{\sigma_\varepsilon}\right)\frac{\partial \varepsilon_T}{\partial x}\right] + \frac{1}{r}\frac{\partial}{\partial r}\left[r\left(\mu + \frac{\mu_t}{\sigma_\varepsilon}\right)\frac{\partial \varepsilon_T}{\partial r}\right] \quad (60)$$

where

$$P = \frac{\mu_t}{\rho}\left\{2\left[\left(\frac{\partial U}{\partial x}\right)^2 + \left(\frac{\partial V}{\partial r}\right)^2 + \boxed{\left(\frac{V}{r}\right)^2}\right] + \left(\frac{\partial U}{\partial r} + \frac{\partial V}{\partial x}\right)^2\right\} \quad (61)$$

$c_{p_1} = 2.2$

$c_{p_2} = 1.8 - 0.3\,[(k_p/k_T - 1)/(k_p/k_T + 1)]$

$c_{T_1} = 1.08\ \varepsilon_p/\varepsilon_T$

$c_{T_2} = 1.15$

Turbulence Model

$$\mu_t = \rho c_\mu \frac{(k_p + k_T)}{2}\frac{k_p}{\varepsilon_p}$$

$\sigma_k = 1.0$

$\sigma_\varepsilon = 1.3$

$c_\mu = 0.09$

$\mu_T = \mu_t + \mu$

C. Algebraic Stress Model

The algebraic stress model given below includes wall effects in both the the x- and r-directions. Here following Reece (Ref. 21) it is assumed that the influence of both sets of walls are simply additive, and there are no cross-correlations due to corner effects. Either or both of these wall effects can be removed by assigning a value of zero to their corresponding length-scale functions, f_x and f_r[†].

[†] f_x and f_y for planar flows.

Conservation of Mass

$$\frac{\partial \rho}{\partial t} + \frac{\partial \rho U}{\partial x} + \frac{1}{r}\frac{\partial r \rho V}{\partial r} = 0 \tag{62}$$

x-Momentum

$$\frac{\partial \rho U}{\partial t} + \frac{\partial \rho U^2}{\partial x} + \frac{1}{r}\frac{\partial r \rho UV}{\partial r}$$

$$= -\frac{\partial P}{\partial x} + \frac{\partial}{\partial x}\left(2\mu \frac{\partial U}{\partial x} - \rho\overline{u^2}\right) + \frac{1}{r}\frac{\partial}{\partial r}\left[r\mu\left(\frac{\partial U}{\partial r} + \frac{\partial V}{\partial x}\right) - r\rho\overline{uv}\right] \tag{63}$$

r-Momentum

$$\frac{\partial \rho V}{\partial t} + \frac{\partial \rho UV}{\partial x} + \frac{1}{r}\frac{\partial r \rho V^2}{\partial r}$$

$$= -\frac{\partial P}{\partial r} + \frac{\partial}{\partial x}\left[\mu\left(\frac{\partial V}{\partial x} + \frac{\partial U}{\partial r}\right) - \rho\overline{uv}\right] + \frac{1}{r}\frac{\partial}{\partial r}\left(2r\mu \frac{\partial V}{\partial r} - \rho r\overline{v^2}\right) - \boxed{2\mu \frac{V}{r^2} + \rho \frac{\overline{w^2}}{r}} \tag{64}$$

k Transport Equation

$$\frac{\partial \rho k}{\partial t} + \frac{\partial \rho Uk}{\partial x} + \frac{1}{r}\frac{\partial r \rho Vk}{\partial r}$$

$$= \rho P - \rho\varepsilon + \frac{\partial}{\partial x}\left(\mu \frac{\partial k}{\partial x} + \rho c_k \frac{k}{\varepsilon}\overline{u^2}\frac{\partial k}{\partial x} + \rho c_k \frac{k}{\varepsilon}\overline{uv}\frac{\partial k}{\partial r}\right)$$

$$+ \frac{1}{r}\frac{\partial}{\partial r}\left(\mu r \frac{\partial k}{\partial r} + r\rho c_k \frac{k}{\varepsilon}\overline{uv}\frac{\partial k}{\partial x} + r\rho c_k \frac{k}{\varepsilon}\overline{v^2}\frac{\partial k}{\partial r}\right) \tag{65}$$

ε Transport Equation

$$\frac{\partial \rho \varepsilon}{t} + \frac{\partial \rho U\varepsilon}{\partial x} + \frac{1}{r}\frac{\partial r \rho V\varepsilon}{\partial r}$$

$$= \rho c_{\varepsilon_1}\frac{\varepsilon}{k}P - \rho c_{\varepsilon_2}\frac{\varepsilon^2}{k} + \frac{\partial}{\partial x}\left(\mu \frac{\partial \varepsilon}{\partial x} + \rho c_{\varepsilon_3}\frac{k}{\varepsilon}\overline{u^2}\frac{\partial \varepsilon}{\partial x} + \rho c_{\varepsilon_3}\frac{k}{\varepsilon}\overline{uv}\frac{\partial \varepsilon}{\partial r}\right)$$

$$+ \frac{1}{r}\frac{\partial}{\partial r}\left(\mu r \frac{\partial \varepsilon}{\partial r} + r\rho c_{\varepsilon_3}\frac{k}{\varepsilon}\overline{uv}\frac{\partial \varepsilon}{\partial x} + r\rho c_{\varepsilon_3}\frac{k}{\varepsilon}\overline{v^2}\frac{\partial \varepsilon}{\partial r}\right) \tag{66}$$

where

$$P = -\left[\overline{u^2}\frac{\partial U}{\partial x} + \overline{v^2}\frac{\partial V}{\partial r} + \overline{uv}\left(\frac{\partial U}{\partial r} + \frac{\partial V}{\partial x}\right) + \boxed{\overline{w^2}\frac{V}{r}}\right] \tag{67}$$

Turbulence Model

$$-\rho\overline{u^2} = \Gamma[(2 + 4a_{1x} + a_{1r})(e_u + 2/3)\frac{\partial U}{\partial x} + 3a_{2x}(e_u + 2/3)$$

$$- (1 + 2a_{1x} + 2a_{1r})(e_v + 2/3)\frac{\partial V}{\partial r} - 1.5a_{2r}(e_v + 2/3)$$

$$\boxed{- (1 + 2a_{1x} - a_{1r})(e_w + 2/3)\frac{V}{r}}$$

$$+ (2 + 4a_{1x} + a_{1r})\, e_{uv}\frac{\partial U}{\partial r} - (1 + 2a_{1x} + 2a_{1r})\, e_{uv}\frac{\partial V}{\partial x}] - 2/3\rho k \qquad (68)$$

$$-\rho v^2 = \Gamma[-(1 + 2a_{1x} + 2a_{1r})(e_u + 2/3)\frac{\partial U}{\partial x} - 1.5\, a_{2x}(e_u + 2/3)$$

$$+ (2 + a_{1x} + 4a_{1r})(e_v + 2/3)\frac{\partial v}{\partial r} + 3a_{2r}(e_v + 2/3)$$

$$\boxed{- (1 - a_{1x} + 2a_{1r})(e_w + 2/3)\frac{V}{r}}$$

$$- (1 + 2a_{1x} + 2a_{1r})\, e_{uv}\frac{\partial U}{\partial r} + (2 + a_{1x} + 4a_{1r})\, e_{uv}\frac{\partial V}{\partial x}] - 2/3\rho k \qquad (69)$$

$$-\rho\overline{w^2} = \Gamma[-(1 + 2a_{1x} - a_{14})(e_u + 2/3)\frac{\partial U}{\partial x} - 1.5a_{2x}(e_u + 2/3)$$

$$- (1 - a_{1x} + 2a_{1r})(e_v + 2/3)\frac{\partial V}{\partial r} - 1.5a_{2r}(e_v + 2/3)$$

$$\boxed{+ (2 + a_{1x} + a_{1r})(e_w + 2/3)\frac{V}{r}}$$

$$- (1 + 2a_{1x} - a_{1r})\, e_{uv}\frac{\partial U}{\partial r} - (1 - a_{1x} + 2a_{1r})\, e_{uv}\frac{\partial V}{\partial x}] - 2/3\rho k \qquad (70)$$

$$-\rho\overline{uv} = \Gamma[1.5(1 + 1.5a_{1x} + 1.5a_{1r})(e_u + 2/3)\frac{\partial V}{\partial x}$$

$$+ 1.5(1 + 1.5a_{1x} + 1.5a_{1r})(e_v + 2/3)\frac{\partial U}{\partial r}$$

$$\boxed{+ 1.5(1 + 1.5a_{1x} + 1.5a_{1r})\, e_{uv}\frac{V}{r}} + 2.25(a_{2x} + a_{2r})e_{uv}] \qquad (71)$$

where

$$a_{1x} = c_2 c_2' f_x/(1 - c_2) \qquad a_{1r} = c_2 c_2' f_r/(1 - c_2)$$

$$a_{2x} = c_1' \frac{\varepsilon}{k} f_x/(1 - c_2) \qquad a_{2r} = c_1' \frac{\varepsilon}{k} f_r/(1 - c_2)$$

$$\Gamma = 2/3\rho k^2/\varepsilon \qquad \lambda = (1 - c_2)/((c_1 - 1) + P/\varepsilon)$$

$$e_u = (\overline{u^2} - 2/3k)/k \qquad e_v = (\overline{v^2} - 2/3k)/k$$

$$e_w = (\overline{w^2} - 2/3k)/k \qquad e_{uv} = \overline{uv}/k$$

$$f_x = \begin{cases} \dfrac{k^{3/2}/\varepsilon}{\kappa/a^{3/2}x} & \text{single wall} \\ \dfrac{k^{3/2}/\varepsilon}{\kappa/a^{3/2}\left[\dfrac{1}{(1/x) + (1/L - x)}\right]} & \text{parallel walls} \end{cases}$$

$$f_r = \begin{cases} \dfrac{k^{3/2}/\varepsilon}{\kappa/a^{3/2}r} & \text{single wall} \\ \dfrac{k^{3/2}/\varepsilon}{\kappa/a^{3/2}\left[\dfrac{1}{(1/r) + (1/h - r)}\right]} & \text{parallel walls (e.g. coaxial pipes)} \end{cases}$$

c_k, c_{ε_1}, c_{ε_2}, c_{ε_3}, c_1, c_2, c_1' and c_2' are constants defined in Table 2.1, and L and h are the distances of separation, respectively, between the parallel walls in the x- and r-directions. κ is the von Karman constant (0.4187) and "a" is the near-wall value of $-\overline{uv}/k$ (generally taken as 0.25).

3. ASSESSMENT OF TURBULENCE MODELS FOR SCRAMJET APPLICATIONS

Three major areas were considered in the assessment of turbulence models for scramjet applications carried out under this program. These areas involved the development of a compressibility correction technique to extend the accurate prediction capability of the thin shear-layer MDLS or k-ε models to highly supersonic flows; the investigation of the performance capabilities of the k-ε, MDLS, and ASM models (and the modified k-ε and ASM approaches outlined in Section 2) in subsonic recirculating flows, both planar and axisymmetric; and the development of the k-ε and ASM approaches for the prediction of supersonic recirculating flows. In the latter two areas problems of turbulence model application were encountered that highlight the interaction between turbulence modeling and numerical solution techniques, and these problems and their solution are described in the subsequent discussions.

3.1 COMPRESSIBILITY CORRECTION APPROACH

The basic approach followed in the development of a compressibility correction technique involved the introduction of a modification to the term representing the dissipation rate production in the dissipation rate expression. Using the approximation introduced by Hanjalic, Launder and Sindir and given by equation (32), this expression becomes, for thin shear flows

$$\frac{\varepsilon}{k} P_K = \rho(c_{P_1} c_\mu + c'_{P_1}) \, k\left(\frac{\partial U}{\partial r}\right)^2 \tag{72}$$

For the MDLS model, $c_{P_1} = 2.2$ and $c_\mu = 0.09$. As described in preliminary form in Ref. 2, the form of the correction was taken to be

$$c_{P1}' = -0.11 + aM^b \tag{73}$$

for $M \geq 1$, where the coefficients a and b are determined from a parametric examination of supersonic jet core length and supersonic shear layer growth rate predictions. Results of a trial-and-error correlation of supersonic jet core length data produced a coefficient fit of the form

$$c_{P1}' = -0.11 + 0.0075M, \ (M \geq 1) \tag{74}$$

that is, a = 0.0075 and b = 1, where M is the local Mach number which varies radially and axially throughout the flow. The results of MDLS model predictions of jet core lengths are shown in Figure 3.1, as compared to data from a variety of sources (Refs. 30-35), and it can be seen from the figure that the increase in jet core length as a function of Mach number that occurs for M > 1 is well represented. Without the correction given by equation (74), the predicted core length trend for M > 1 is equal to that seen in Figure 3.1 for M < 1. Results obtained using this correlation with the MDLS model were also compared with the supersonic shear layer growth rate data correlation described in Ref. 38, as shown on Figure 3.2. While the agreement between the predicted shear layer growth rates and those obtained from the experimental data correlation of Ref. 36 is not as good as for the supersonic jet potential core lengths, the predicted results are in considerably better agreement with the overall trend of the data using the correction given by equation (74) than are results obtained with no correction (Ref. 1), in which there is essentially no change in shear layer growth rate with Mach number for M > 1.

It should be noted that the sensitivity of jet potential core length and shear layer growth rate to Mach number exhibited in Figures 3.1 and 3.2 is independent of the observed sensitivity of these parameters to other aspects of the flowfield initial conditions. For example, it is well known that potential core lengths for subsonic, essentially incompressible round jets are strongly dependent on the state of flow at the jet exit: laminar, thin boundary layer exit conditions produce considerably shorter core lengths than do exit conditions which involve thicker, turbulent boundary layers. This phenomenon is related to the presence just downstream of the jet exit, in the thin laminar boundary layer case, of vortical large scale structures which produce locally large mixing rates. These structures do not develop if the jet exit flow involves thicker turbulent boundary layers. In the case of the present computations (and the experiments to which their results are compared) the initial condition in all cases involved a relatively thick turbulent boundary layer at the jet nozzle exit. Thus the other aspects of initial condition specification,

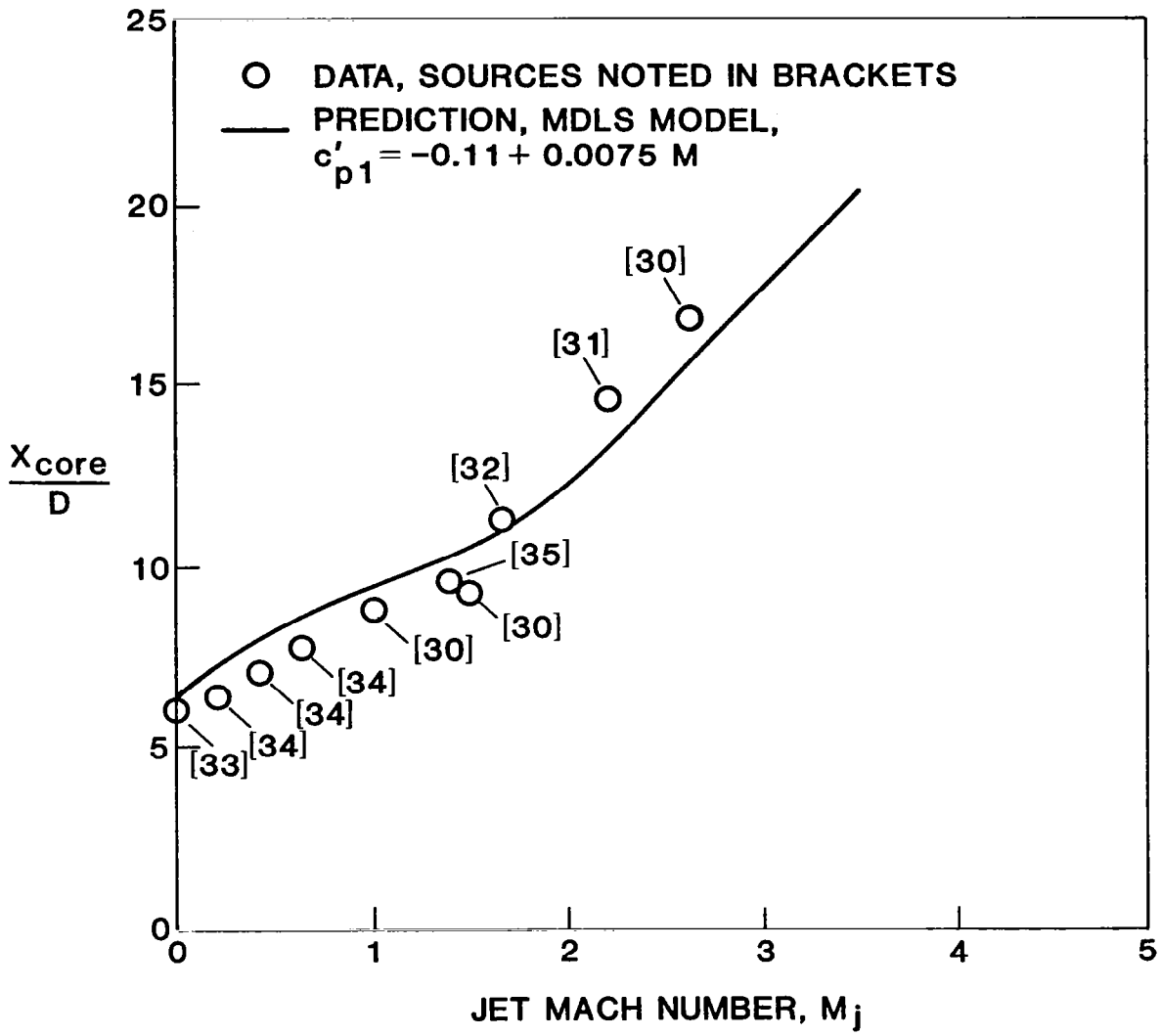

FIGURE 3.1. Comparison of Compressibility Correction Results With Data for Jet Core Length as a Function of Mach Number.

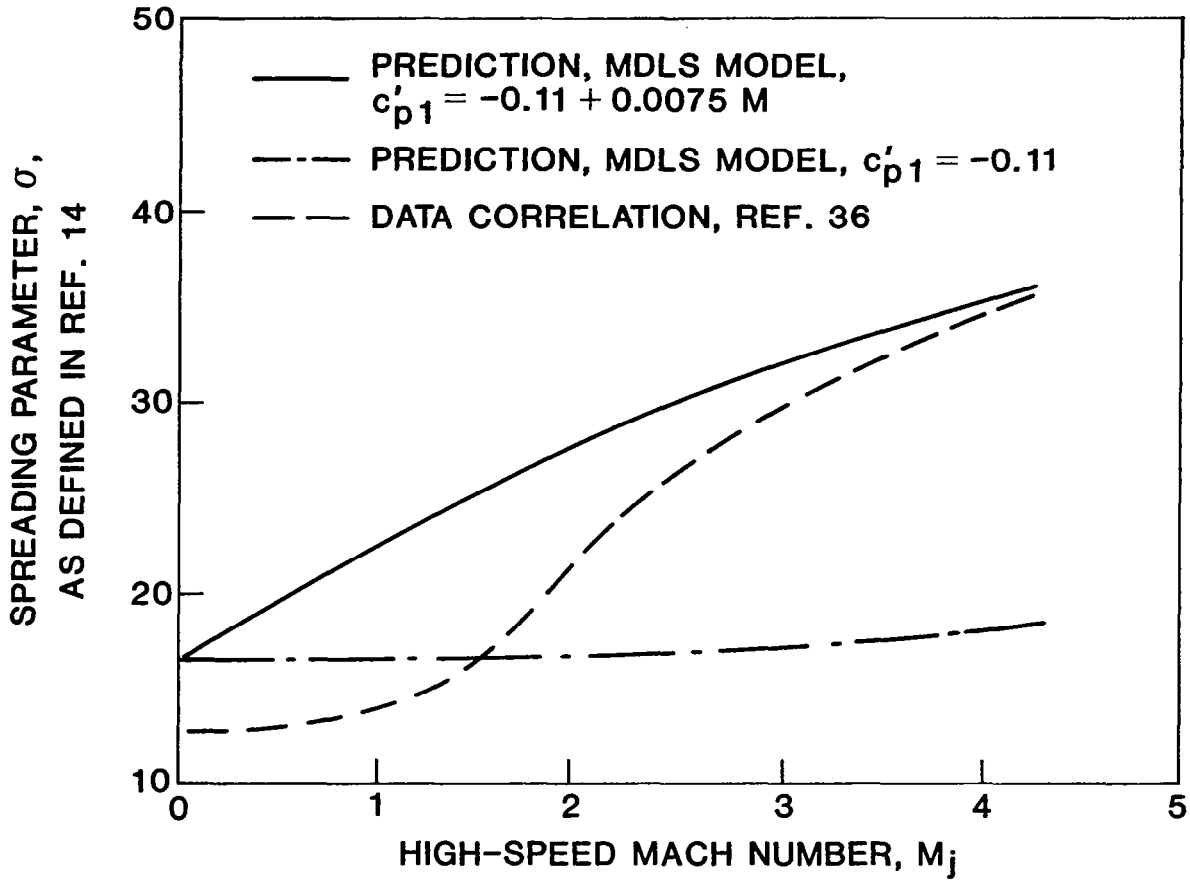

FIGURE 3.2. Comparison of Compressibility Correction Results With Data for Shear Layer Growth Rate as a Function of Mach Number.

which also affect the determination of velocity potential core lengths, do not enter the comparisons just discussed.

3.2 ASSESSMENT OF MODELS FOR SUBSONIC RECIRCULATING FLOWS

3.2.1 Planar Flows

The predictive capabilities of a total of six turbulence models were examined for planar backward-facing step flows using the STEP family of elliptic codes (Ref. 5). The turbulence models were the k-ε model, the multi-dissipation-length-scale model, the algebraic stress model (only cross-stream† wall effects), "modified" k-ε model, "modified" algebraic stress model (only cross-stream wall effects), and multi-wall algebraic stress model (both cross-stream and streamwise†† wall effects). These models have been discussed in detail in Chapter 2.

Before definitive predictions of the test cases were obtained, (i.e., grid-independent and fully converged), a preliminary study was conducted to assess the relative predictive capability of the models. The multi-dissipation-length-scale (MDLS) model when applied to backward-facing step flow computations failed to improve on the standard k-ε model predictions. However, the concept of multiple time and length scales is physically sound, and is also appealing in the sense that it enables separate modeling of turbulent processes proceeding at different rates. A more extensive optimization of the coefficients than was done by Hanjalic et al. (Ref. 3) may be necessary to extend the predictive capability of this model beyond free shear flows. For the work described here the MDLS model was abandoned in favor of the k-ε model.

The idea behind the multi-wall ASM formulation was to account for the streamwise wall effects on the stress field, and thus try to capture the corner eddy that was missing in the previous calculations. Experimental observations (Refs. 37-39) indicate a two-eddy structure in all backward-facing step flows as shown in Figure 3.3.

---

†Influence of walls parallel to the streamwise direction, such as the top and bottom walls in backward-facing step geometries.

††Influence of walls normal to the streamwise direction, such as the rearward face of the face.

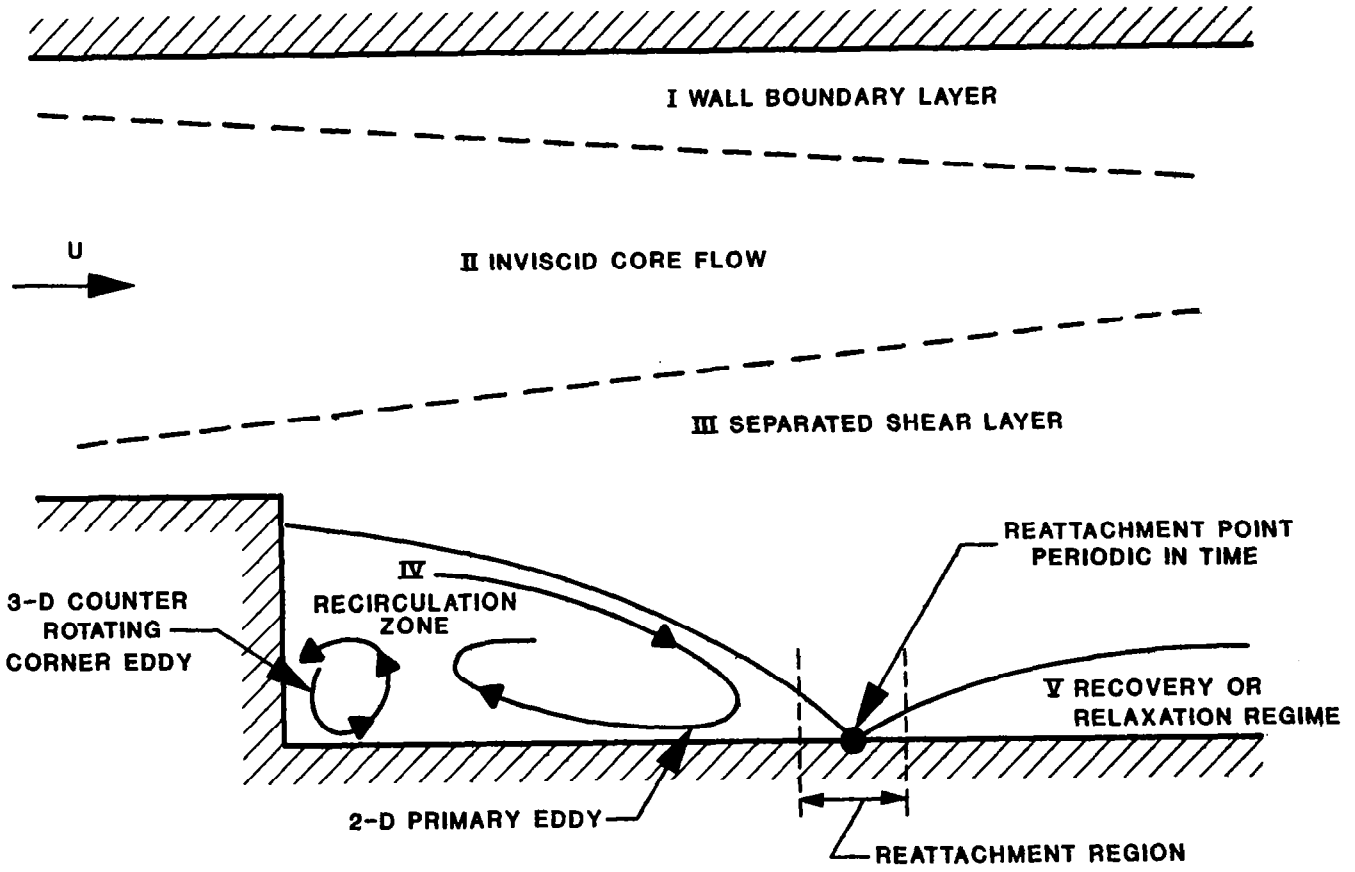

FIGURE 3.3. Streamline Pattern for Separating and Reattaching Flows in Backward-Facing Step Geometries

The three dimensional counter-rotating corner eddy which involves lateral as well as streamwise and transverse variations extends only a short distance (usually less than a step height) downstream of the step, and a large two-dimensional primary eddy which involves only streamwise and transverse variations occupies the rest of the recirculation zone. Figure 3.3 shows these two eddies and the other flow regimes encountered in backward-facing step geometries. In this type of flow, probably the one most informative yet simple describing parameter is the reattachment length defined as the distance from the step to the point where the separated shear layer attaches to the surface[†]. This, of course, is equal to the combined length of the two eddies. All flow parameters in the reverse flow as well as in the adjacent recovery region seem to correlate with this quantity, hence an accurate estimate of the reattachment length is essential for successful mean flow and turbulence field predictions. Since the reattachment length predicted by the ASM generally falls short of the experimental values by about a step height, it was conjectured that, if this corner eddy does grow in magnitude (due to streamwise wall effects), it would "push" the reattachment length further downstream and thus bring the computed values closer to the measurements. The reattachment length results are given in Table 3.1 for the Kim, Kline and Johnston 3:1 expansion ratio study (Ref. 39). The differences between the multi-wall and standard ASM (i.e., including cross-stream wall effects only) appear insignificant. The U-velocity, skin friction and peak $\overline{uv}$ profiles presented in Figures 3.4 through 3.6 also show no significant changes between the two versions of the model. However, contrary to expectations, the multi-wall treatment predicts shorter reattachment lengths (by about 2%) and smaller corner eddies. The shortcomings of the multi-wall ASM are probably due to the cross correlations between the perpendicular walls that are not included in the present version, which adopts Reece's hypothesis (Ref. 21) that perpendicular wall effects are simply additive and cross correlations are small enough to be neglected. The only other suggestion available in the literature, to the best of our knowledge, is Gessner and Eppich's proposal (Ref. 41) of an "image point" approach. This idea is still in a development stage and

[†]The point of reattachment is taken as the point where the shear stress vanishes.

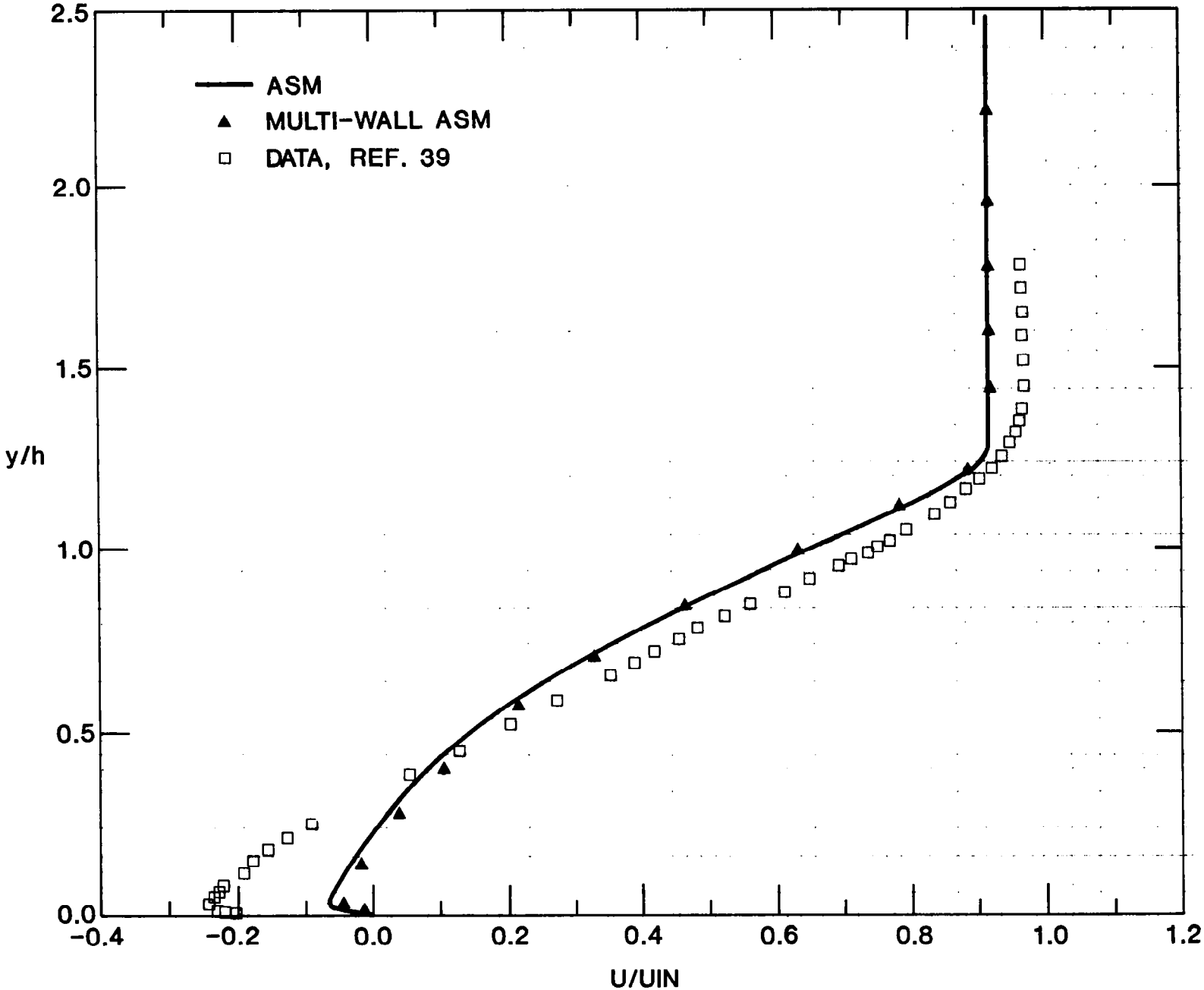

FIGURE 3.4. U-Velocity Profiles at Streamwise Location x/h = 5.333. 3:1 Area Ratio Planar Expansion, UIN = 18.2 m/s. Data From Kim, Kline and Johnston, Ref. 39.

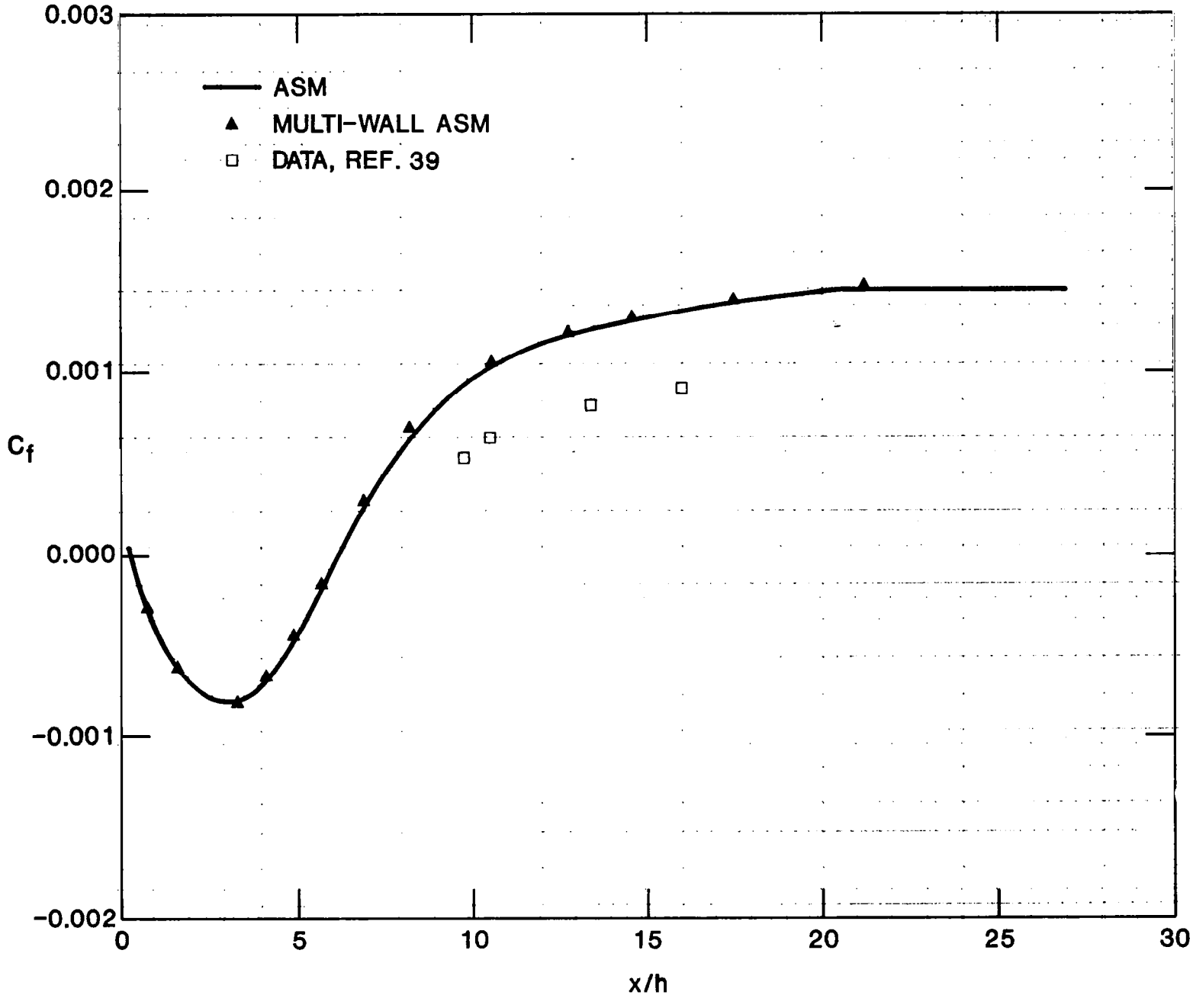

FIGURE 3.5. Bottom Wall Skin Friction Coefficient. 3:1 Area Ratio Planar Expansion. Data From Kim, Kline and Johnston, Ref. 39.

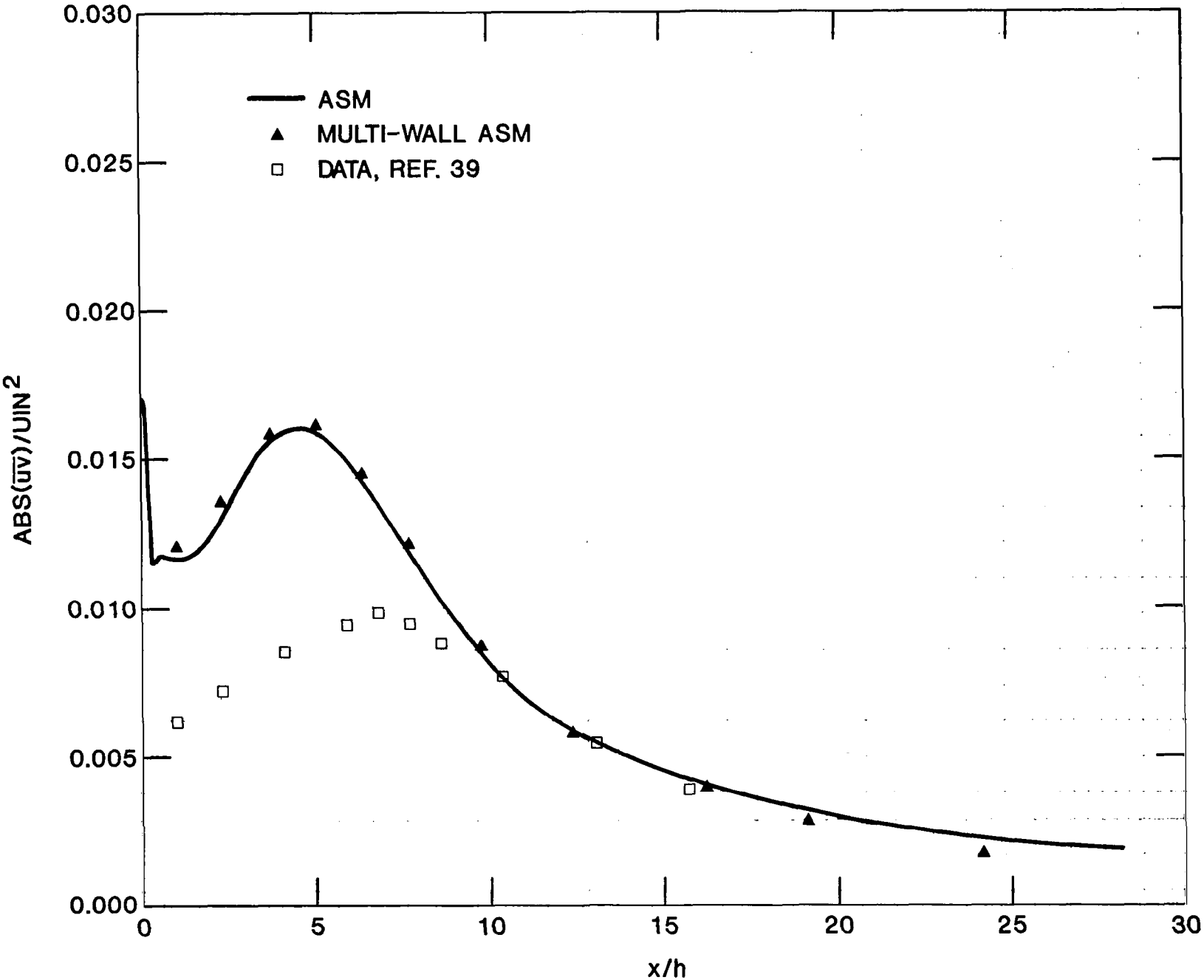

FIGURE 3.6. Maximum $\overline{uv}$ Distribution Along the Channel. 3:1 Area Ratio Planar Expansion, UIN = 18.2 m/s. Data From Kim, Kline and Johnston, Ref. 39.

is not well tested even for simple shear flows. Therefore, implementation of this scheme into recirculating flow computations does not seem appropriate for the present. The multi-wall ASM was not pursued further in plane backward-facing step flow calculations.

TABLE 3.1. Reattachment Length Predictions for the Kim, Kline and Johnston Study (3:1 Expansion Ratio)

Models	Reattachment Length in Step Heights
ASM	6.16
Multi-wall ASM	6.02
Measurements	7 ± 1

Upon completion of the preliminary study (which eliminated two of the original six models) definitive predictions of the test cases were carried out using the k-ε, "modified" k-ε, ASM, and "modified" ASM models for the solution domain shown in Figure 3.7. Reattachment length results are given in Table 3.2. Predicted and measured profiles of U-velocity and shear stress ($\overline{uv}$) are compared for three different expansion ratios. These results are now discussed[†] in more detail.

A. U-Velocity Predictions

Figures 3.8 through 3.10 present, at selected streamwise locations, the measured and predicted U-velocity profiles for the 3:1 and 4:1, and the predicted profiles for the 9:1 expansion ratios, respectively. A study of these results produces two important observations: one is that the relative performance of the models is region-dependent, i.e., best predictions are not

[†]Complete sets of predictions for U, V, P, k, ε, $\overline{u^2}$, $\overline{v^2}$, $\overline{w^2}$, $\overline{uv}$, P, μ_t and P/ε are available for all 3 test cases and 4 models (except for the normal Reynolds stresses with the k-ε models) at 40 streamwise stations. To keep the presentation manageable profiles for a given variable are presented at representative stations and for selected expansion ratios only. However, discussions to follow are based on the complete set of results that are kept on file at SAI. Further documentation of the results is given in Ref. (5).

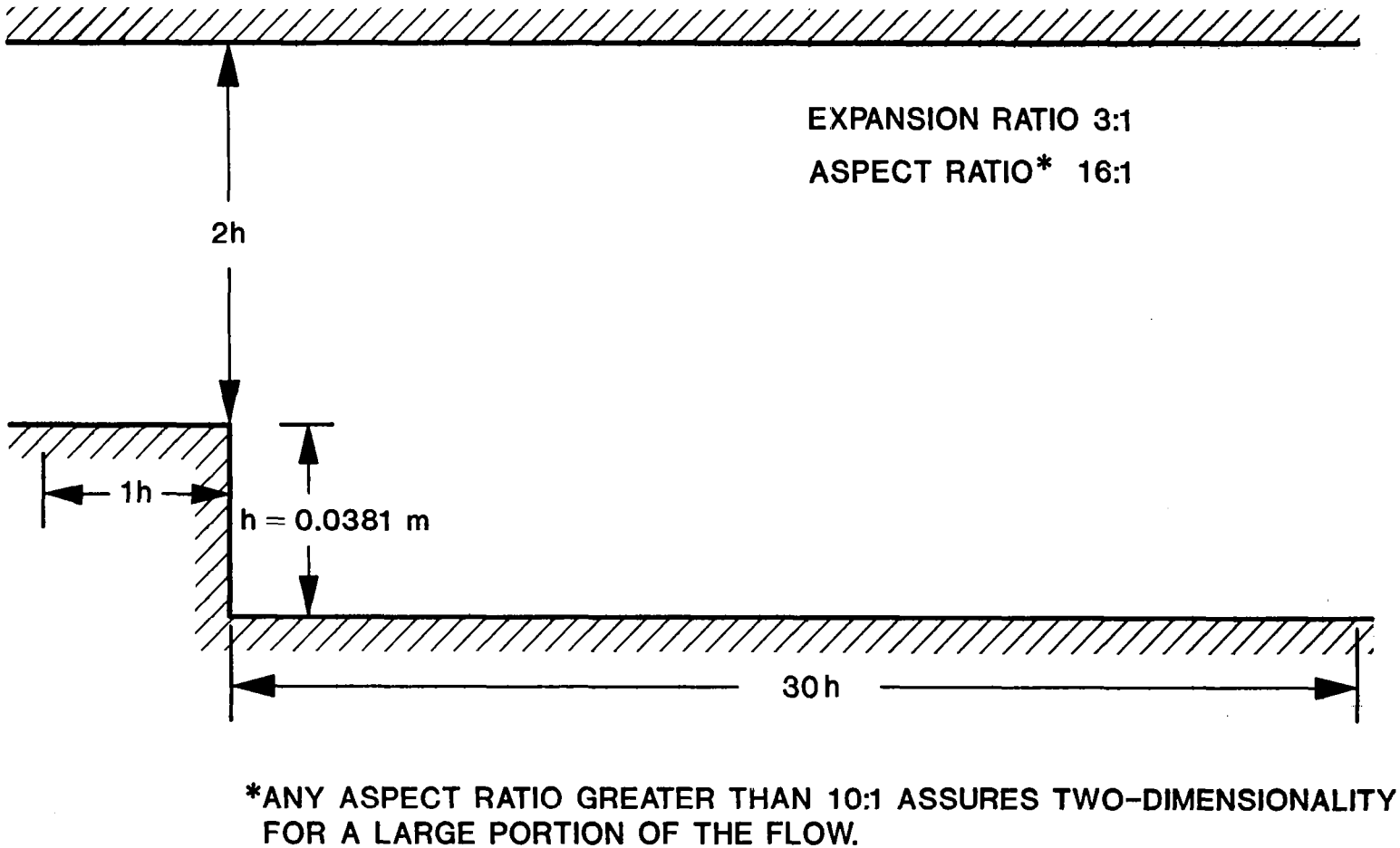

FIGURE 3.7. Solution Domain Used in the Calculations.

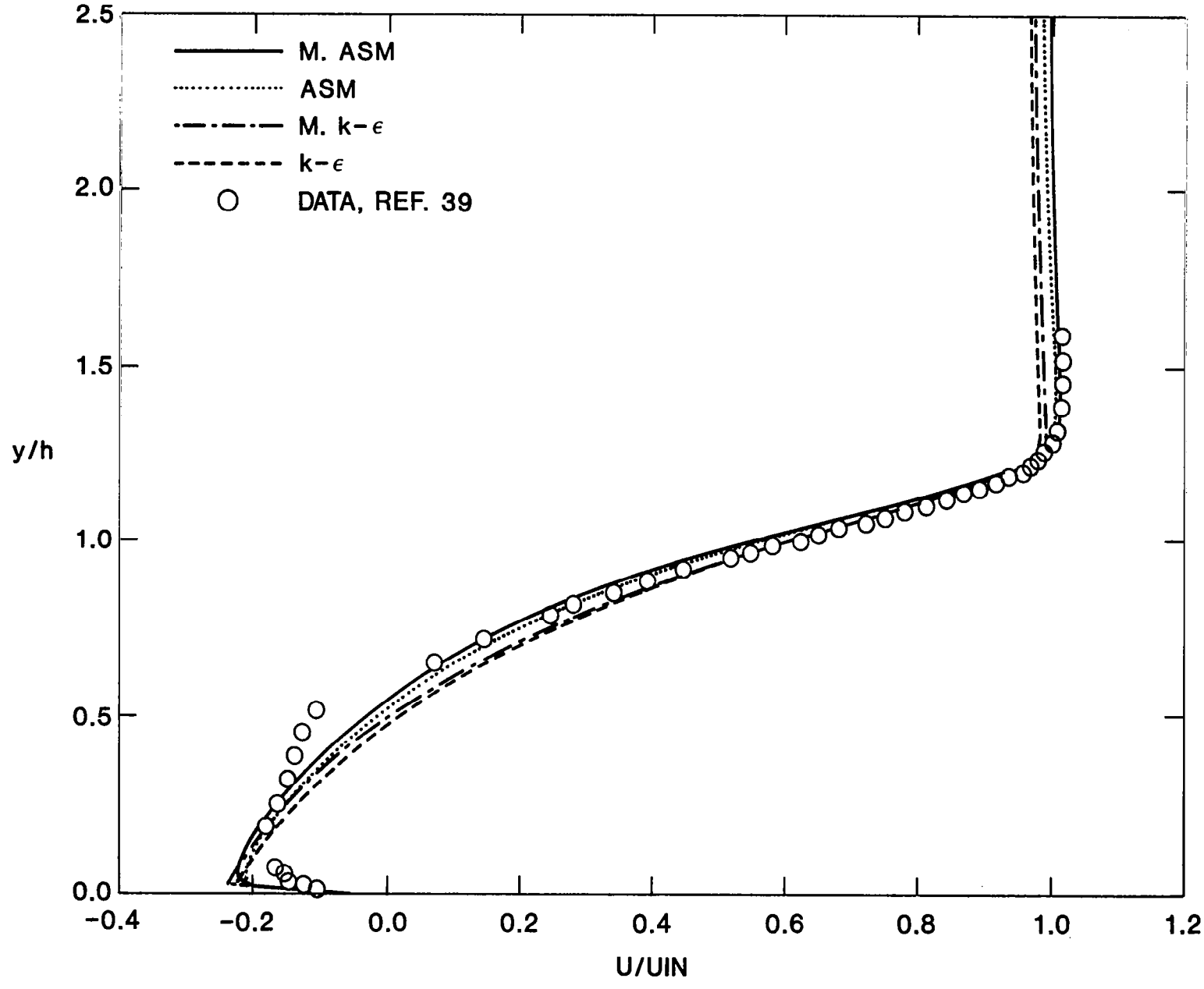

FIGURE 3.8a. U-Velocity Profiles at Streamwise Location x/h = 2.667.
3:1 Area Ratio Planar Expansion, UIN = 18.2 m/s.
Data From Kim, Kline and Johnston, Ref. 39.

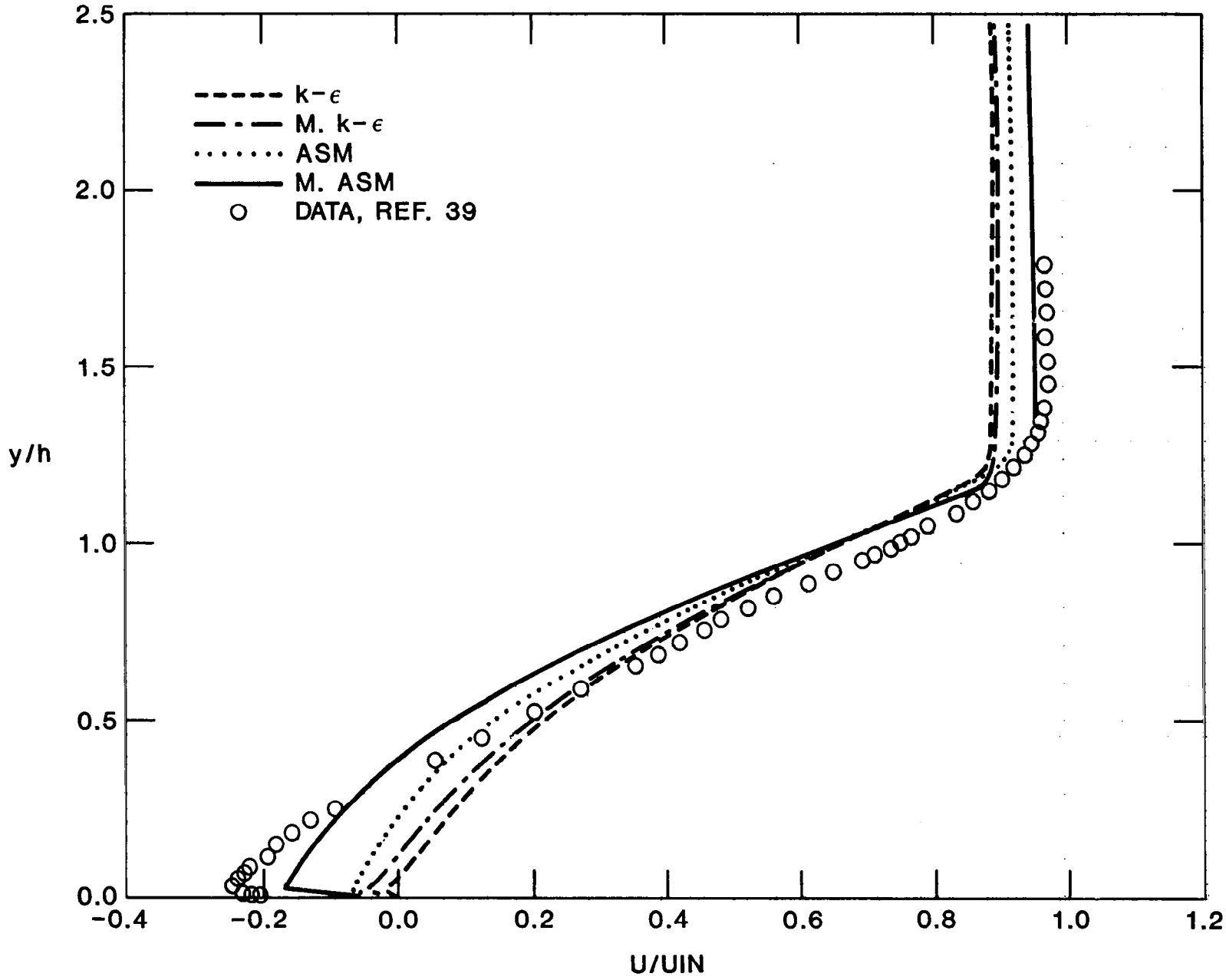

FIGURE 3.8b. U-Velocity Profiles at Streamwise Location x/h = 5.333. 3:1 Area Ratio Planar Expansion, UIN = 18.2 m/s. Data From Kim, Kline and Johnston, Ref. 39.

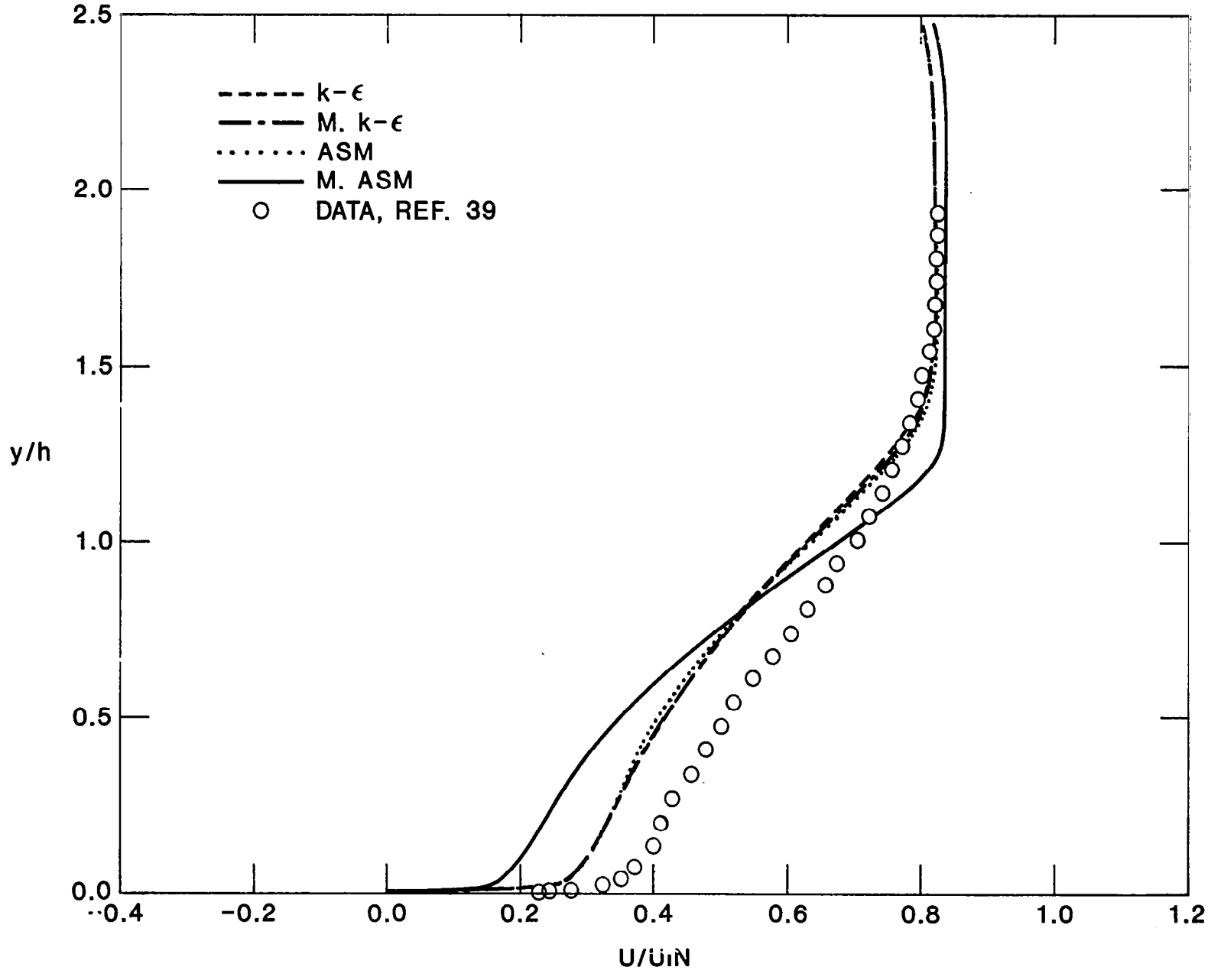

FIGURE 3.8c. U-Velocity Profiles at Streamwise Location x/h = 10.667.
3:1 Area Ratio Planar Expansion, UIN = 18.2 m/s.
Data From Kim, Kline and Johnston, Ref. 39.

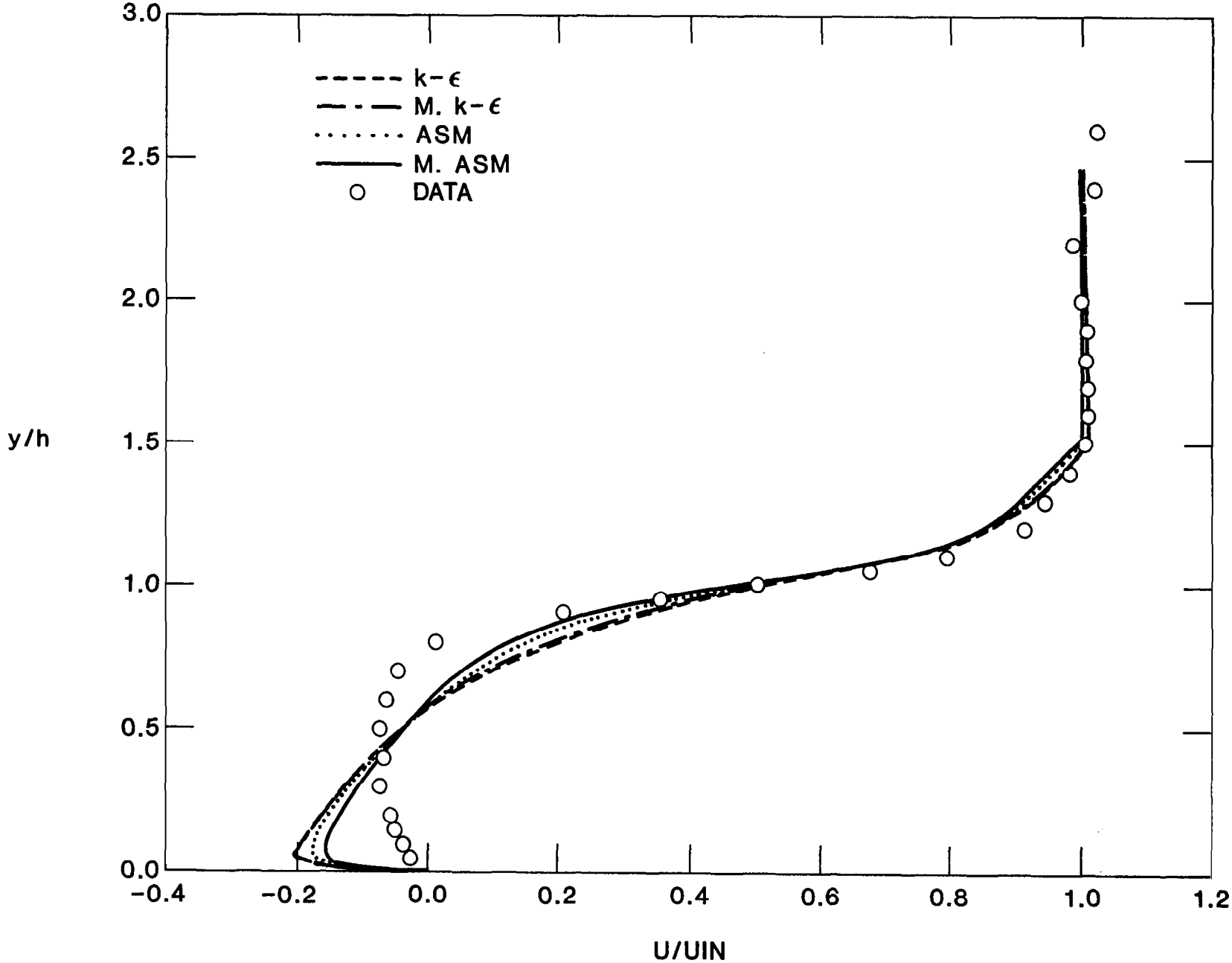

FIGURE 3.9a. U-Velocity Profiles at Streamwise Location x/h = 4.0.
4:1 Area Ratio Planar Expansion, UIN = 44.2 m/s.
Data From Driver and Seegmiller, Private Communication.

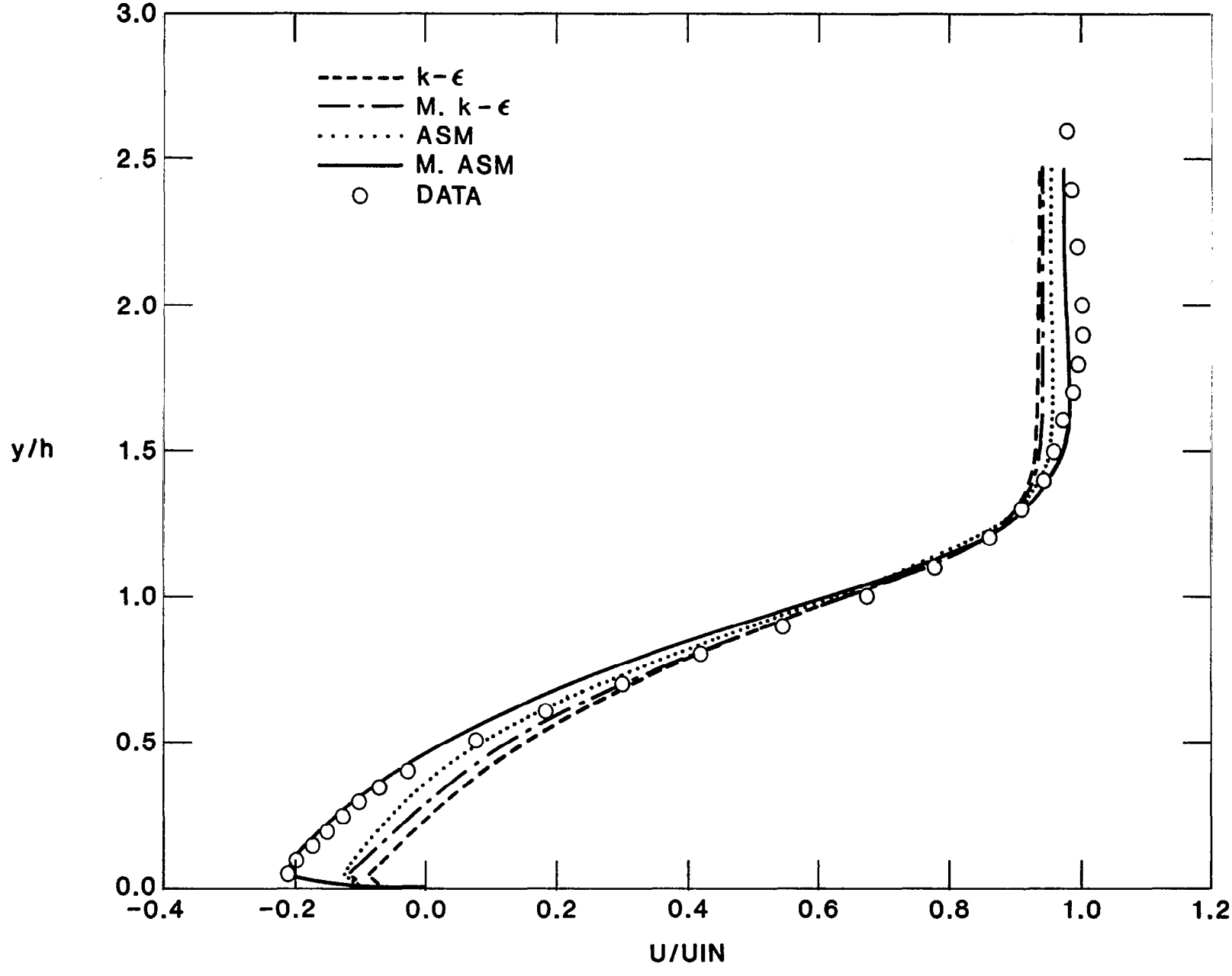

FIGURE 3.9b. U-Velocity Profiles at Streamwise Location x/h = 4.0.
4:1 Area Ratio Planar Expansion, UIN = 44.2 m/s.
Data From Driver and Seegmiller, Private Communication.

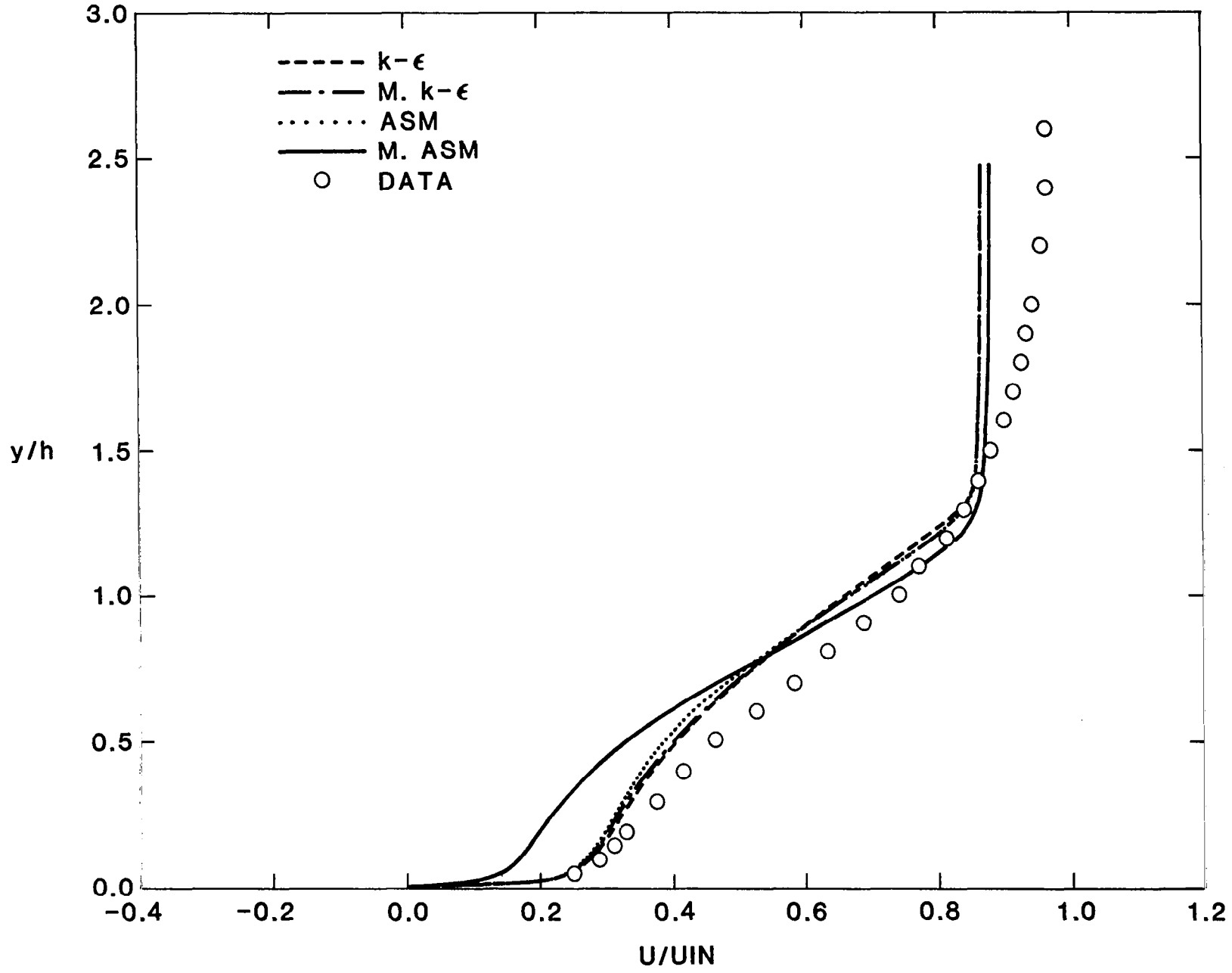

FIGURE 3.9c. U-Velocity Profiles at Streamwise Location x/h = 8.63.
4:1 Area Ratio Planar Expansion, UIN = 44.2 m/s.
Data From Driver and Seegmiller, Private Communication.

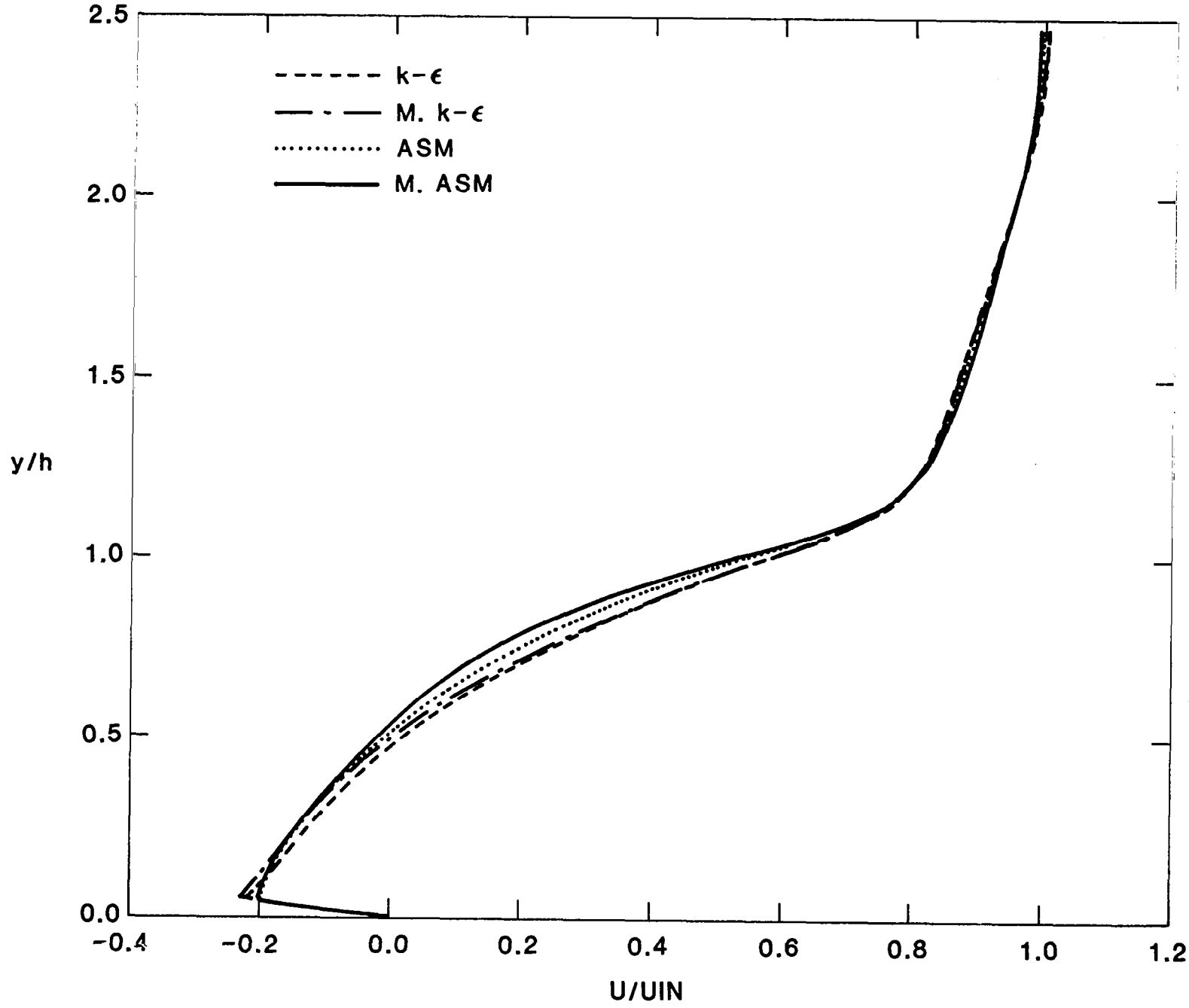

FIGURE 3.10a. U-Velocity Profiles at Streamwise Location x/h = 2.0. 9:1 Area Ratio Planar Expansion, UIN = 44.2 m/s.

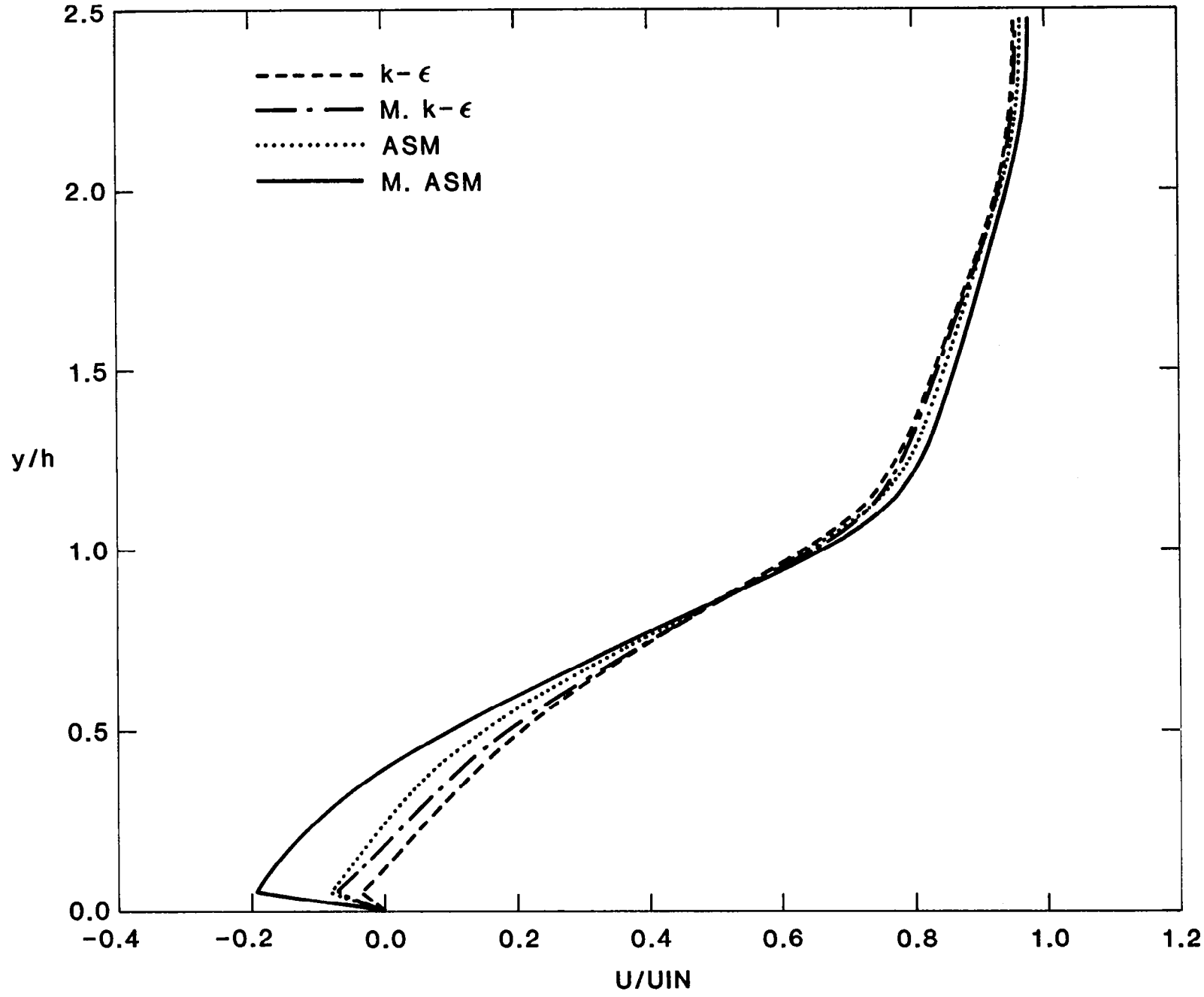

FIGURE 3.10b. U-Velocity Profiles at Streamwise Location x/h = 4.0.
9:1 Area Ratio Planar Expansion, UIN = 44.2 m/s.

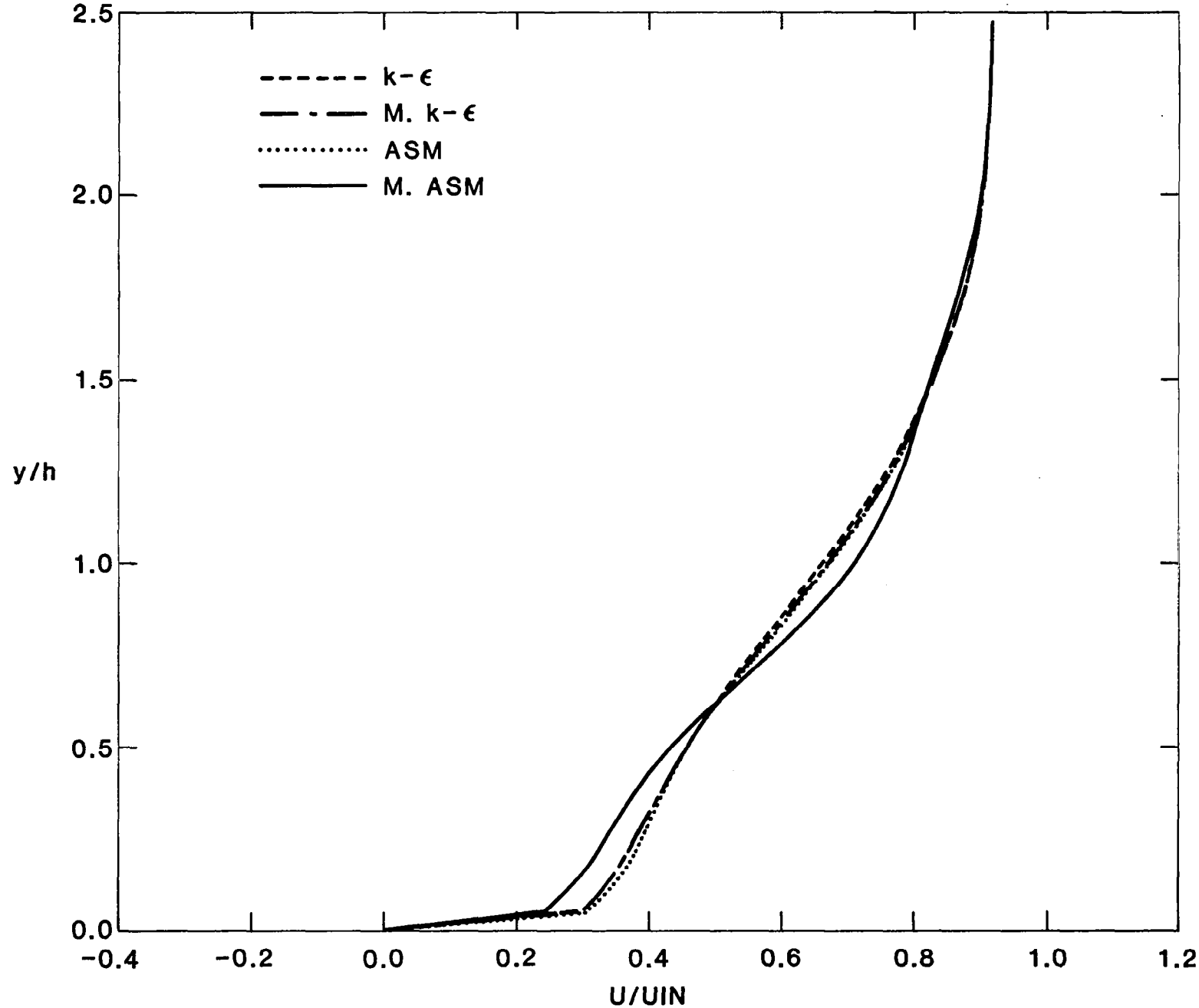

FIGURE 3.10c. U-Velocity Profiles at Streamwise Location x/h = 8.63. 9:1 Area Ratio Planar Expansion, UIN = 44.2 m/s.

necessarily obtained by the same model in both the reverse flow and recovery regions; and secondly, within a given region the established trends do not vary with expansion ratio.

TABLE 3.2 Variation of Reattachment Length With Expansion Ratio[†]

Expansion Ratio	Reattachment Length in Step Heights (h)				
	k-ε	"Modified" k-ε	ASM	"Modified" ASM	Measurements
3:1, (40)	5.36	5.81	6.16	7.77	7 ± 1
4:1[††],	4.98	5.26	5.40	6.92	7.00 ± 0.20
9:1, (39)	4.29	4.56	4.65	5.79	6.25 ± 0.25

The U-velocity profiles are now discussed starting with the recirculation zone. There the "modified" ASM displays the best agreement with data for all expansion ratios. The differences between the remaining models are relatively small with the ASM, "modified" k-ε, and k-ε models showing, in that order, lesser degrees of agreement. Since they all underestimate the size of the reverse flow region as shown in Table 3.2 it is natural that the predicted velocities would suffer from "scaling" problems. The maximum mean reverse flow velocities, U/U_{in}, are given in Table 3.3 for all models and expansion ratios. The magnitude of this velocity seems to decrease slightly with increasing expansion ratio. Measured values are also reported in that table, however these probably do not represent the true maxima since relatively few measuring stations were employed in this region (most of them were at least 2 step heights apart). Nevertheless, the agreement is surprisingly good. Overall, it was to be

[†]Results were obtained with a non-uniform grid of 42 by 42 nodes for a solution domain length of 31 step heights (1h before the expansion and 30 downstream of the step). Computations were started at x/h = -1 with the measured inlet velocity profiles. The inlet kinetic energy and dissipation rates were calculated from this profile using Prandtl's mixing length hypothesis. The convergence criterion (the maximum acceptable level of the residual sources) was set to 0.001.

[††]Private communication. Driver, D. M., and Seegmiller, H. L.; NASA-Ames Research Center, STE Branch, 1981.

expected that the "modified" ASM would show the best agreement with data, since, within the recirculation zone, the U-velocities are closely correlated with the reattachment length. This is further supported by the fact that the "modified" ASM predicts the lowest spreading rate for the separated shear layer and also displays the best agreement with the measured shear stress profiles.

TABLE 3.3. Peak Mean Reverse Flow Velocities and Locations

Expansion Ratio	Model	Peak Mean Reverse Flow Velocity U/Ū in		Location in Step Heights x/h	
		Predicted	Measured†	Predicted	Measured†
3:1(α=0°)	ASM	- 0.210	- 0.243	2.550	5.333
	M.ASM	- 0.230		3.210	
	k-ε	- 0.239		2.120	
	M.k-ε	- 0.245		2.340	
4:1(α=0°)	ASM	- 0.206	- 0.213	2.340	4.000
	M.ASM	- 0.229		3.210	
	k-ε	- 0.235		1.950	
	M.k-ε	- 0.240		2.120	
9:1(α=0°)	ASM	- 0.198		2.340	
	M.ASM	- 0.229		2.980	
	k-ε	- 0.226		1.590	
	M.k-ε	- 0.235		1.950	

Downstream of the recirculation zone the predicted recovery of the U-velocity profiles is slow compared to the measurements at all expansion ratios.

†The experimental values given here probably do not represent the true maxima since relatively few measuring stations were employed in the recirculation region.

Here the predictions by the ASM, "modified" k-ε and k-ε models are hardly distinguishable from each other, and in general show fair agreement with data. When plotted against the actual downstream distance from the step the "modified" ASM seems to suffer from an even slower recovery rate. If the streamwise distance is normalized relative to the predicted reattachment points[†], the differences between models diminish. However, the "modified" ASM still displays a somewhat different behavior from the other models. Close to the wall it consistently predicts lower velocities up to an inflection point (at a y/h of about 0.9) followed by a swift increase (more so than the other models) to the freestream values. This behavior can be partially explained by examining the computed shear stress profiles. Profiles predicted by the "modified" ASM generally reach their peak closer to the wall and drop sooner to the freestream levels than the other models. This could explain the more prominent inflective point and the faster rise to the freestream levels in the corresponding velocity predictions. Close to the wall there is practically no difference in all the predicted $\overline{uv}$ profiles, so the lower velocities of the modified" ASM must be due to transport effects (less momentum carry-over due to the larger reverse flow region) and to the action of the normal stresses (the magnitude of predicted $-\partial(\rho\overline{u^2})/\partial x$ is smaller for the "modified" version). The differences between the models in this region diminish with increasing expansion ratio and streamwise distance.

B. Shear Stress Predictions

Figures 3.11 through 3.13 present at given streamwise locations the measured and predicted $\overline{uv}$ profiles for the 3:1 and 4:1, and the predicted profiles for the 9:1 expansion ratios, respectively.

An analysis of these figures reveals similar trends in the $\overline{uv}$ profiles at all expansion ratios. Within two step heights downstream of the step, the measured $\overline{uv}$ profiles initially assume small gradually decreasing positive values that eventually change sign, and sharply increase in magnitude to a negative

---

[†]This takes into account the variation in the starting point of the forward flow which may be responsible for the apparent differences between the predicted recovery rates.

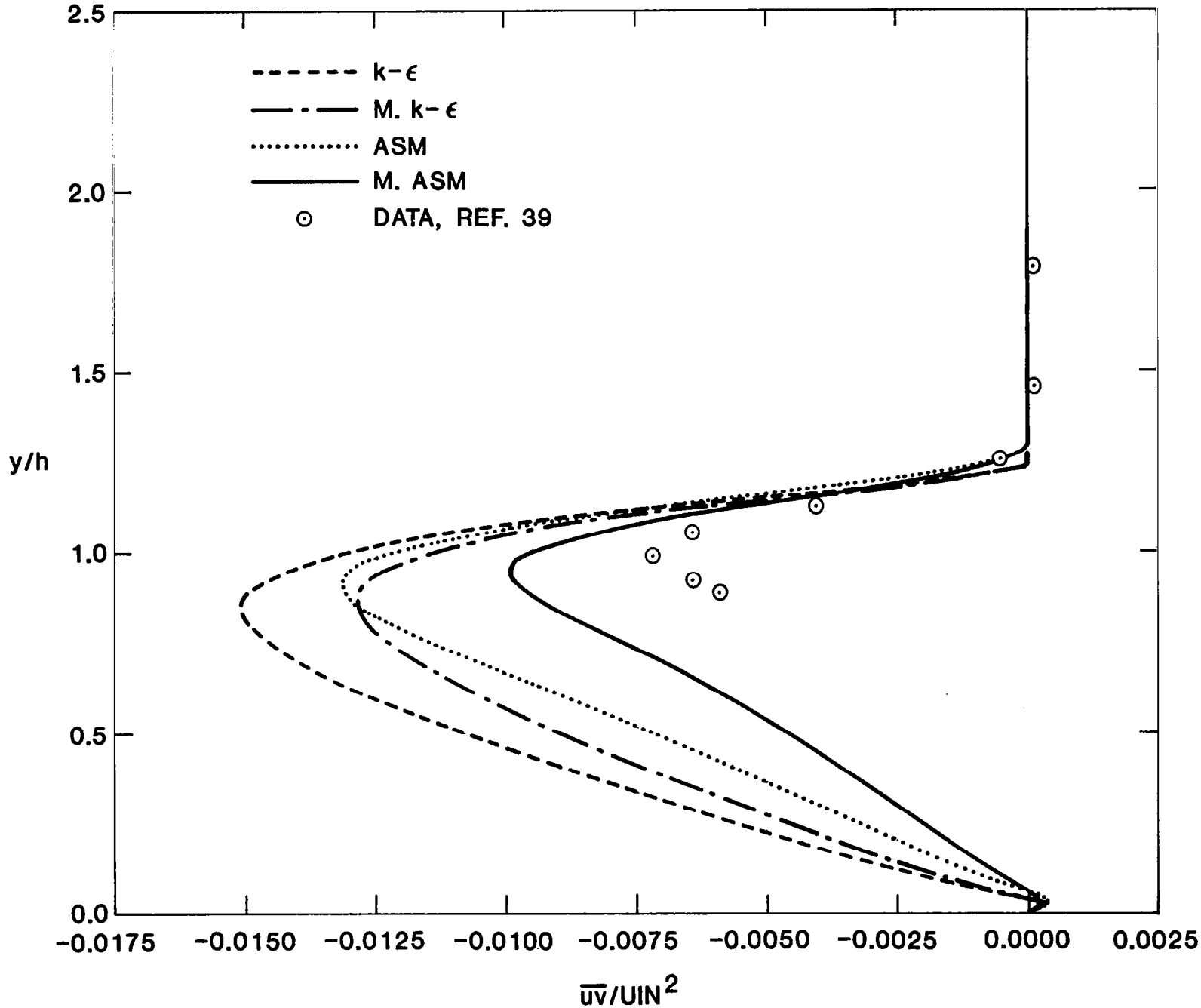

FIGURE 3.11a. $\overline{uv}$ Profiles at Streamwise Location x/h = 2.333. 3:1 Area Ratio Planar Expansion, UIN = 18.2 m/s. Data From Kim, Kline and Johnston, Ref. 39.

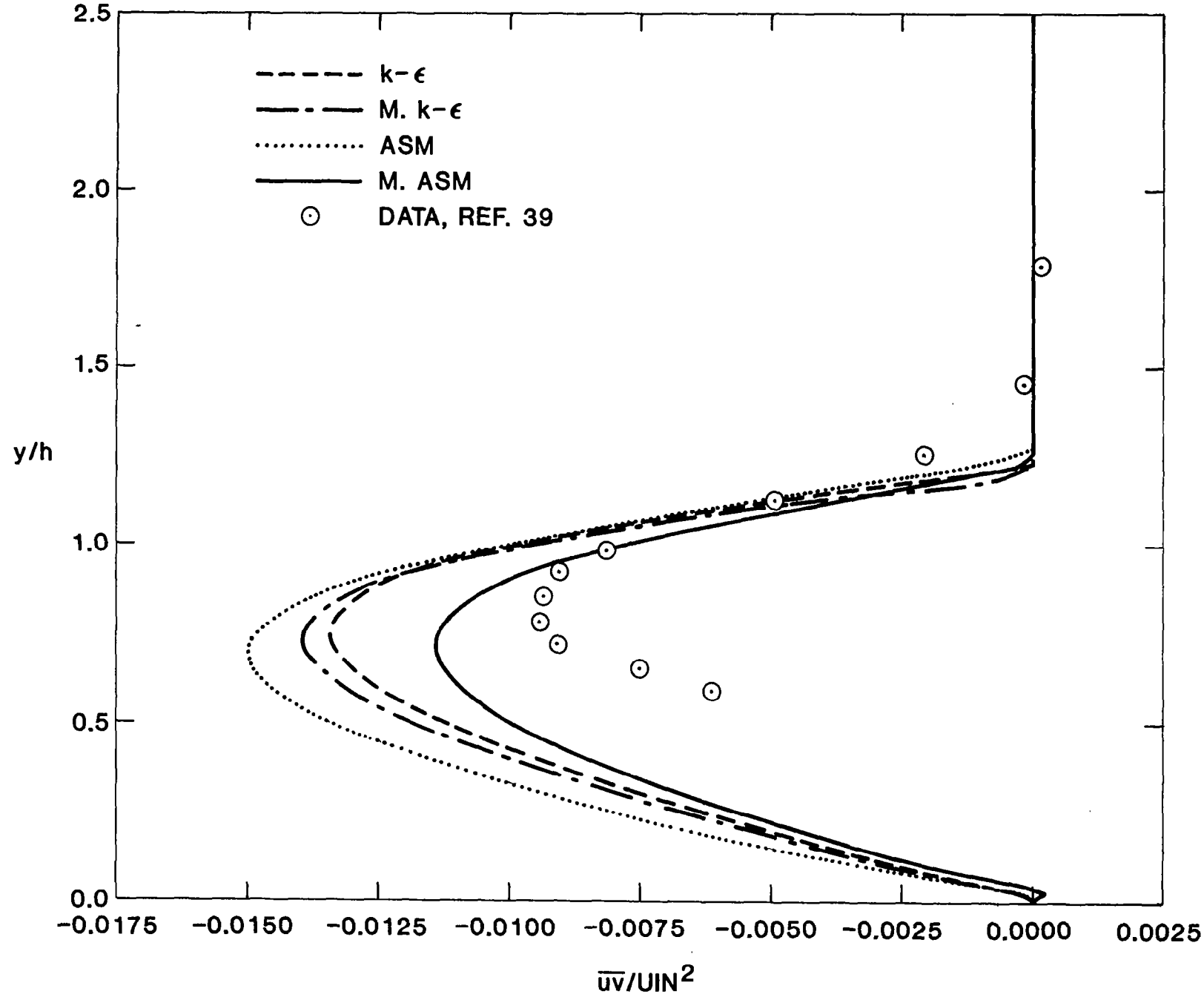

FIGURE 3.11b. $\overline{uv}$ Profiles at Streamwise Location x/h = 5.887.
3:1 Area Ratio Planar Expansion, UIN = 18.2 m/s.
Data From Kim, Kline and Johnston, Ref. 39.

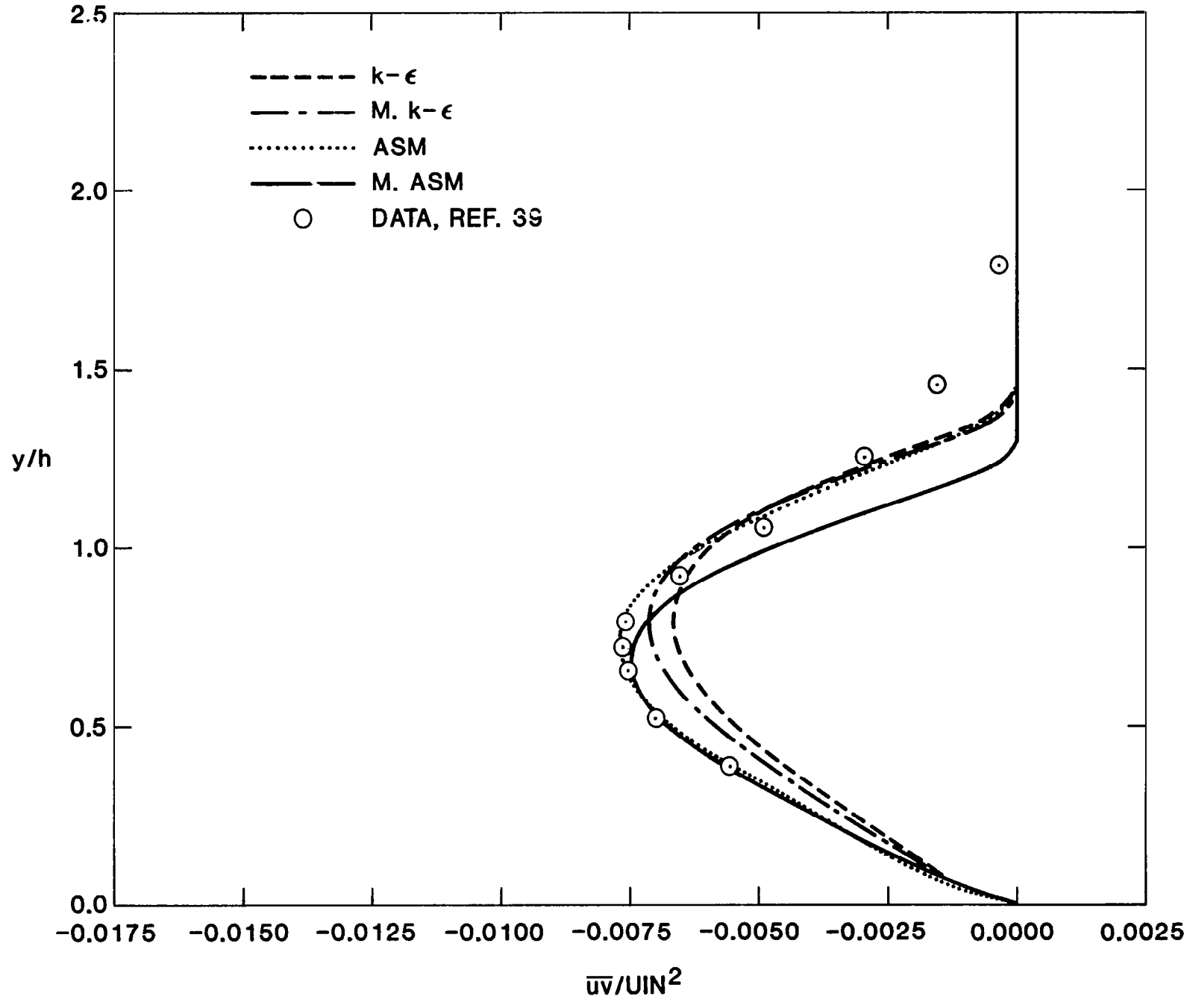

FIGURE 3.11c. $\overline{uv}$ Profiles at Streamwise Location x/h = 10.33.
3:1 Area Ratio Planar Expansion, UIN = 18.2 m/s.
Data From Kim, Kline and Johnston, Ref. 39.

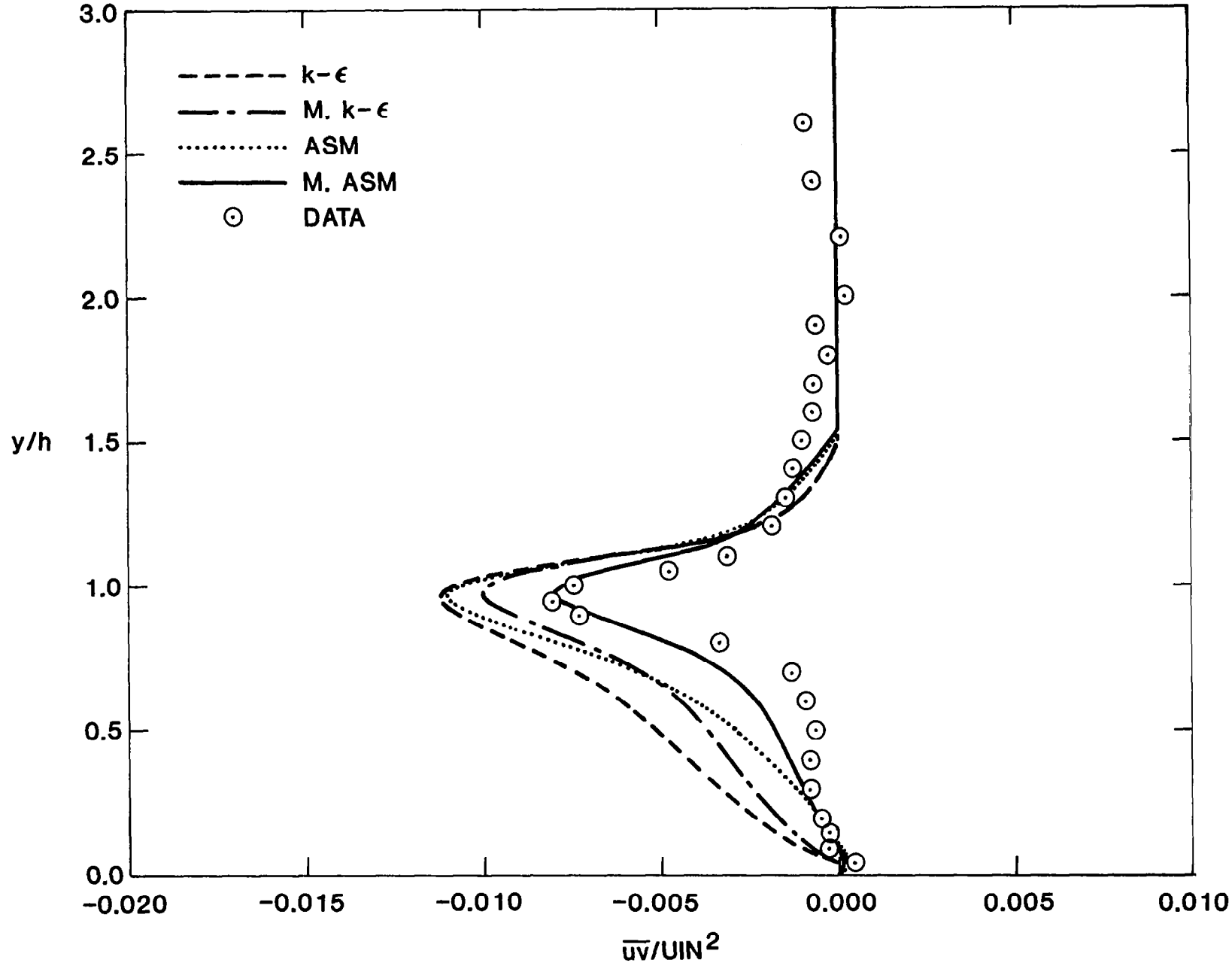

FIGURE 3.12a. $\overline{uv}$ Profiles at Streamwise Location x/h = 1.25.
4:1 Area Ratio Planar Expansion, UIN = 44.2 m/s.
Data From Driver and Seegmiller, Private Communication.

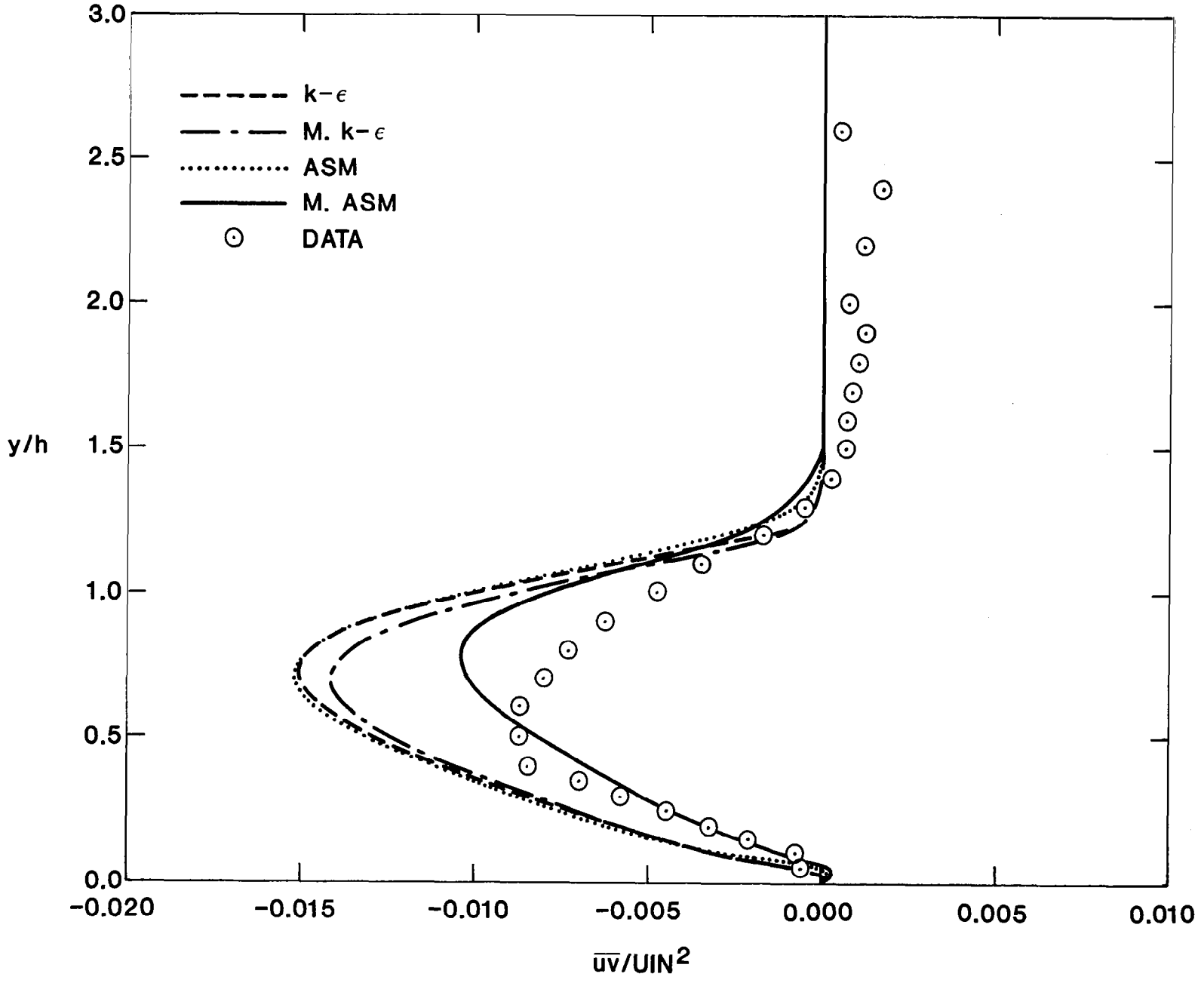

FIGURE 3.12b. $\overline{uv}$ Profiles at Streamwise Location x/h = 4.00.
4:1 Area Ratio Planar Expansion, UIN = 44.2 m/s.
Data From Driver and Seegmiller, Private Communication.

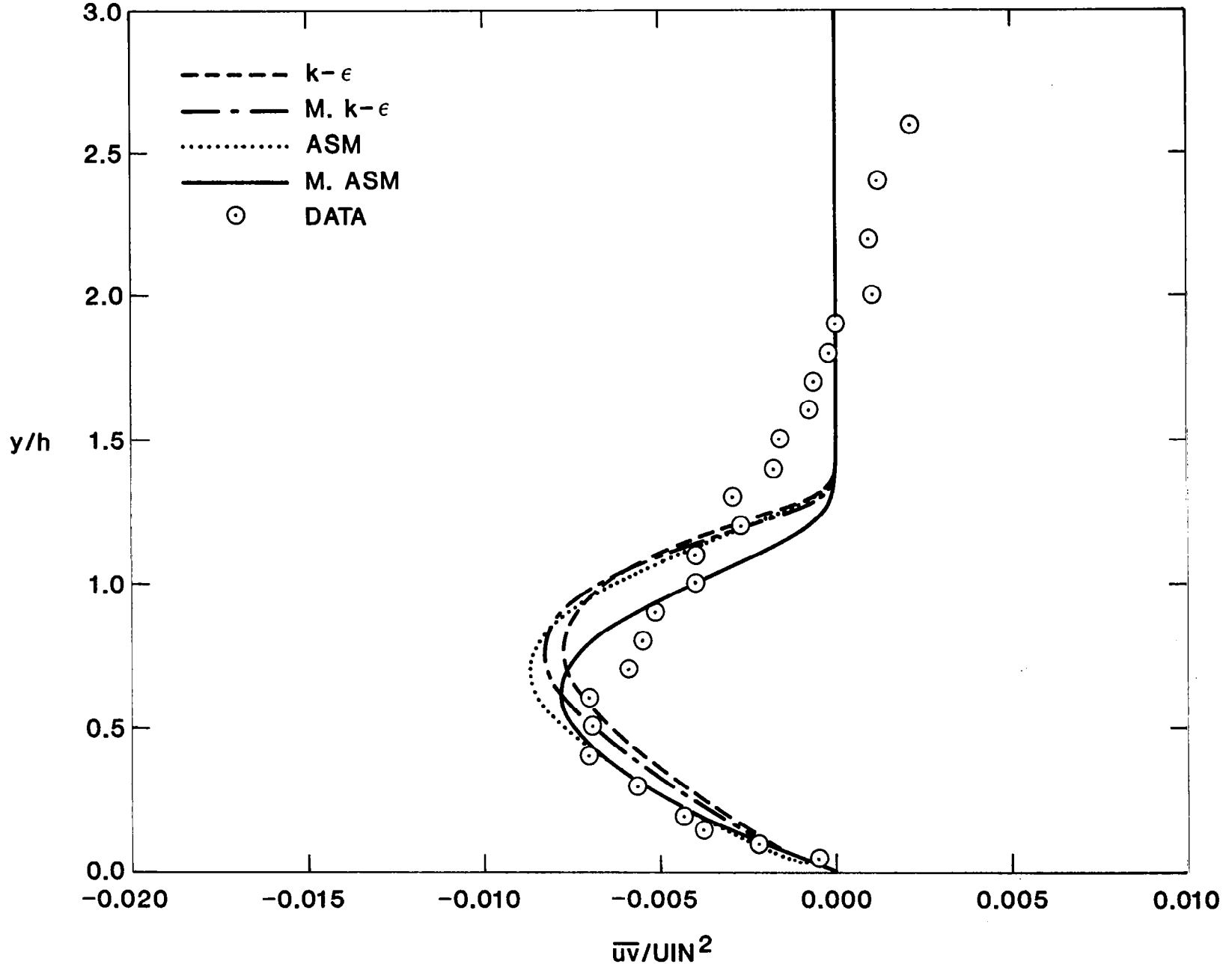

FIGURE 3.12c. $\overline{uv}$ Profiles at Streamwise Location x/h = 8.63.
4:1 Area Ratio Planar Expansion, UIN = 44.2 m/s.
Data From Driver and Seegmiller, Private Communication.

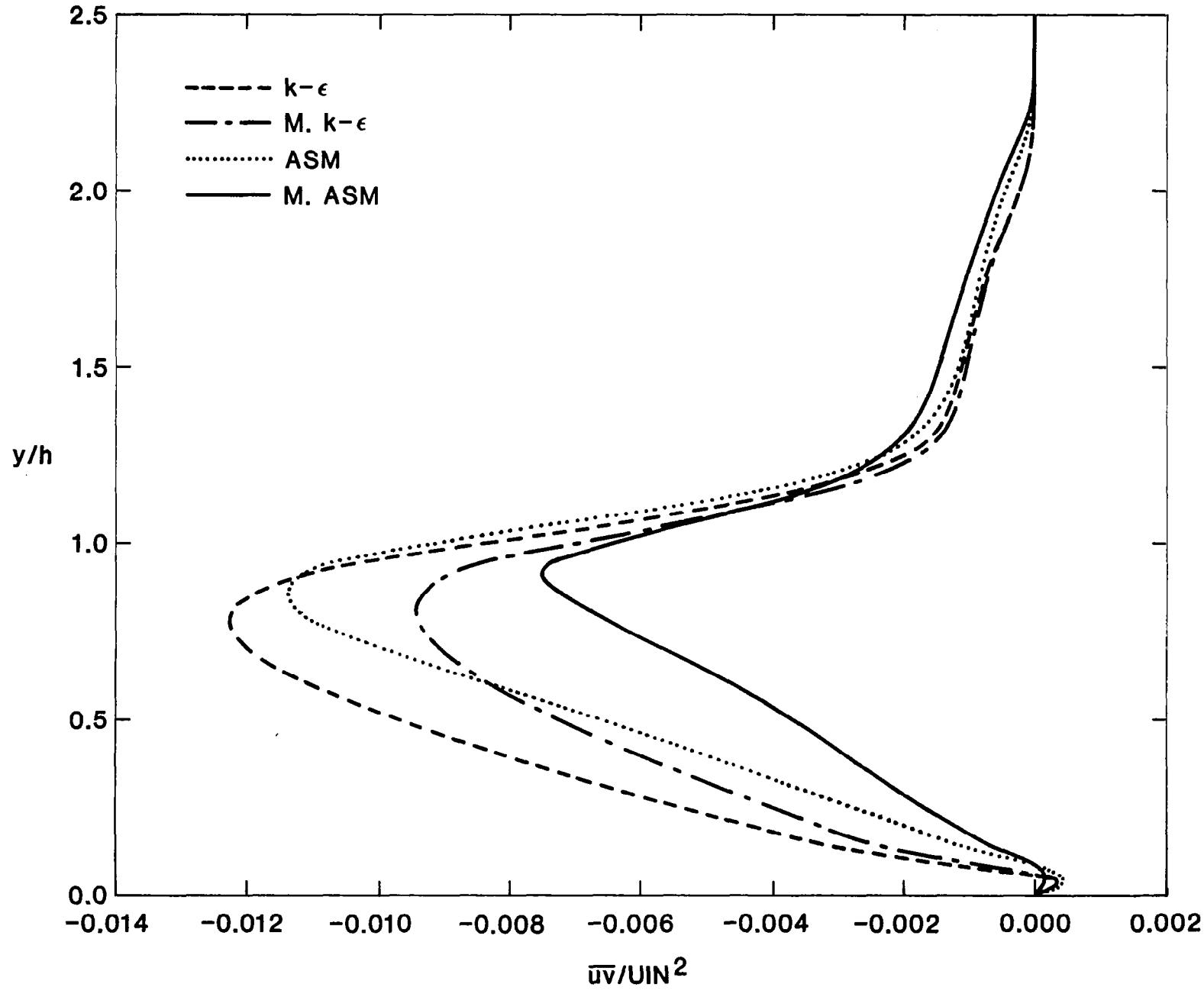

FIGURE 3.13a. $\overline{uv}$ Profiles at Streamwise Location x/h = 2.0.
9:1 Area Ratio Planar Expansion, UIN = 44.2 m/s.

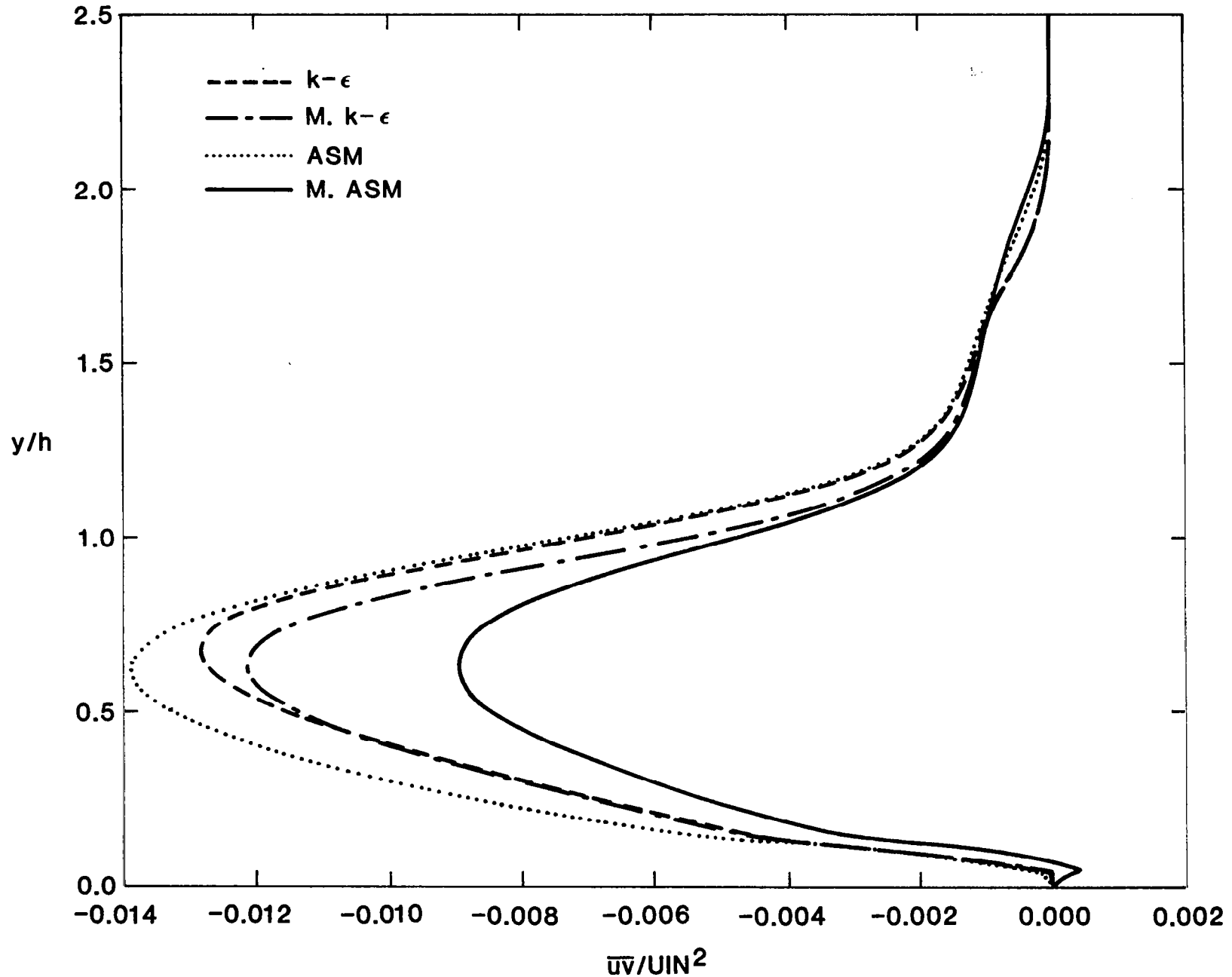

FIGURE 3.13b. $\overline{uv}$ Profiles at Streamwise Location x/h = 4.00.
9:1 Area Ratio Planar Expansion, UIN = 44.2 m/s.

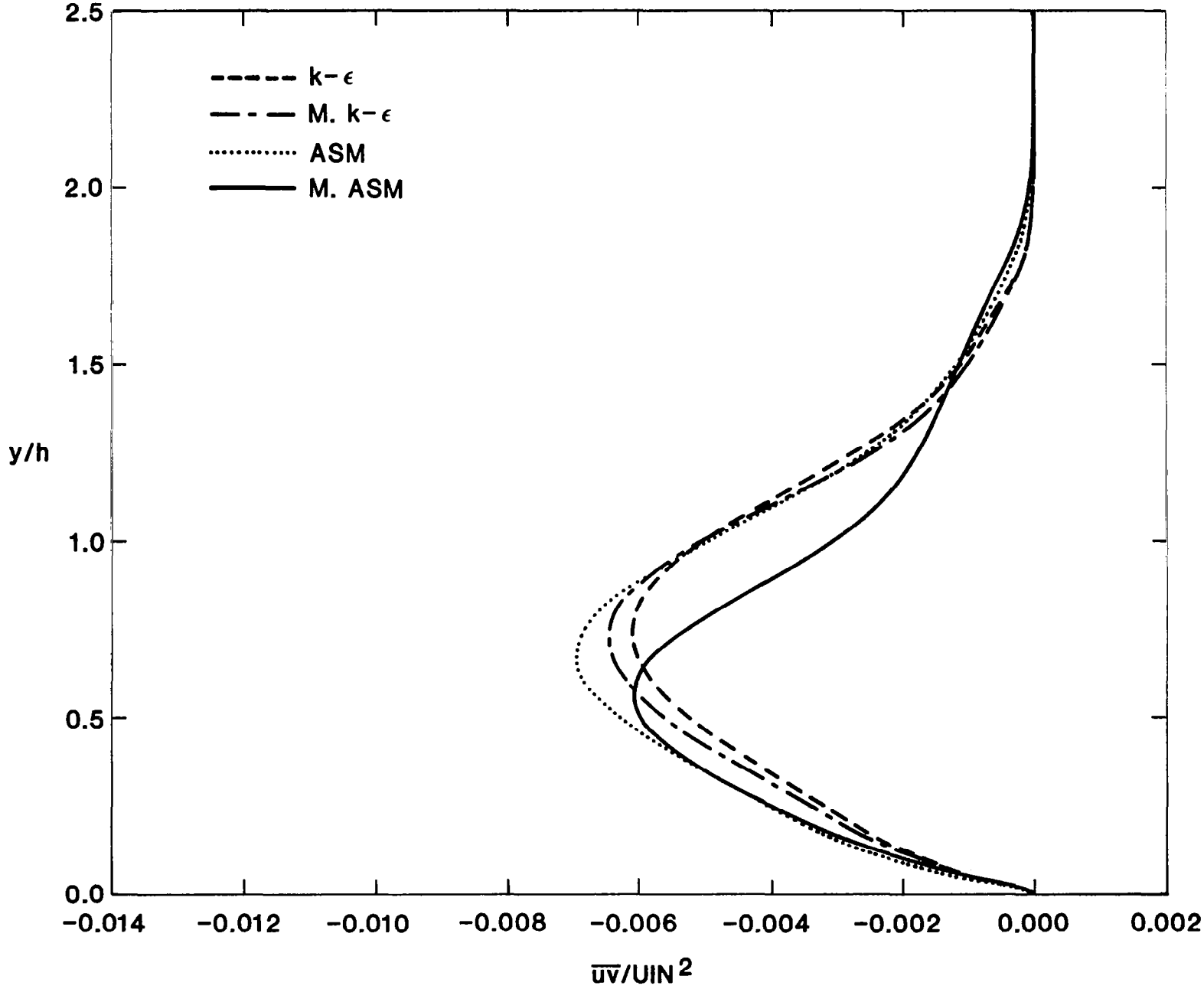

FIGURE 3.13c. $\overline{uv}$ Profiles at Streamwise Location x/h = 8.63.
9:1 Area Ratio Planar Expansion, UIN = 44.2 m/s.

peak around a y/h of 0.9. This is followed by a rapid drop to the free stream levels. Further downstream the $\overline{uv}$ values experience a more gradual variation with y, increasing monotonically (in magnitude) to a negative peak at a y/h of about 0.5 before descending to their freestream values. From there on the same qualitative behavior is observed with the profiles flattening out and the magnitude of the peaks decreasing with streamwise distance. In all regions higher expansion ratios favor a more gradual return to the freestream levels.

Agreement between predictions and measurements range from satisfactory to good with the "modified" ASM generally showing the best agreement followed by the ASM, "modified" k-ε and k-ε models. The differences between the predictions diminish downstream of the recirculation zone where all models predict a more rapid drop to the freestream levels than the data indicate. This is especially true for the "modified" ASM which reaches its peak at lower y/h values and then descends to the freestream levels considerably sooner than the other models. In all cases the net effect of the modification seems to be a reduction in the shear stress levels; maximum peak $\overline{uv}$ values drop by as much as 52 percent over the standard version for the ASM and about 12 percent for the k-ε model. This decrease also seems to depend on the expansion ratio, with lower expansion ratios showing slightly less sensitivity to the modifications in both models.

The behavior of $\overline{uv}$ described above brings up several important observations for discussion. Firstly, the excellent agreement displayed by the "modified" ASM in the recirculation zone is not surprising since this model was also highly successful in predicting the size of this region. Similarly, the relative performance of the other models correlate closely with their reattachment length predictions. The effect of the modification on the shear stress computations may be explained by studying the expressions used in the models to calculate $\overline{uv}$. The k-ε model employs the Boussinesq approximation (equation (24)) which has a transport coefficient μ_T defined as $c_\mu \rho k^2/\varepsilon$. Since one of the effects of the modification is to reduce the turbulent kinetic energy, it is reasonable to expect that this would also diminish μ_t and the shear stress. The ASM, on the other hand, uses a more complicated expression (equation (71)) that includes a transport coefficient, Γ (a function of k), and the anisotropic normal stress components, e_u and e_v, to calculate $\overline{uv}$. Again the modification is observed to

reduce all these quantities leading to lower shear stress levels. The effects of the expansion ratio on the $\overline{uv}$ values can also be explained by reference to the turbulent kinetic energy predictions. Since higher expansion ratios tend to diminish the levels of k for all models, it is plausible that the $\overline{uv}$ values which have a strong functional dependence on k would behave similarly.

C. Conclusions

All of the models considered successfully predict the qualitative behavior of the mean flow and turbulence parameters in all test cases. The relative performance of the models however is region-dependent, and hence the best predictions are not necessarily obtained by the same model in both the reverse flow and recovery zones. The established trends within a given region do not vary with expansion ratio or deflection angle. The main effect of these factors is to change the size of the recirculation zone and the levels of the turbulent kinetic energy and shear stresses. Higher expansion ratios reduce both the size of this region and the levels of these quantities. Finally, the modification introduced to the models increases the predicted reattachment lengths and reduces the turbulent kinetic energy and stress levels in all test cases. In the recirculation zone all models tend to underpredict the size of this region in varying degrees. Generally, the "modified" ASM computes reattachment lengths that compare very favorably with measurements. Predictions by the remaining models are usually considerably shorter than the data. Here, the mean velocity as well as the turbulence parameters correlate closely with the reattachment length. Therefore the best agreement with the measured U- and V-velocities is achieved by the "modified" ASM-followed, in order, by the ASM, "modified" k-ε, and k-ε models. The scarcity of reliable turbulence measurements in this region makes valid quantitative comparisons a difficult task. Within the scope of available data, the agreement between the $\overline{uv}$ predictions and measurements is generally quite good; the "modified" ASM shows the best success-followed, in the above order, by the other three models.

In the recovery region all four models predict too slow a recovery rate. Computations by the ASM, "modified" k-ε, and k-ε models are hardly distinguishable from each other. The "modified" ASM displays an even slower recovery when

plotted against the actual distance from the step. When this distance is normalized relative to the reattachment point the differences in the predicted recovery rates diminish. The agreement between the $\overline{uv}$ predictions and measurements is generally satisfactory for all models.

The following conclusions can be drawn from the assessment of the models for plane backward-facing step flows:

(1) The relative performance of the models in subsonic backward-facing step flow computations is region-dependent, i.e., best predictions are not necessarily obtained by the same model in both the reverse flow and recovery regimes.

(2) The "modified" ASM produces the best predictions in the reverse flow region but computes too slow a recovery rate in the relaxation regime where the other models show better agreement with the data.

(3) A modular approach that uses the "modified" ASM in the reverse flow region and the standard version in the recovery regime appears to be the most appropriate scheme for predicting subsonic plane backward-facing step flows.

3.2.2 Axisymmetric Flows

Before the axisymmetric flow predictions are discussed, it is informative to review the past and present efforts in this area. Earlier work which used a stream function-vorticity (ψ - Ω) formulation identified three problem areas in axisymmetric flow predictions. These were:

(1) Treatment of the corner point at the expansion plane

(2) Treatment of the first-derivative term in the ψ-equation

(3) Treatment of the wall boundary conditions near reattachment

The corner-point treatment problem involves the proper establishment of the boundary conditions at the dump plane, i.e., at the intersection of the inlet wall and step. At this point, the dividing streamline that separates the recirculation zone downstream of the step from the remainder of the flow has its origin. For the proper prediction of recirculation zone length it is essential that at this point the dividing streamline have a zero slope, i.e., that it be

parallel to the inlet wall contour. Within a stream function-vorticity formulation, this condition can be directly specified; for primitive-variable formulations it is specifiable only indirectly, through specification of the gradients in the axial and radial velocity components. The second problem involved the treatment of the term $\frac{1}{r}\frac{\partial\psi}{\partial r}$ that appears in the axisymmetric form of the stream function equation. As a first derivative term it could not be treated numerically in the same fashion as the second-derivative terms which describe the remainder of the diffusion of stream function: i.e., in the numerical solution of the stream function transport equation

$$\frac{\partial^2\psi}{\partial x^2} + \frac{\partial^2\psi}{\partial r^2} + \frac{1}{r}\frac{\partial\psi}{\partial r} = -r\Omega$$

approximation of the second derivative terms using second-order differences and the first derivative term using first-order upwind differencing introduces "wiggles" into the solution near the centerline. The problem was overcome by noting that $\frac{1}{r}\frac{\partial\psi}{\partial r} = u$ (for an incompressible flow) and treating the term in question as a "source" term. While this slowed the overall convergence of the iterative solution procedure (since the value of the axial mean velocity u is obtained for the computation at the last step) this change removed the inaccuracies that resulted from the mixed differencing orders.

Treatment of the wall boundary condition involves both numerical solution technique aspects and turbulence modeling aspects, since within a given overall flowfield solution technique it is generally not possible to use a sufficiently fine grid to provide the resolution necessary to avoid approximations near walls. The standard approach to wall boundary condition formulation is to use the law-of-the-wall to define an effective axial velocity at the first grid point away from the wall. In general, the logarithmic law of the wall provides a valid approximation, but it breaks down near the reattachment point where the axial velocity tends toward zero and the logarithmic portion of the boundary layer disappears. The solution is to include a treatment, again based on empirical formulations, for the laminar sublayer region, and to treat the match point between the flowfield solution and the wall boundary as a variable rather than a prescribed location. This requires an iteration to be carried out to establish

both the friction velocity and the match point, but results in a considerable improvement in the prediction of recirculation zone length.

The effects of the treatment chosen for each of these three problem areas in the context of a stream function-vorticity formulation is shown in Figure 3.14. In all cases the basic two-equation turbulence model, as described in Section 2, was used in the flowfield calculation. The flowfield represented is an incompressible sudden expansion with two coaxial inlet streams, the inner of which is at a velocity level of 1/3 of the outer stream. These data were reported by Habib and Whitelaw (Ref. 41). Substantial differences in the predicted centerline velocity results are observed for each of the changes discussed in the preceding paragraphs and outlined in Figure 3.14. In each case, the same turbulence model has been used, illustrating the effects on the overall results of the specification of the numerical aspects of the problem. Since different numerical solution procedures involve different boundary condition and initial condition treatments, the variation illustrated here can be taken to indicate the discrepancies that may be encountered when the turbulence models developed using a given solution procedure are applied to analyses which use different procedures.

Much of the computational work described in this section uses a significantly different numerical formulation than the ψ-Ω code considered in the previous paragraphs. This code, which is based on the STEP family, is discussed in detail in Ref. 5. It solves two-dimensional (planar or axisymmetric) steady-state and time-dependent elliptic partial differential equations through an iterative procedure based on an integral control volume analysis with hybrid upwind finite differencing[†] and staggered grids[††]. The flow and turbulence

[†]In evaluating the values of the dependent variables at the cell boundaries one of two practices is usually adopted. If it is assumed that the variable in question varies linearly between the two nodes bracketing the cell boundary, the value of the variable at that boundary is taken as the arithmetical average of the nodal values. This procedure is usually referred to as "central differencing". The second practice known as "upwind differencing" assumes that the value at the cell boundary is equal to that of the upwind node. However, a "hybrid" scheme that employs one or the other of these procedures depending on the value of the cell Reynolds number may actually be superior to either of these schemes used alone. A version of this hybrid upwind finite differencing scheme first proposed by Spalding (Ref. 42) is employed in the STEP family.

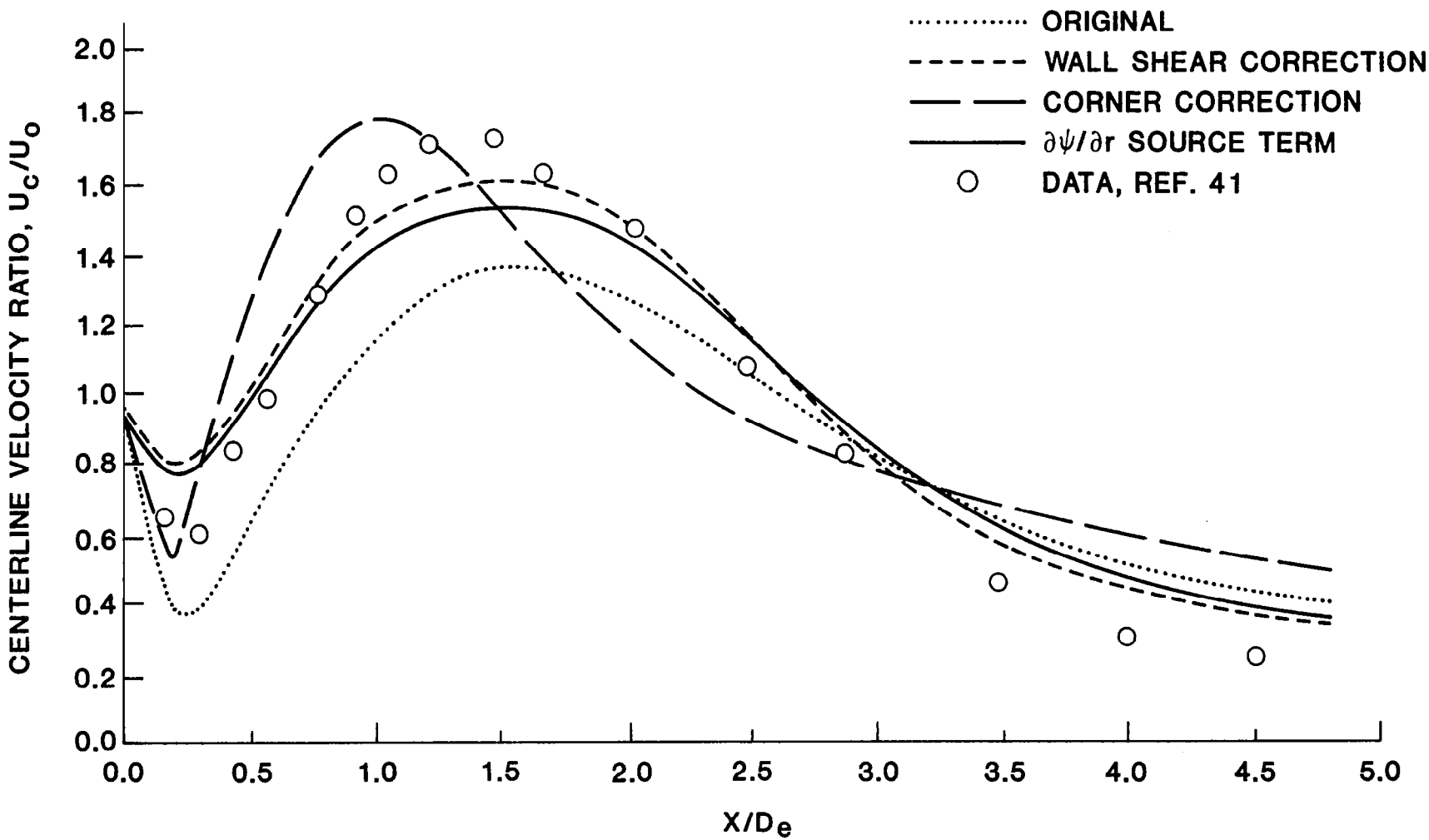

FIGURE 3.14. Effects of Code Refinement on Centerline Velocity Profile Prediction. Stream Function-Vorticity Code, Two-Equation k-ε Turbulence Model. Data From Habib and Whitelaw, Ref. 41.

equations are solved in primitive variables (U, V, P, k, ε, etc.). Within the STEP methodology the treatment of corner cells is straightforward. Figure 3.16 outlines the treatment used for typical scalar variable, and U- and V-velocity corner cells at the expansion plane of a backward-facing step geometry. Again, since it is not feasible in the STEP code to provide sufficient near-wall grid resolution to avoid approximations, the treatment of wall boundaries near reattachment remains a problem in turbulence modeling. In fact, the new non-equilibrium wall-functions discussed in Section 2.9 were developed to address this particular problem. The basic difference between the two approaches is that the STEP family uses the viscous sublayer/fully turbulent region interface kinetic energy instead of the friction velocity, while in the stream function-vorticity approach the thickness of the viscous sublayer is treated as a variable in matching the velocity profiles at the interface between the viscous sublayer and the turbulent interior flow.

Using the STEP code, predictions of the axisymmetric incompressible 2:1 diameter ratio sudden expansion flowfield described by Chaturvedi (43) were obtained with the k-ε, "modified" k-ε, ASM, and "modified" ASM models. A non-uniform 22 by 22 node mesh was used. This mesh is relatively coarse, so that the results may not be grid-independent. However, the comparative computations are believed to be representative of the capabilities of the different models. To provide a broader overall comparison, the results of the predictions carried out using the STEP code and the different turbulence models have been compared to stream function-vorticity code predictions using the k-ε model, and to data obtained by Schmotolocha and Phung (Ref. 44) for the same geometry but at a substantially higher inlet Reynolds number (1.4×10^6 compared to 2×10^5).

---

††For hybrid differencing purposes the STEP family uses a staggered grid in which the velocities are evaluated at the boundaries of scalar variable (P, k, ε, etc.) cells. Hence, separate grids define the locations of the U- and V-velocities. A portion of these three grids is shown in Figure 3.15.

The solution domain is arranged so that the outer surfaces of the boundary scalar cells coincide with the physical boundaries of the flow field. The advantages of this scheme become apparent when the boundary conditions are incorporated into the finite difference formulation. Figure 3.16 shows the solution domain used for a typical backward-facing step geometry.

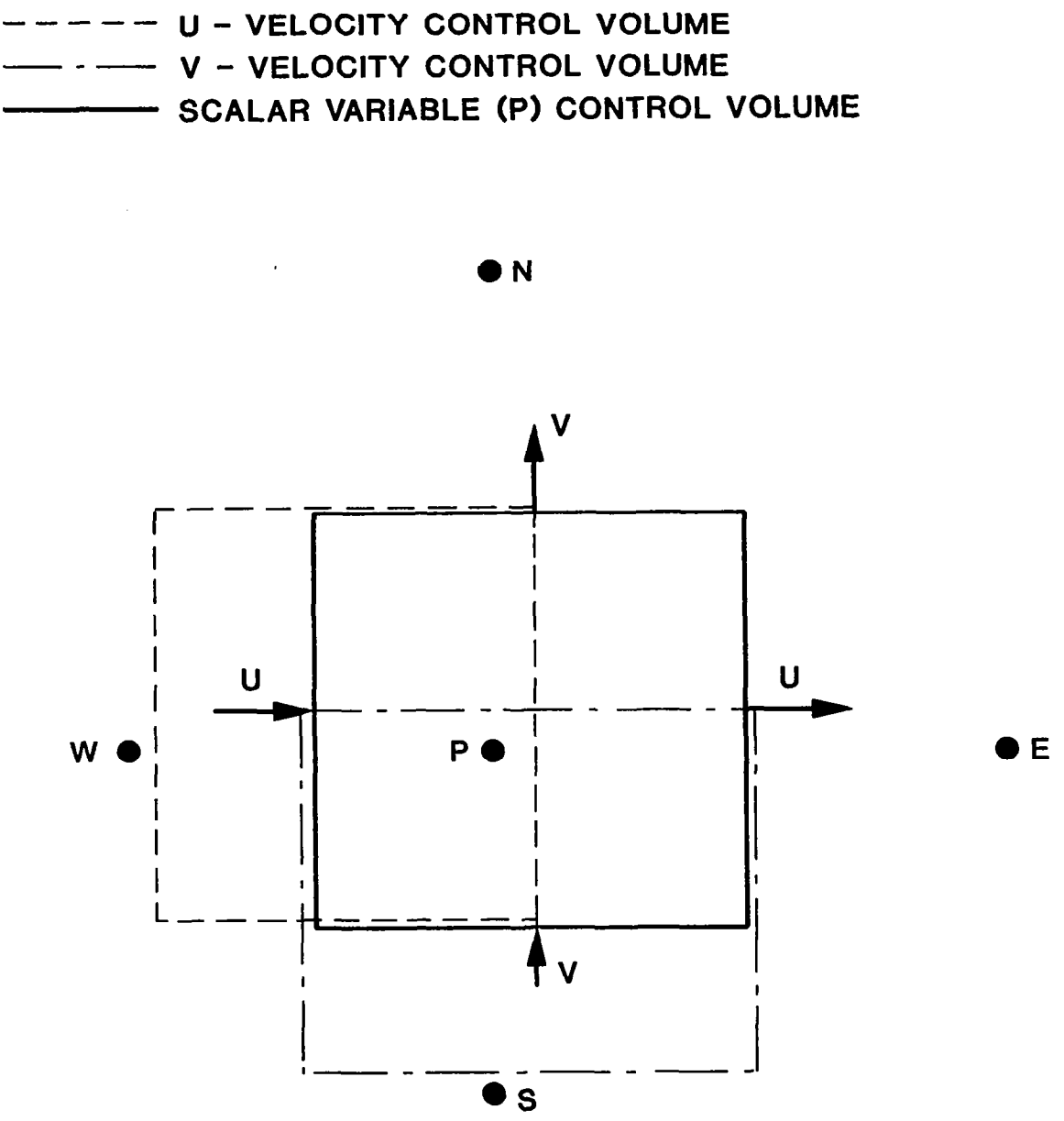

FIGURE 3.15. Typical Non-Uniform STEP Grid Portion.

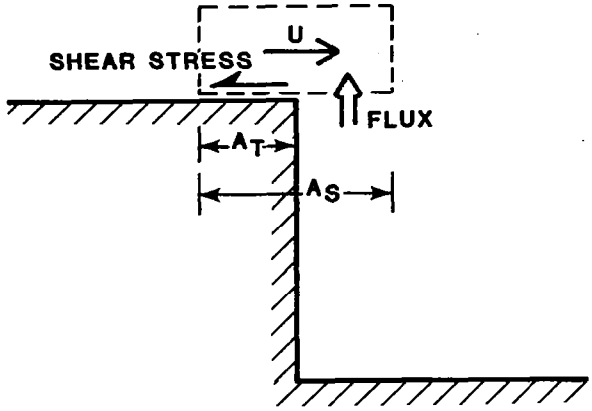

a) U-Velocity Corner Cell

Special Treatment for U-Velocity Corner Cell:

1. Wall shear stress applied only through area A_T.
2. Flux leaves or enters cell from the south boundary through area $A_S - A_T$.
3. Remaining fluxes calculated in the usual way outlined in Ref. 5.

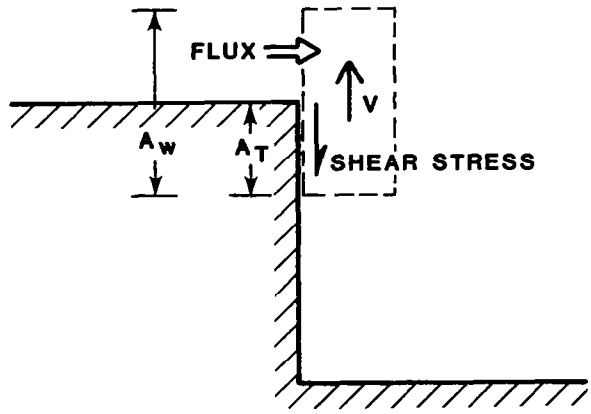

b) V-Velocity Corner Cell

Special Treatment for V-Velocity Corner Cell:

1. Wall shear stress applied only through area A_T.
2. Flux leaves or enters cell from the west boundary through area $A_W - A_T$.
3. Remaining fluxes calculated in the usual way outlined in Ref. 5.

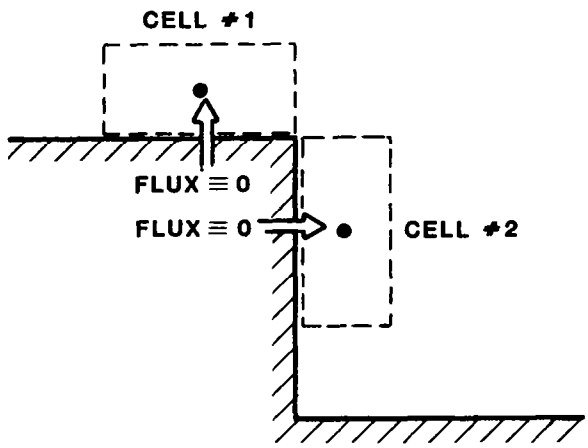

c) Scalar Variable Corner Cell

Special Treatment for Scalar Variable Corner Cell:

1. For cell #1, flux in the southerly direction set to zero.
2. For cell #2, flux in the westerly direction set to zero.
3. Remaining fluxes calculated in the usual way outlined in Ref. 5.

FIGURE 3.16. Corner Cell Treatment in the STEP Family.

Reattachment length results are given in Table 3.4. Excluding the "modified" ASM which overpredicts the reattachment length by some 40%, the agreement between the k-ε, "modified" k-ε, and ASM computations, and the Chaturvedi measurements is remarkably good. The k-ε model predictions obtained using the ψ-Ω code also show excellent agreement with the data and the STEP code computations. The apparent failure of the "modified" ASM is at present difficult to interpret. Possible causes are that: the modification to the model may perform poorly in axisymmetric flows, or for low expansion ratios†, or maybe for both. A series of carefully selected test runs to be carried out during continuing work should identify the source of the problem. The differences between the remaining three models are small. This was anticipated because in low expansion ratio axisymmetric geometries, the flow is dominated by the pressure field, and the influence of the turbulence models is correspondingly less important.

TABLE 3.4. Reattachment Length Predictions for the Chaturvedi (Ref. 43) Study (2:1 Diameter Ratio)

Models (STEP Code)	Reattachment Length in Step Heights
k-ε	7.91
"modified" k-ε	8.07
ASM	8.08
"modified" ASM	11.35
Chaturvedi Data (Ref. 43)	≃ 8.00
Schmotolocha & Phung Data (Ref. 44)	≃ 9.00
Stream function-vorticity code predictions (k-ε model)	8.00

Inlet Condition (both computational techniques)

Reynolds number (based on step height): 2×10^5

Inlet free-stream velocity (U_{in}): 31 m/s (see Figure 3.17a)

Turbulence intensity: $1 \times 10^{-5} U_{in}^2$ (assumed uniform)

†The lowest expansion ratio tested in planar flows was 3:1.

Figure 3.17 presents the predicted and measured U-velocity profiles at selected streamwise locations. The k-ε, "modified" k-ε, and ASM models show about equal success in predicting the velocity field. The agreement with data is generally satisfactory even though all three models tend to underpredict the velocities both in the recirculation zone and across the separated shear layer. The ASM displays slightly better agreement near the flow centerline, while the stream function-vorticity results seem to agree better data in the separated shear layer. The "modified" ASM velocity predictions cannot be compared with the measurements unless they are properly scaled relative to the predicted reattachment length. This can be accomplished by defining a new streamwise distance as $(x_R - x)/h$ and plotting the predicted velocity profiles in the recirculation region relative to this distance. x_R is the computed reattachment length and h is the step height. The centerline velocity calculations given in Figure 3.18 follow the trends established above. The invariance with Reynolds number of geometrically similar axisymmetric flows is confirmed by the excellent agreement throughout the channel between the radial profiles of velocity measured by Chaturvedi (Ref. 43) and by Schmotolocha and Phung (Ref. 44)† - except that probe interference effects are evident in the Ref. 44 data near the centerline.

Profiles of turbulent kinetic energy are compared with Chaturvedi's experimental data in Figure 3.19. For these comparisons, the assumptions $\overline{w^2} = \overline{v^2}$ has been made in the experimental data reduction: Chaturvedi presents profiles of $\overline{u^2}$ and $\overline{v^2}$ only. At $x/R_1 = 1.0$, both the shape and magnitude of the turbulent kinetic energy profiles are predicted extremely well using the stream function-vorticity code. The four models tested using the STEP code all successfully simulate the shape of the profiles, but they either overpredict the magnitude in the case of k-ε, "modified" k-ε, and ASM models or fall short of the data for the "modified" ASM. Further downstream ($x/R_1 = 2.0$ and 3.0), while the magnitude of the peak turbulence energy is predicted quite well using the ψ-Ω formulation and reasonably well by the k-ε, "modified" k-ε and "modified" ASM models using the STEP code (the standard ASM still overpredicts the data, progressively greater disagreement between the predicted level of turbulence energy and that measured

†Abbott and Kline (Ref. 37) reached the same conclusion for plane backward-facing step flows. However, these conclusions only apply to flows that are fully turbulent throughout the channel or pipe.

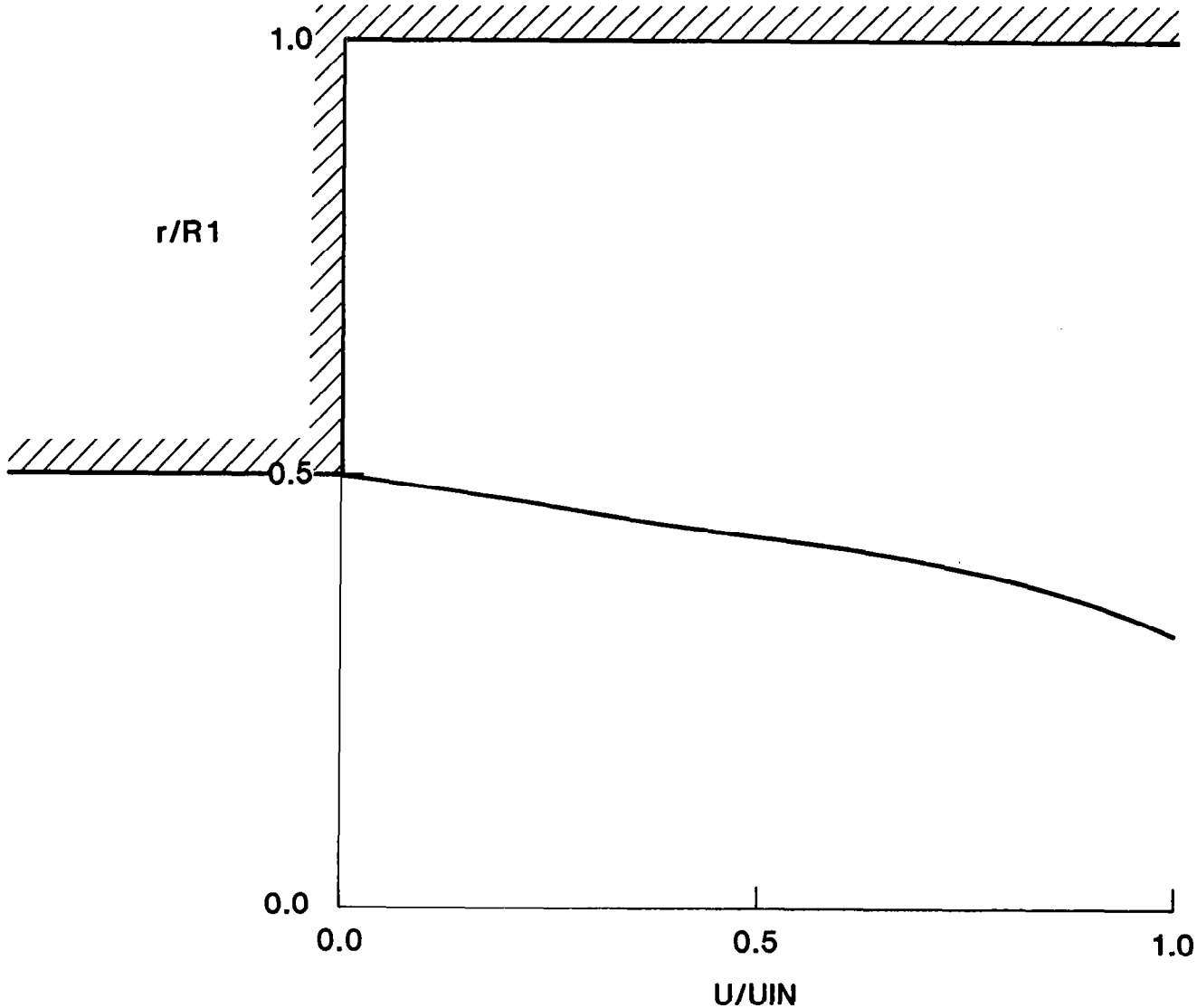

FIGURE 3.17a. Assumed Inlet Velocity Profile at x/R_1 = -1.08.
2:1 Area Ratio Axisymmetric Expansion, UIN = 31.0 m/s.

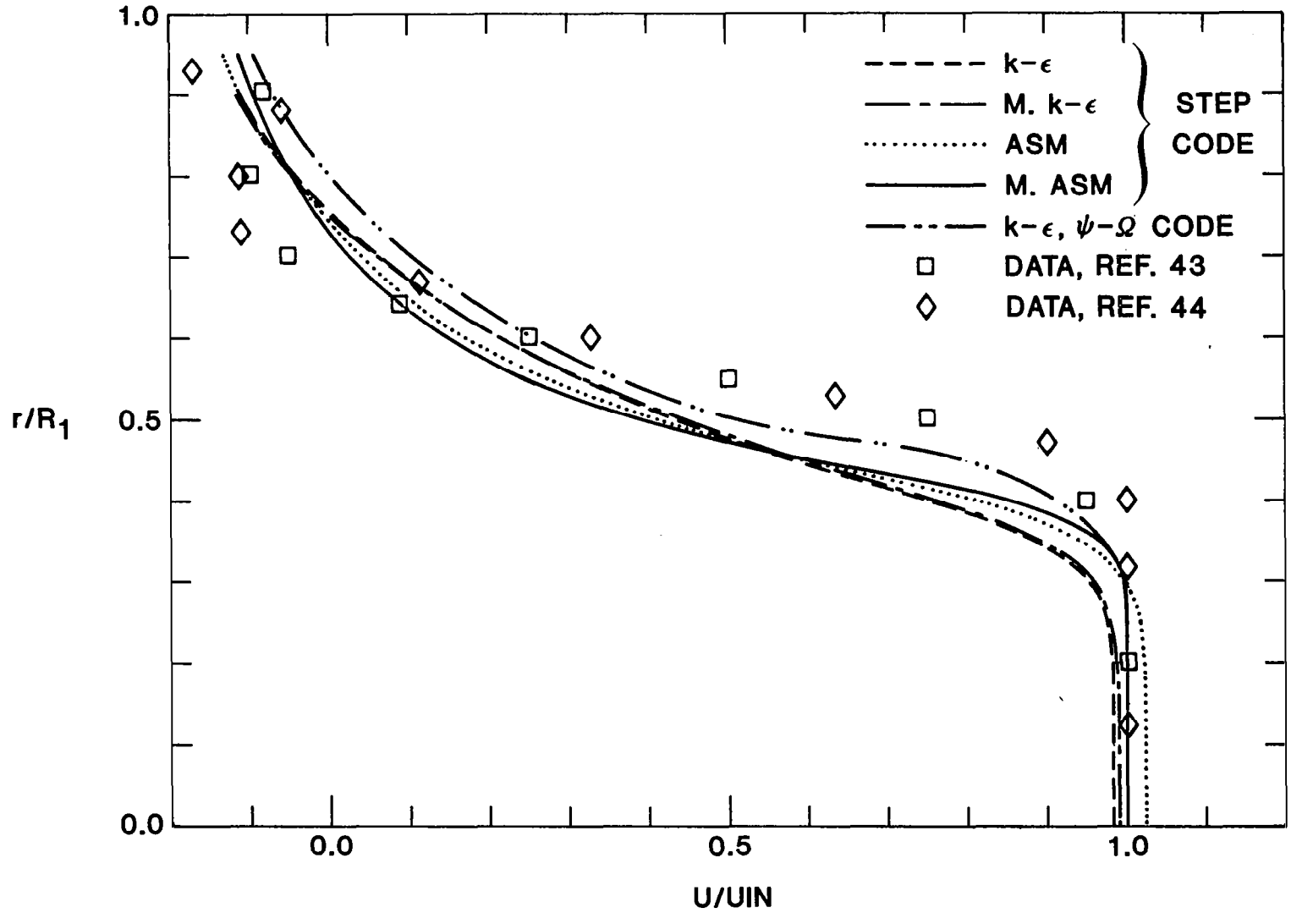

FIGURE 3.17b. U-Velocity Profiles at x/R_1 = 1.00. 2:1 Area Ratio Axisymmetric Expansion, UIN = 31.0 m/s. Data From Chaturvedi, Ref. 43, and Schmotolocha & Phung, Ref. 44.

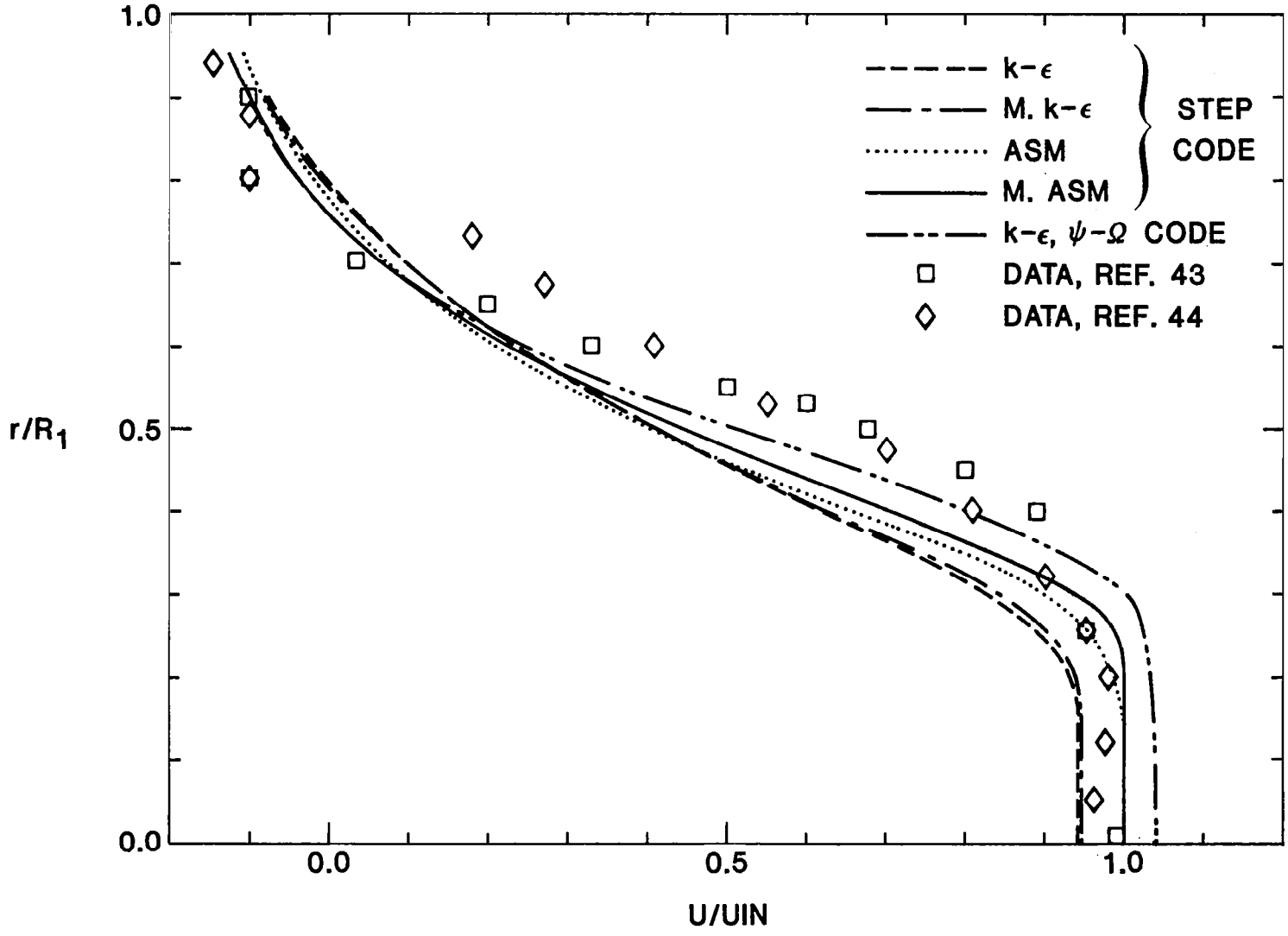

FIGURE 3.17c. U-Velocity Profiles at x/R_1 = 2.00. 2:1 Area Ratio Axisymmetric Expansion, UIN = 31.0 m/s. Data From Chaturvedi, Ref. 43, and Schmotolocha & Phung, Ref. 44.

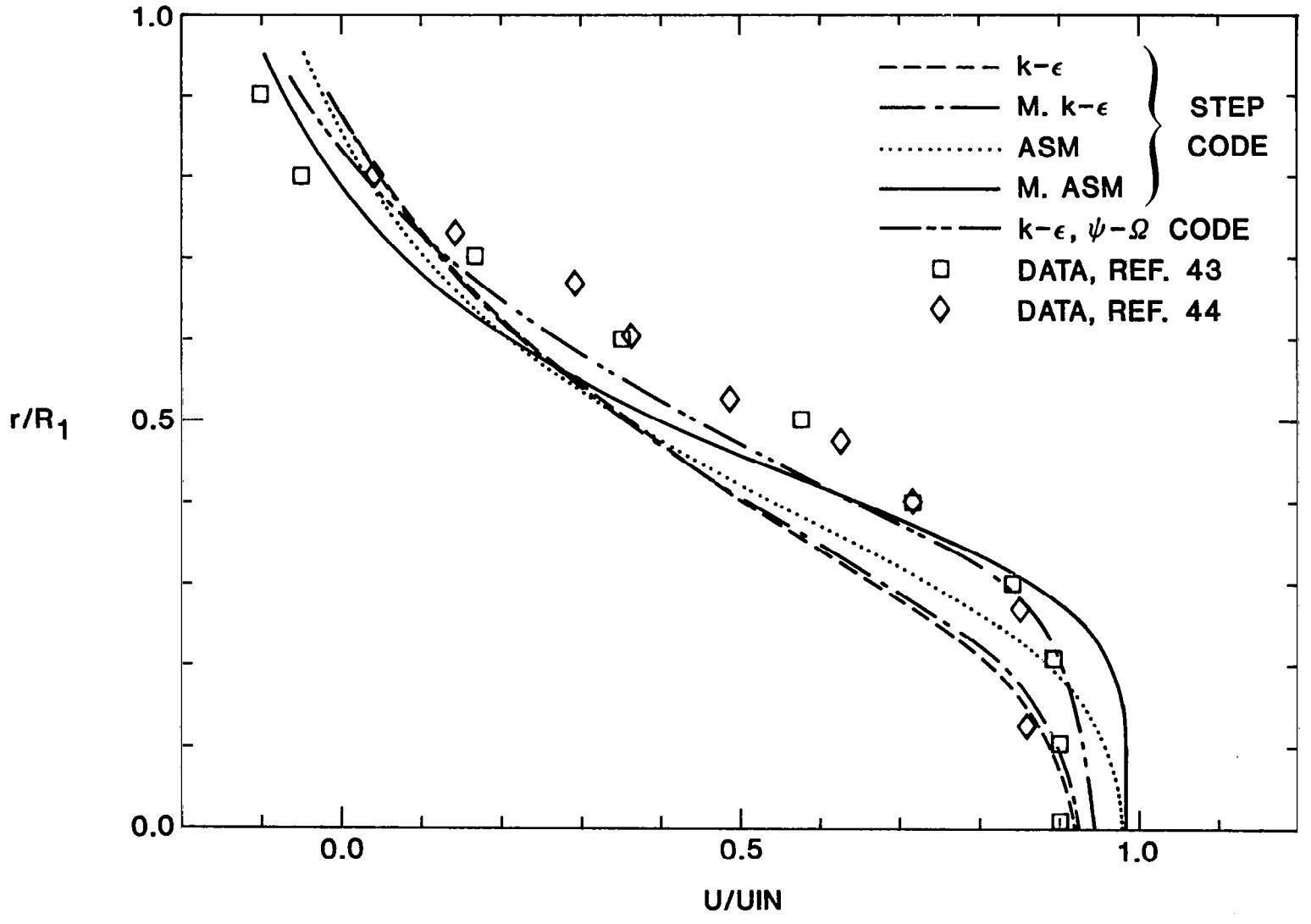

FIGURE 3.17d. U-Velocity Profiles at x/R_1 = 3.00. 2:1 Area Ratio Axisymmetric Expansion, UIN = 31.0 m/s. Data From Chaturvedi, Ref. 43, and Schmotolocha & Phung, Ref. 44.

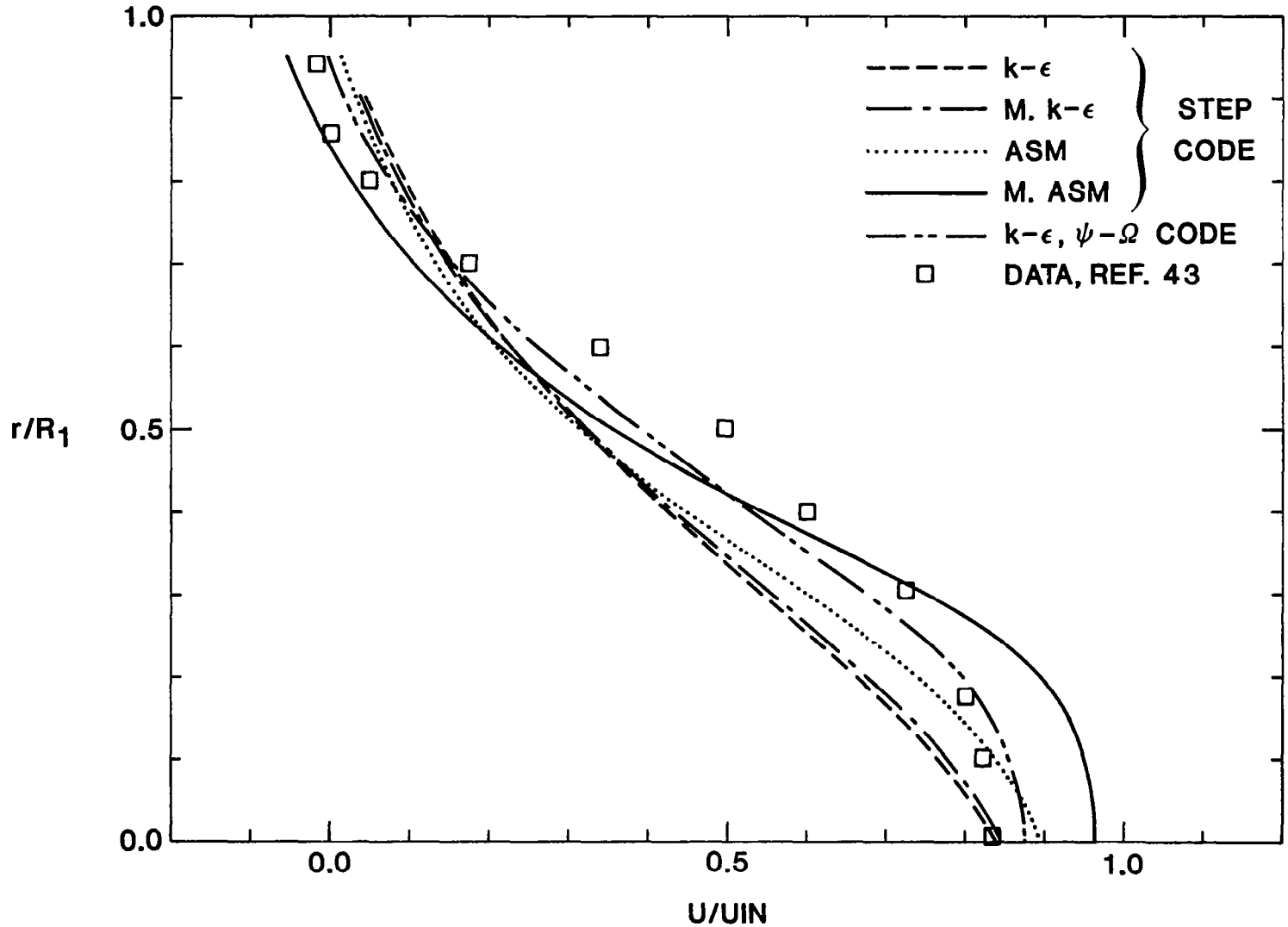

FIGURE 3.17e. U-Velocity Profiles at x/R_1 = 4.00. 2:1 Area Ratio Axisymmetric Expansion, UIN = 31.0 m/s. Data From Chaturvedi, Ref. 43.

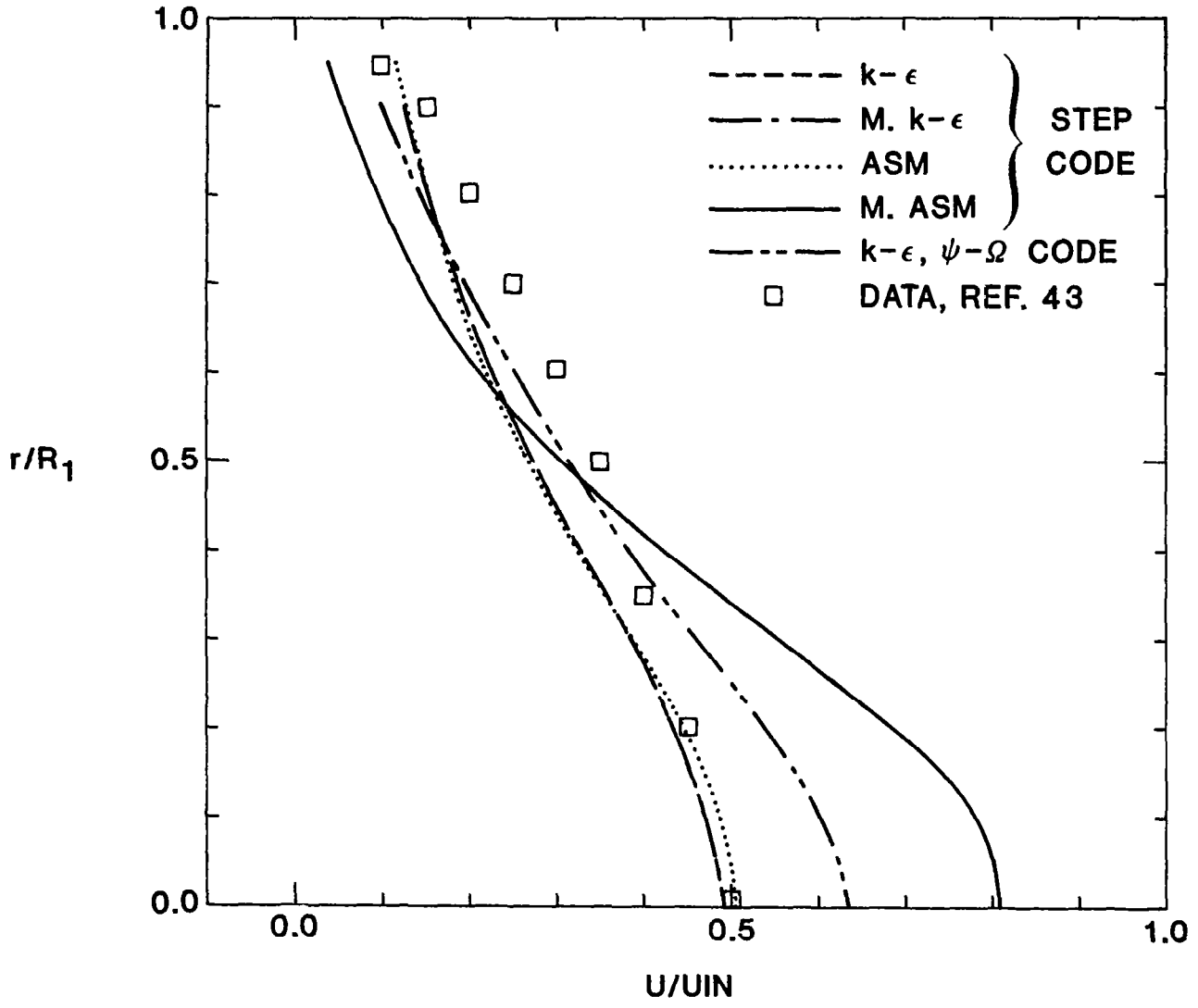

FIGURE 3.17f. U-Velocity Profiles at x/R_1 = 6.00. 2:1 Area Ratio Axisymmetric Expansion, UIN = 31.0 m/s. Data From Chaturvedi, Ref. 43.

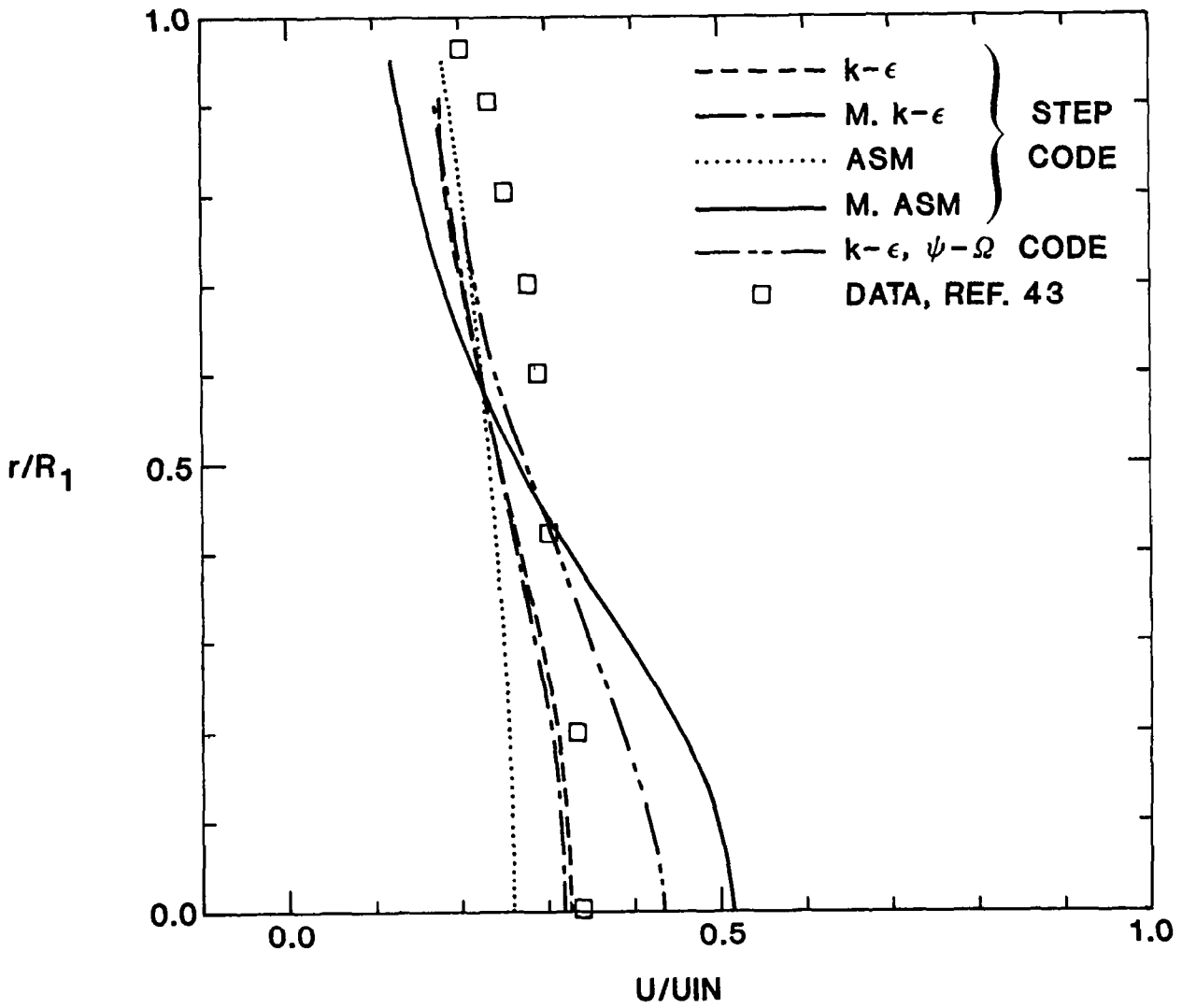

FIGURE 3.17g. U-Velocity Profiles at x/R_1 = 8.00. 2:1 Area Ratio Axisymmetric Expansion, UIN = 31.0 m/s. Data From Chaturvedi, Ref. 43.

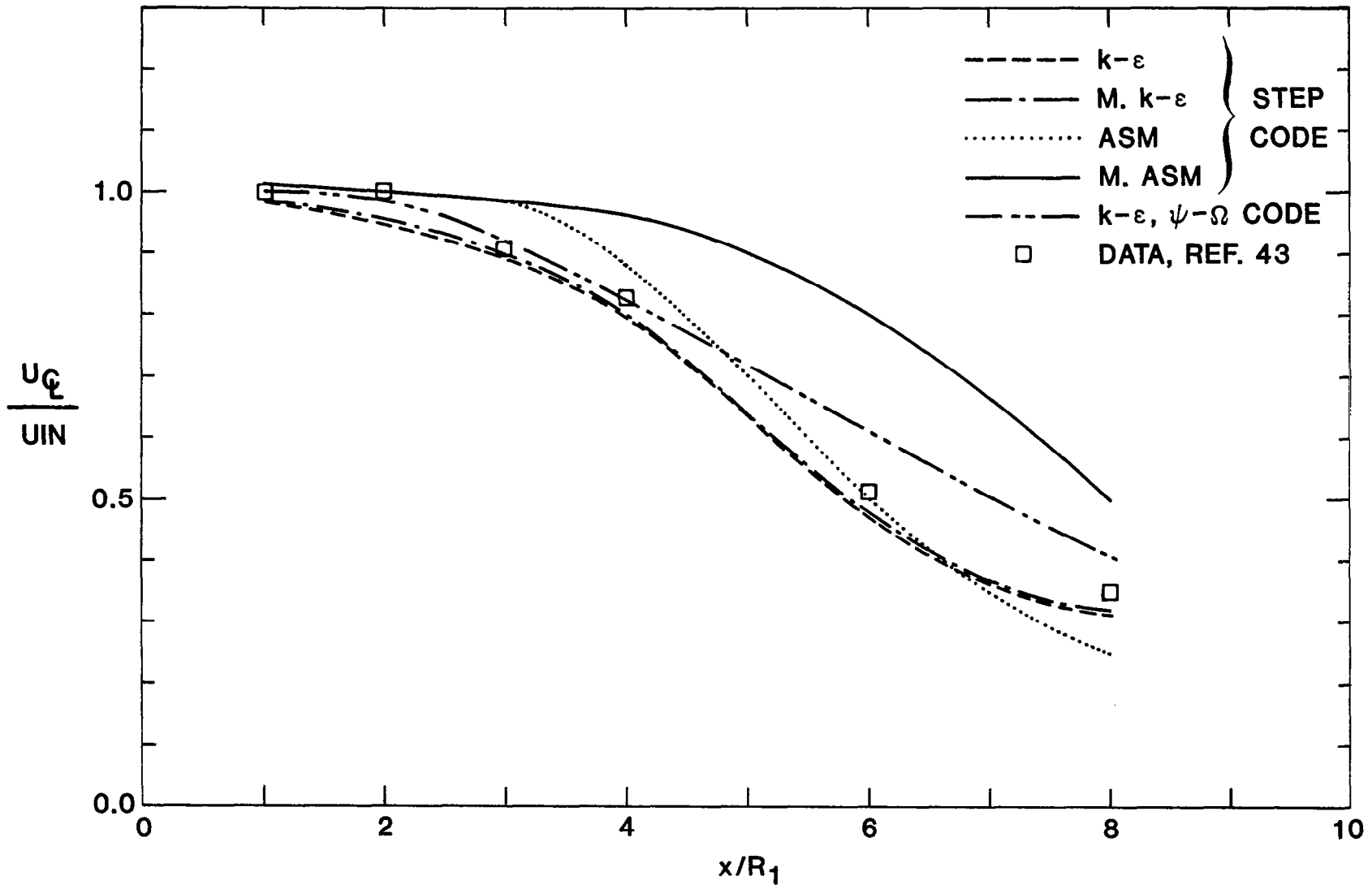

FIGURE 3.18. Streamwise Variation of Centerline Velocity, U_{ℓ}/UIN. 2:1 Area Ratio Axisymmetric Expansion, UIN = 31.0 m/s. Data From Chaturvedi, Ref. 43.

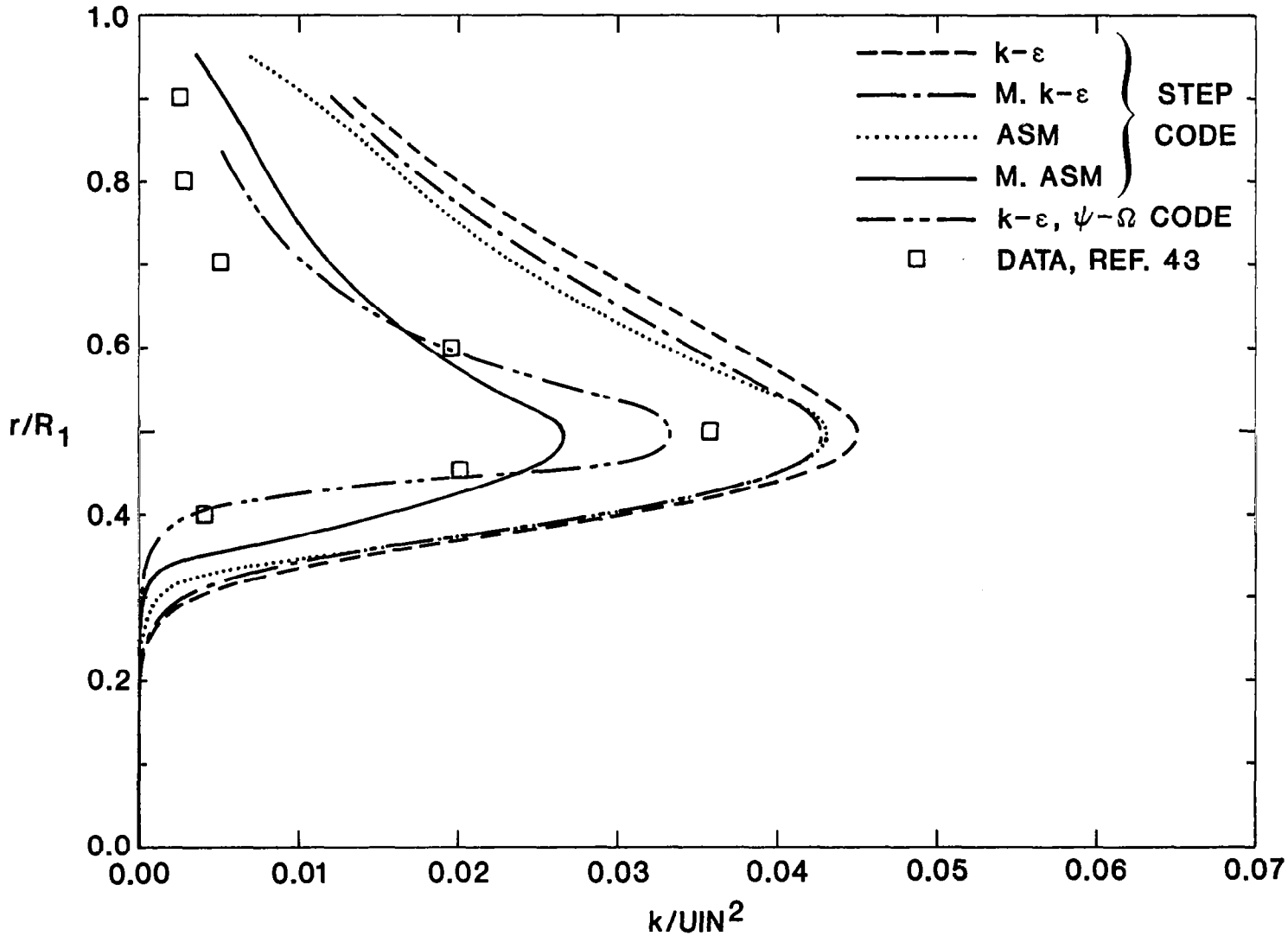

FIGURE 3.19a. k Profiles at x/R_1 = 1.00. 2:1 Area Ratio Axisymmetric Expansion, UIN = 31.0 m/s. Data From Chaturvedi, Ref. 43.

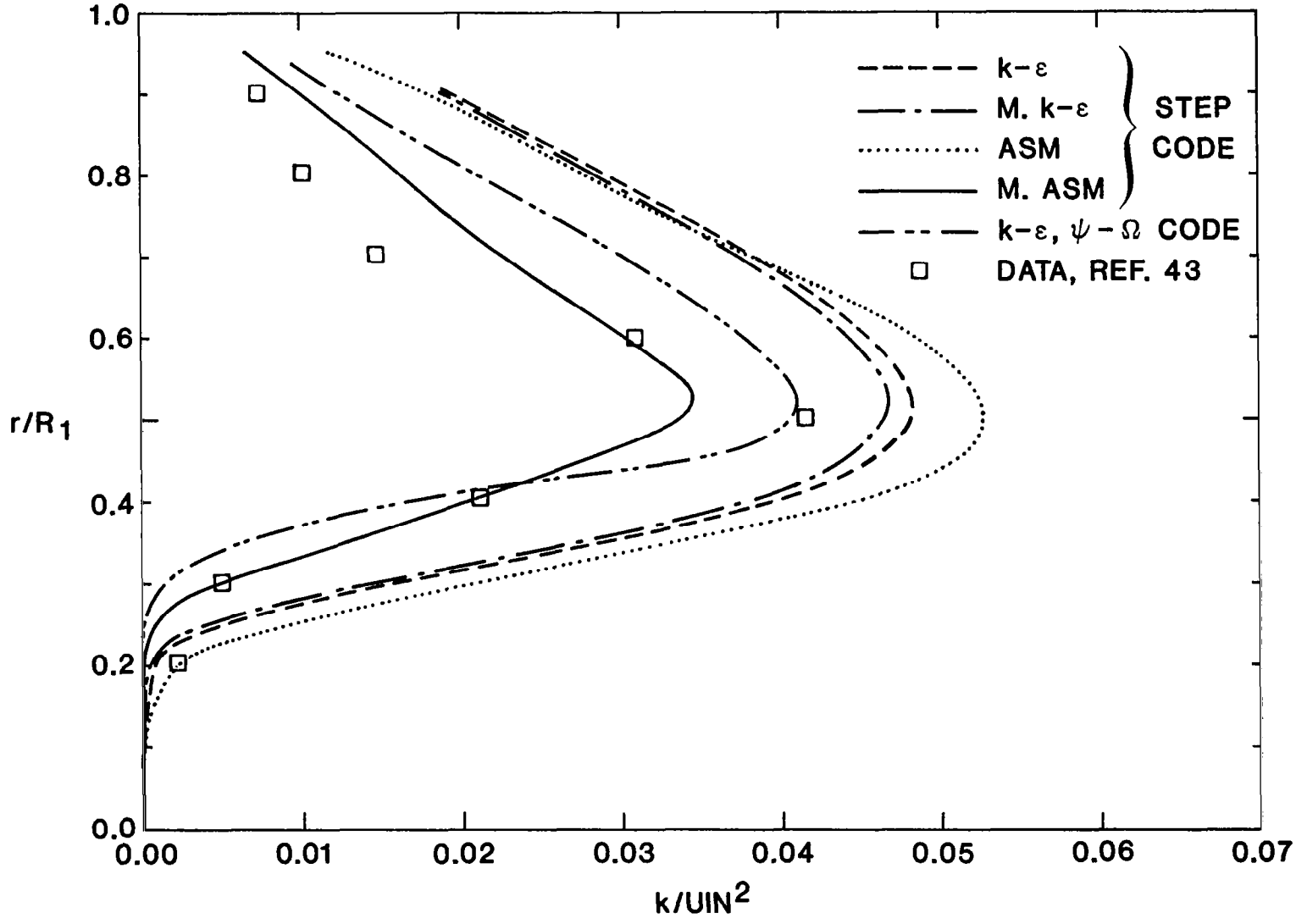

FIGURE 3.19b. k Profiles at x/R_1 = 2.00. 2:1 Area Ratio Axisymmetric Expansion, UIN = 31.0 m/s. Data From Chaturvedi, Ref. 43.

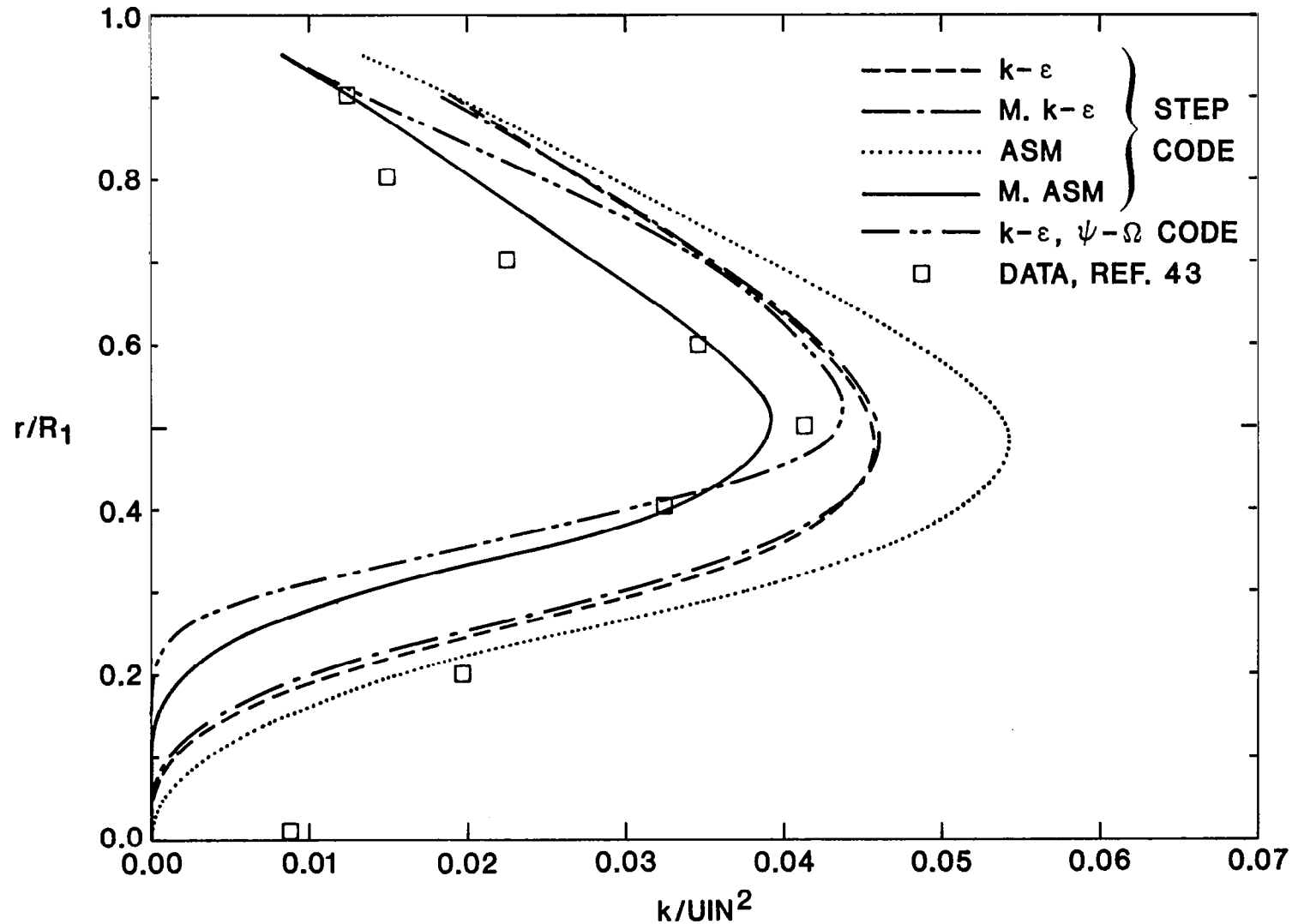

FIGURE 3.19c. k Profiles at x/R_1 = 3.00. 2:1 Area Ratio Axisymmetric Expansion, UIN = 31.0 m/s. Data From Chaturvedi, Ref. 43.

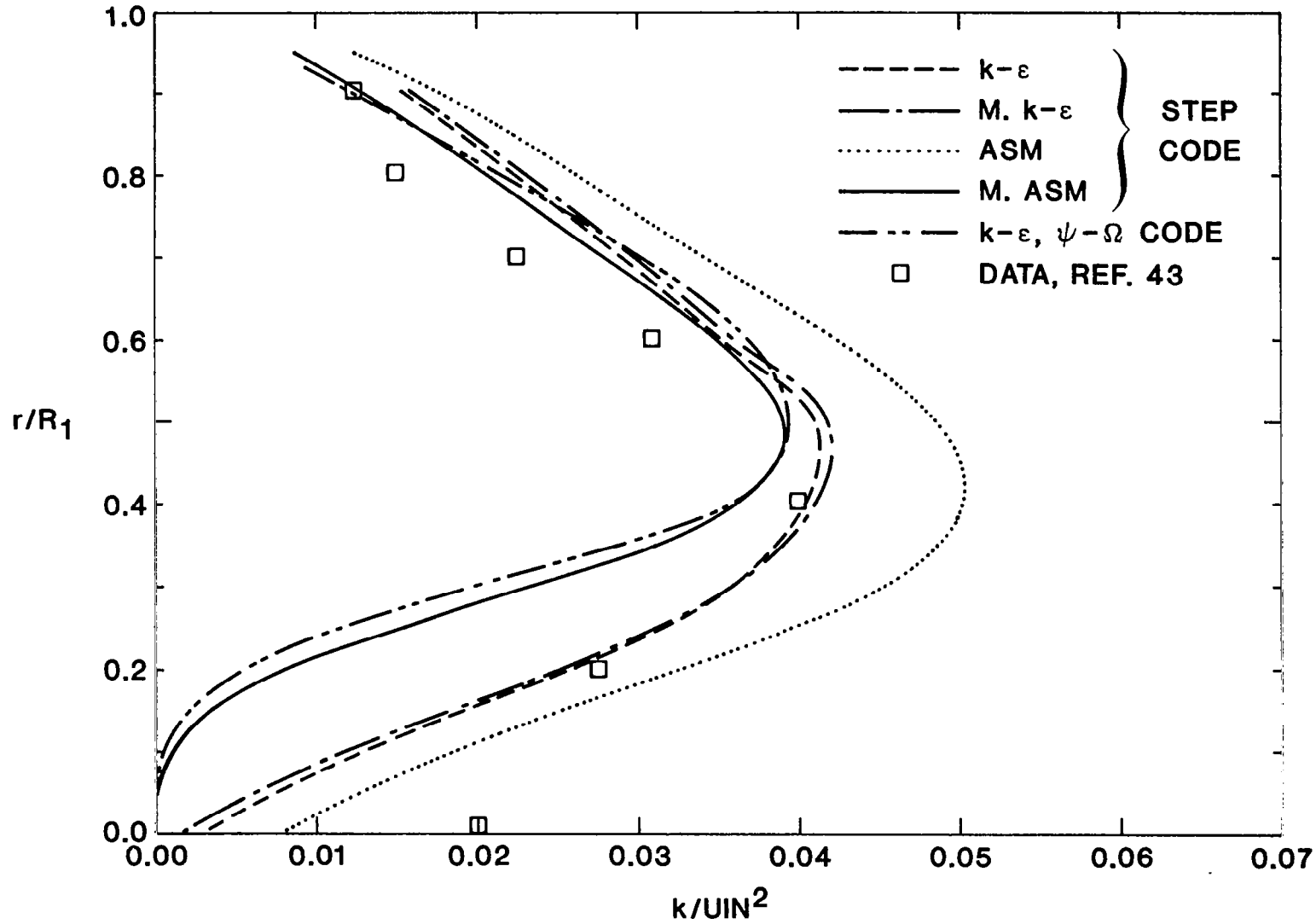

FIGURE 3.19d. k Profiles at $x/R_1 = 4.00$. 2:1 Area Ratio Axisymmetric Expansion, UIN = 31.0 m/s. Data From Chaturvedi, Ref. 43.

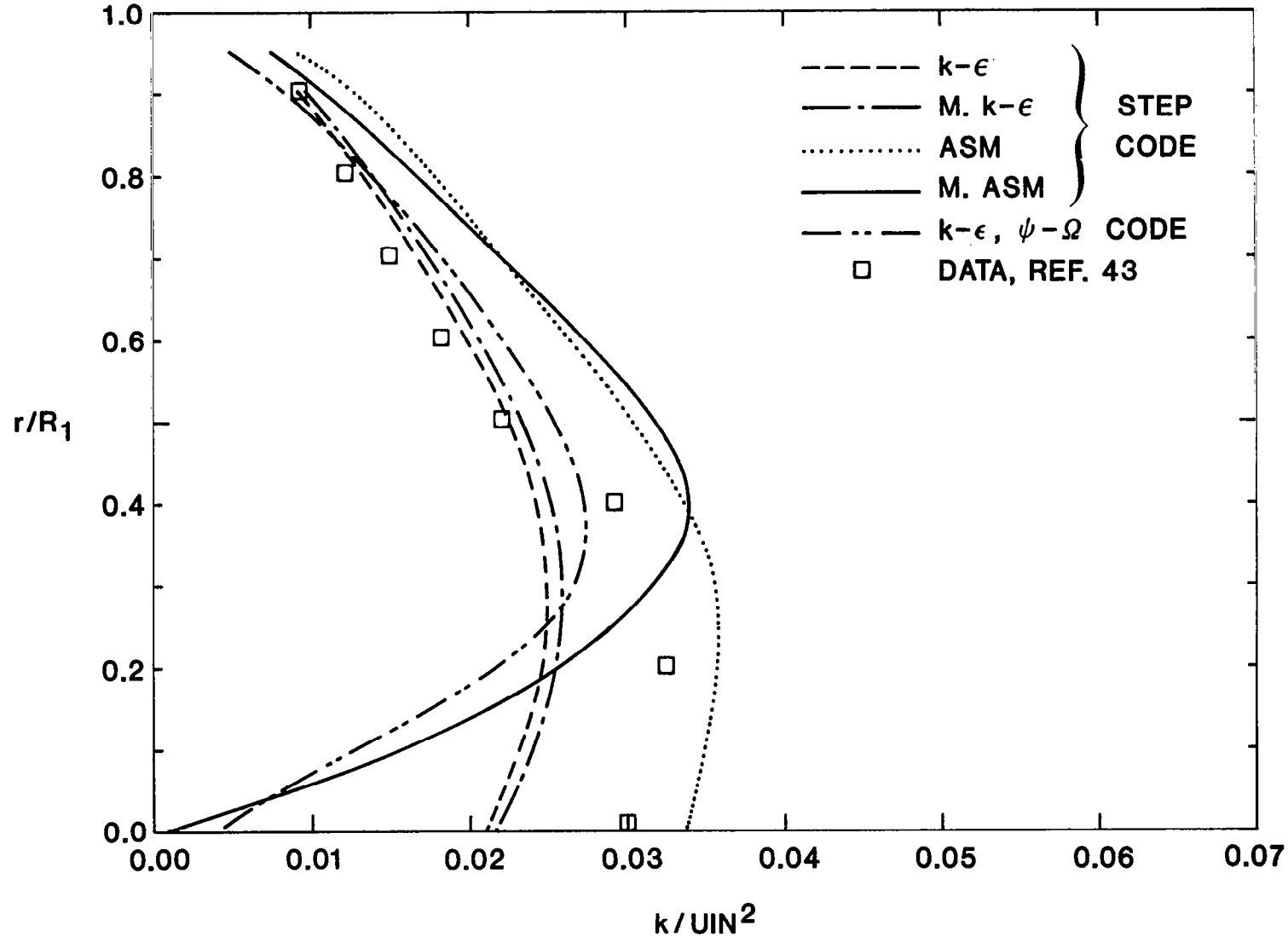

FIGURE 3.19e. k Profiles at x/R_1 = 6.16. 2:1 Area Ratio Axisymmetric Expansion, UIN = 31.0 m/s. Data From Chaturvedi, Ref. 43.

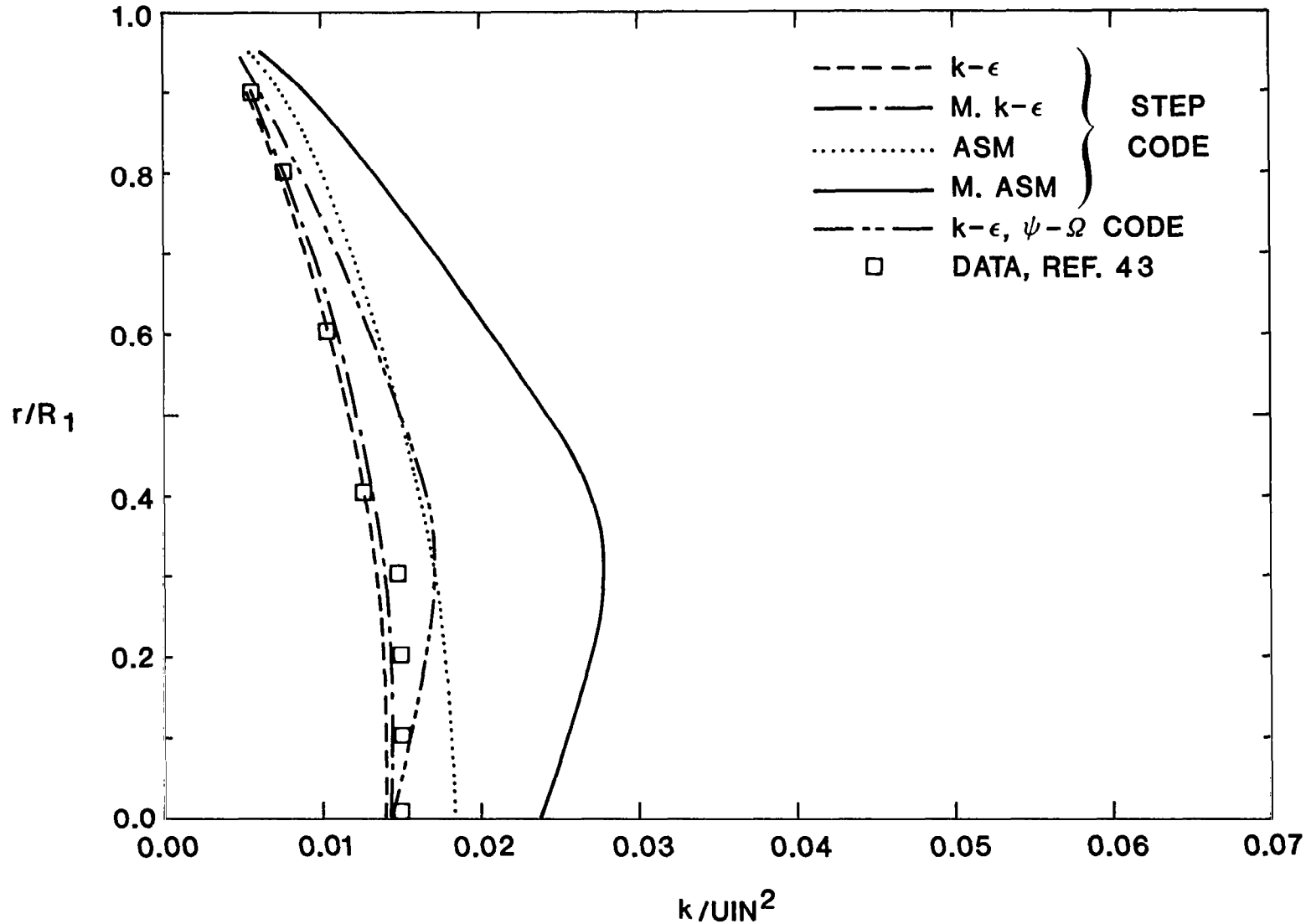

FIGURE 3.19f. k Profiles at x/R_1 = 8.00. 2:1 Area Ratio Axisymmetric Expansion, UIN = 31.0 m/s. Data From Chaturvedi, Ref. 43.

by Chaturvedi is evident near the flow centerline. Some disagreement can also be seen within the recirculation region. In the latter case at least part of the disagreement is related to the assumption $\overline{w^2} = \overline{v^2}$ made in obtaining a turbulent kinetic energy value from the $\overline{u^2}$ and $\overline{v^2}$ data presented by Chaturvedi, but this is not necessarily the case with respect to the near-centerline turbulent kinetic energy levels. In this region the existence of large scale fluctuations in an essentially inviscid flow has been observed in other experiments (Ref. 45), and these fluctuations, which do not directly contribute to the Reynolds stresses, are responsible for the disagreement between the experiment and the theoretical predictions in this region. As mixing proceeds towards the flowfield centerline, the contribution of these large-scale fluctuations to the apparent turbulence e energy decreases, as is evidenced by the rapid convergence of the experimental and predicted turbulent kinetic energy profiles as the flow proceeds downstream, Figures 3.19e and 3.19f. However, some of the energy involved in these large scale motions does contribute to the overall flowfield mixing rate, as is shown by the velocity profiles in Figures 3.17f and 3.17g: this contribution is not adequately accounted for by any of the turbulence models. These results seem to indicate that in low expansion ratio axisymmetric flows, the mean velocity and turbulence predictions do not change significantly with different turbulence models. Simple k-ε model predictions appear to be at least as good as the more sophisticated ASM computations.

The effects of ordered large scale fluctuations on the turbulent energy profile along the flowfield centerline are shown in a fairly dramatic fashion by the centerline turbulent kinetic energy profile comparisons shown in Figure 3.20. However, as Figure 3.20 indicates, the overall effect of this phenomenon on the centerline mean velocity, and thus the overall mixing rate, is small. Figure 3.20 can also be taken to show that the overall results indicate an essentially inviscid deceleration of the flow up to the end of the recirculation region, followed by a turbulent mixing process downstream. The coincidence of the end of the region of "inviscid" deceleration and the reattachment point is a feature of this particular geometry (a 2:1 radius ratio expansion), since shear layer or jet potential core mixing rates are independent of geometry while the reattachment length can be correlated directly with the expansion step height. For these predictions ASM shows relatively good agreement with the data. The standard and

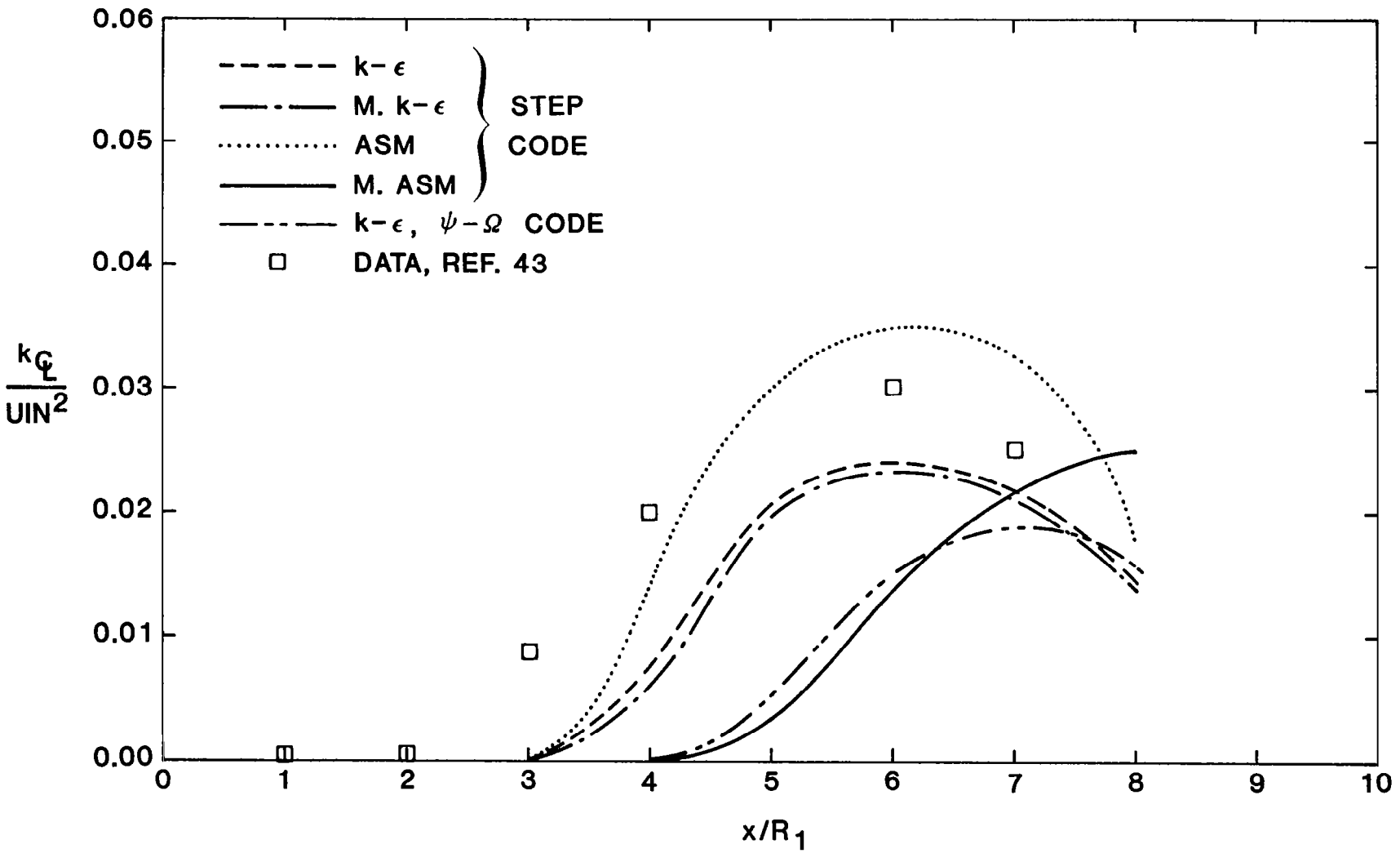

FIGURE 3.20. Streamwise Variation of Centerline k, k_{ℓ}/UIN^2. 2:1 Area Ratio Axisymmetric Expansion, UIN, 31.0 m/s. Data From Chaturvedi, Ref. 43.

"modified" versions of the k-ε model tend to underpredict the magnitude of the turbulence kinetic energy but successfully simulate its behavior along the centerline. Both the "modified" ASM STEP code results and the ψ-Ω code calculations seriously underpredict the data.

Since this study included only one expansion ratio† no definitive conclusions (other than the comments made above) can be drawn on the performance of the models. A follow-up study covering a range of expansion ratios is needed for further evaluation of the models. The discrepancies between the ψ-Ω, k-ε model calculations and the STEP code predictions are probably due to the false diffusion effects associated with the relatively coarse grid used in the STEP code computations.

3.3 SUPERSONIC RECIRCULATING FLOWS

Efforts in this area were concentrated on implementing the k-ε model (Section 2.5) and the non-equilibrium wall-function treatment (Section 2.9) into the TWODLE code developed by J. P. Drummond at NASA-Langley (Ref. 46). Reflecting on the future use of TWODLE it was decided to maintain the built-in turbulence models†† in the code and implement the k-ε model as an option. This required more extensive coding initially but should be beneficial in the sense that:

(1) The original structure of the code (including all subroutines was kept intact; therefore, the code can be executed with or without the k-ε model.

(2) Since the model was implemented into a working code (rather than building the code around the model) initial debugging was expected to be less time consuming.

(3) This modular approach could also facilitate the incorporation of the algebraic stress model which can be introduced as another option.

These considerations led to the model implementation discussed next.

---

†It should be noted that Chaturvedi data were obtained using hot-wire anemometers and relatively primitive techniques. The accuracy of the turbulence data may thus be questionable.

††Basically algebraic eddy viscosity specifications.

3.3.1 Scheme I

The initial approach taken was to incorporate the k and ε transport equations into the MacCormack time-split finite difference technique of TWODLE, and solve them simultaneously with the velocity and, if desired, chemistry fields. This brought about a basic change in the general form of the TWODLE governing equations. A source vector $\vec{H}$ was introduced as shown in equation (A1) of Appendix A to treat the production and dissipation terms associated with the k and ε equations, or any other source-sink term in the governing equations. The new form of the governing equations thus became

$$\frac{\partial \vec{U}}{\partial t} + \frac{\partial \vec{F}}{\partial x} + \frac{\partial \vec{G}}{\partial Y} = H$$

where all the terms are defined in Appendix A for the k-ε model.

Within the TWODLE format two ways of incorporating the k and ε equations into the integration procedure were thought to be possible. One was to solve them in the $L_y(\Delta t/2)\ L_x(\Delta t)\ L_y(\Delta t/2)$ symmetric operator sequence at both the intermediate $\overline{(n+1)}$ and new $(n+1)$ time levels with the generation and destruction terms calculated only during the L_x operator step. The solution algorithm thus became

(1) Guess or specify initial fields for all variables.

(2) Go through the symmetric operator sequence.

$$\left.\begin{array}{l} L_y(\Delta t/2) \\ L_x(\Delta t) \\ L_y(\Delta t/2) \end{array}\right\} \begin{array}{l} \text{Source - sink terms, } \rho(P - \varepsilon) \text{ and } \rho\varepsilon/k(c_{\varepsilon_1} P - c_{\varepsilon_2}\varepsilon), \\ \qquad \text{calculated during the operator step } L_x. \end{array}$$

to obtain the new $(n+1)$ ρ, U, V, k and ε fields.

(3) Calculate μ_t from its definition in terms of c_μ, ρ, k and ε.

(4) Go back to step 2 until steady-state is reached.

The second method was to maintain the practice of solving the k and ε transport equations in the $L_yL_xL_y$ operator sequence, but calculate the source and sink terms at the old (n) time level before the operator sequence was started to advance the time. This changed the solution algorithm to

(1) Guess or specify initial fields for all variables.

(2) Calculate μ_t from its definition in terms of c_μ, ρ, k and ε.

(3) Calculate source and sink terms for the k and ε equations, $\rho(P - \varepsilon)$ and $\rho\varepsilon/k(c_{\varepsilon_1} P - c_{\varepsilon_2}\varepsilon)$, respectively.

(4) Go through the symmetric operator sequence $L_y(\Delta t/2)\ L_x(\Delta t)\ L_y(\Delta t/2)$ to obtain the new $(n + 1)$ ρ, U, V, k and ε fields.

(5) Go back to step 2 until steady-state is reached.

Although both of these approaches seem plausible, many variations within these two methods (especially for the former) were tried without success to achieve stable results. These variations are described in Appendix B; a total of seven approaches were examined. Numerical instabilities due to the stiffness of the source-dominated k and ε transport equations seemed to be the cause of the problem. All non-linear equations display varying degrees of stiffness depending on the nature of the equation, the type and strength of the non-linearity, and the effects of coupling with other equations in the solution algorithm. The k and ε equations are especially stiff in the sense that they are coupled and at high Reynolds numbers[†] they become source-dominated, i.e., the levels of k and ε are determined to a large extent by the relative magnitudes of their generation (source) and destruction (sink) rates. At high Reynolds numbers convective and diffusive transport are comparatively minor. Therefore, the treatment of these source-sink terms is of vital importance in achieving stable results. Our efforts so far have not produced a stable method for treating source-dominated equations in the MacCormack time-split finite difference technique of TWODLE.

3.3.2 Scheme II

This method adopts a new formulation where the k and ε equations are solved only once at each time step after the velocities are advanced in time and the

---

[†]Basically for all flows of aerodynamic interest.

source terms are calculated using these updated velocities. In this formulation the solution algorithm has the following form

(1) Guess or specify initial fields of all variables.

(2) Go through the symmetric operator sequence $L_y(\Delta t/2)\ L_x(\Delta t)\ L_y(\Delta t/2)$ to obtain the new $(n + 1)$ ρ, U and V fields.

(3) Solve the k and ε transport equations (explicitly) using the new $(n + 1)$ velocity and density, and the old (n)k, ε and μ_t fields to obtain the updated $(n + 1)$ k and ε values.

(4) Calculate μ_t from its definition in terms of c_μ, ρ, k and ε.

(5) Go back to step 2 until steady-state is reached.

It should be noted that this method uses a "mixed" time level formulation (U, V and ρ are at the n + 1 level, and k, ε and μ_t are at the n level) and solves the k and ε equations sequentially and explicitly. The finite difference form of the k and ε equations and the changes introduced into TWODLE for model implementation are outlined in Appendix C. With this approach a stable solution appears to be achieved, although the computations have not yet been carried to steady state.

Table 3.5 presents the U-velocity profiles as predicted by the k-ε, and the TWODLE built-in mixing length and Baldwin-Lomax algebraic models for a Mach 5 10° duct compression corner flow. Results were obtained using a 21 by 21 node mesh for a solution domain length of L = 0.1m and a width of h = 0.02m. A uniform inlet velocity profile and turbulence intensity were assumed. A constant[†] Δt of 7.5×10^{-9} second was employed and 1000 time steps[††] were taken. Results show that the k-ε model generally predicts profiles that are in close agreement with the Baldwin-Lomax model. The mixing length model, on the other hand, produces profiles that are less steep in the vicinity of the walls than the other models. The k, ε and μ_t fields as predicted by the k-ε model also

---

[†]A constant Δt was used to aid the stability of the k-ε model.

[††]Computing budget considerations limited the total time steps taken to 1000. Thus steady-state results were not obtained.

TABLE 3.5. U-Velocity Profiles for the Mach 5 10° Ducted Compression Corner Test Case

x/L = 0.20		U/U_{in}		x/L = 0.35		U/U_{in}	
y/h	k-ε	ITURB = 2	ITURB = 1	y/h	k-ε	ITURB = 2	ITURB = 1
0.0	0.0	0.0	0.0	0.132	0.0	0.0	0.0
0.010	0.716	0.699	0.577	0.142	0.610	0.606	0.532
0.026	0.903	0.901	0.835	0.155	0.807	0.806	0.723
0.048	0.967	0.967	0.963	0.174	0.917	0.916	0.865
0.077	0.996	0.997	0.998	0.199	0.937	0.937	0.930
0.117	1.000	1.000	1.000	0.234	0.934	0.961	0.967
0.922	1.000	1.000	1.000	0.279	0.990	0.991	0.994
0.952	1.000	1.000	0.989	0.336	1.000	0.999	1.000
0.974	0.986	0.985	0.871	0.404	1.000	1.000	1.000
0.989	0.884	0.874	0.600	0.482	1.000	1.000	1.000
1.000	0.0	0.0	0.0	0.933	1.000	1.000	0.998
				0.959	0.999	0.999	0.971
				0.977	0.982	0.981	0.816
				0.991	0.870	0.866	0.560
				1.000	0.0	0.0	0.0

Where h is the height of the duct, L is the length of the solution domain, and U_{in} is the maximum inlet velocity. ITURB is a code parameter that controls selection of the turbulence model. ITURB = 1 is a mixing length model for non-recirculating flows and ITURB = 2 is the Baldwin-Lomax algebraic eddy viscosity model.

TABLE 3.5. U-Velocity Profiles for the Mach 5 10° Ducted Compression Corner Test Case (continued)

x/L = 0.50		U/U_{in}		x/L = 0.80		U/U_{in}	
y/h	k-ε	ITURB = 2	ITURB = 1	y/h	k-ε	ITURB = 2	ITURB = 1
0.176	0.0	0.0	0.0	0.176	0.0	0.0	0.0
0.185	0.656	0.631	0.490	0.185	0.762	0.818	0.540
0.198	0.845	0.843	0.701	0.198	0.965	0.970	0.792
0.216	0.946	0.951	0.891	0.216	0.997	0.998	0.967
0.240	0.998	0.998	0.991	0.240	1.000	1.000	0.998
0.272	1.005	1.005	1.003	0.272	1.000	1.000	1.000
0.315	1.002	1.002	1.002	0.315	1.000	1.000	1.000
0.369	1.001	1.001	1.000	0.369	1.000	1.000	1.000
0.434	1.000	1.000	1.000	0.434	1.000	1.000	1.000
0.742	1.000	1.000	1.000	0.742	1.000	1.000	1.000
0.861	1.000	1.000	1.000	0.861	1.000	1.000	1.000
0.904	1.000	1.000	1.000	0.904	1.000	1.000	1.000
0.936	1.000	1.000	0.998	0.936	1.000	1.000	0.998
0.961	0.996	0.997	0.967	0.961	0.997	0.998	0.967
0.978	0.967	0.970	0.793	0.978	0.965	0.970	0.792
0.991	0.818	0.822	0.541	0.991	0.762	0.818	0.540
1.000	0.0	0.0	0.0	1.000	0.0	0.0	0.0

seem plausible. However, before any valid comparisons can be made between the models steady-state results should be obtained for a number of test cases representing both elliptic and parabolic flows.

From these results, it appears that a stable way of incorporating the k-ε model has been devised: no instabilities were encountered within 1000 time steps. However, in its present form this scheme has two drawbacks: firstly, it requires a small time step (approximately 2 orders of magnitude smaller than the time step used with the other models) and secondly, the k and ε transport equations are solved in the physical rather than in the transformed coordinates, which introduces inaccuracies for irregular geometries. The first drawback can be eliminated by devising an implicit solution algorithm (ADI, block-solver, etc.); ideally the k and ε equations will be solved simultaneously (not sequentially) using a linearization technique such as Newton-Raphson. This will remove the small time step restriction and produce results that are more plausible (since physically things do happen simultaneously). The second drawback can be removed by solving the k and ε equations in the transformed coordinates of TWODLE. This is straightforward analytically, but in practice it would require extensive programming efforts and code changes. Both of these suggestions are important and should be considered in future code development efforts if this method is adopted. If, however, a new implicit version of TWODLE that does not use time-split finite differencing is available in the near future, the k and ε transport equations may be successfully implemented into that solution algorithm since the problems with the initial version of TWODLE were largely due to the time-split finite differencing technique.

4. CONCLUSIONS AND FUTURE WORK

The conclusions reached from the work outlined in this report can be summarized as follows.

4.1 SUBSONIC PLANAR RECIRCULATING FLOWS

(a) The relative performance of the models in subsonic plane backward-facing step flow computations is region-dependent, i.e., best predictions are not necessarily obtained by the same model in both the reverse flow and recovery regimes.

(b) The "modified" ASM produces the best predictions in the reverse flow region but computes too slow a recovery rate in the relaxation regime where the other models show better agreement with data.

(c) A modular approach that uses the "modified" ASM in the reverse flow region and the standard version in the recovery regime appears to be the most appropriate scheme in predicting subsonic plane backward-facing step flows.

(d) The standard and multi-scale k-ε models are not recommended for subsonic planar recirculating flow predictions. However, the concept of multi-time and -length scales is physically sound, and is also appealing in the sense that it enables separate modeling of each energy region in turbulent flows.

4.2 SUBSONIC AXISYMMETRIC RECIRCULATING FLOWS

Evaluation of the relative performance of the models in subsonic axisymmetric backward-facing step flow calculations was not attempted since only one diameter ratio (2:1) was tested. Preliminary results indicate very little difference between the k-ε, "modified" k-ε, and ASM predictions; all show good agreement with the Chaturvedi (Ref. 43) data. The "modified" ASM predicts too long a reattachment length and consequently suffers from scaling problems. More diameter ratios need to be tested before the above observations can be generalized.

4.3 SUPERSONIC RECIRCULATING FLOWS

Incorporation of the k-ε model in TWODLE for supersonic recirculating flow predictions was hindered by numerical stability problems. Finally, a scheme was devised that appears to be stable but requires a very small time step due to the explicit nature of the scheme. Also, the fact that the k and ε transport equations are solved in the physical coordinates may introduce inaccuracies for irregular geometries. Two options are available: modify this scheme so that the k and ε equations are solved implicitly and simultaneously in the transformed coordinates, or implement the k-ε model into the new implicit version of TWODLE that does not use time-split finite differencing.

4.4 FUTURE WORK

Future work in the examination of turbulence models for application to SCRAMJET combustors is expected to concentrate in three major areas. The examination of turbulence model performance in axisymmetric recirculating flows will be extended to a greater range of diameter ratios to examine whether the model performance observed in the work discussed in this report shows similar characteristics at other area ratios. Implementation of turbulence models in the supersonic-flow TWODLE code will continue, with further refinement of the k-ε two-equation formulation and incorporation of an ASM formulation as well. Questions that have arisen from this work regarding the use of an explicit formulation for the turbulence model have ramifications not only with respect to computational techniques but also with respect to the architecture of the computer utilized, and these will be further investigated. Finally, the turbulence model assessment work will be extended to reacting flows with an emphasis on the development and implementation of techniques to account for turbulence-finite rate chemical kinetics interaction.

All of this work has as its goal the definition of a set of turbulence models suitable for the different characteristic regions encountered in a scramjet flowfield. Along with this definition, algorithms to allow transition from one turbulence model to another within the context of a given flowfield solution procedure are to be developed. Major strides toward the definition of suitable turbulence models for different flowfield regions have been made in the work

described in this report, and the work currently underway is expected to complete the turbulence model definition effort.

REFERENCES

1. Fabris, G.; Harsha, P. T.; and Edelman, R. B.: Multiple-Scale Turbulence Modeling of Boundary Layer Flows for Scramjet Applications. NASA Contractor Report 3433, May 1981.

2. Hanjalic, K.; and Launder, B. E.: Sensitizing the Dissipation Equation to Irrotational Strains. J. Fluids Engineering, Trans. ASME, vol. 102, March 1980, pp. 34-40.

3. Hanjalic, K.; Launder, B. E.; and Schiestel, R.: Multiple-Time Scale Concepts in Turbulent Transport Modeling. Second Symposium on Turbulent Shear Flows, Imperial College, London, July 1979.

4. Rodi, W.: The Prediction of Free Turbulent Boundary Layers by Use of a Two-Equation Model of Turbulence. Ph.D. Thesis, University of London, 1972.

5. Sindir, M. M.: Numerical Study of Turbulent Flows in Backward-Facing Step Geometries: Comparison of Four Models of Turbulence. Ph.D. Thesis, University of California, Davis, June 1982.

6. Daly, B. T.; and Harlow, F. H.: Transport Equations in Turbulence. Phys. Fluids, vol. 13, 1970, pp. 2634-2649.

7. Donaldson, C. du P.: A Computer Study of Boundary Layer Transition. AIAA Journal, vol. 7, 1969, pp. 271-278.

8. Rotta, T. A.: Statistische Theorie Nichthomogener Turbulens, Z. Phys., vol. 129, 1951, pp. 547-572.

9. Chou, P. Y.: On Velocity Correlations and the Solution of the Equations of Turbulent Fluctuation. Quart. J. Applied Mathematics, vol. 3, 1945, pp. 38-45.

10. Bradshaw, P.: Outlook for Three-Dimensional Procedures. Proceedings, Computation of Turbulent Boundary Layers - 1968, AFOSR-IFP-Stanford Conference, vol. 1, Methods, Predictions, Evaluation, and Flow Structure, pp. 427-433.

11. Lumley, T. L.; and Khajeh Nouri, B. J.: Computational Modeling of Turbulent Transport. Adv. Geophys., vol. 18A, 1974, pp. 169-192.

12. Launder, B. E.; Morse, A.; Rodi, W.; and Spalding, D. B.: The Prediction of Free Shear Stress Flows - A Comparison of the Performance of Six Turbulence Models. Free Turbulent Shear Flows, vol. I - Conference Proceedings, NASA SP 321, 1973, pp. 361-426.

13. Naot, D; Shavit, A.; and Wolfstein, M.: Two-Point Correlation Model and the Redistribution of the Reynolds Stress. Phys. Fluids, vol. 16, 1973, pp. 738-743.

14. Launder, B. E.; Reece, G. J.; and Rodi, W.: Progress in the Development of a Reynolds Stress Turbulence Closure. J. Fluid Mechanics, vol. 68, 1975, pp. 537-566.

15. Gibson, M. M.; and Launder, B. E.: Ground Effects on Pressure Fluctuations in the Atmospheric Boundary Layer. J. Fluid Mechanics, vol. 86, Part 3, 1978, pp. 491-511.

16. Samaraweera, D. S. A.: Turbulent Heat Transport in Two and Three-Dimensional Temperature Fields. Ph.D. Thesis, University of London, 1978.

17. Shir, C. C.: A Preliminary Numerical Study of Atmospheric Turbulent Flows in the Idealized Planetary Boundary Layer. J. Atmospheric Sciences, vol. 30, 1973, pp. 1327-1339.

18. Irwin, H. P. A. H.: Measurements of a Self-Preserving Plane Wall Jet in a Positive Pressure Gradient. J. Fluid Mechanics, vol. 61, 1973, pp. 33-63.

19. Lumley, J. L.: Prediction Methods for Turbulent Flow - Introduction. Von Karman Institute for Fluid Dynamics, Lecture Series, no. 76, 1975.

20. Hanjalic, K.; and Launder, B. E.: A Reynolds Stress Model of Turbulence and Its Application to Thin Shear Flows. J. Fluid Mechanics, vol. 52, 1972, pp. 609-638.

21. Reece, G. J.: A Generalized Reynolds Stress of Turbulence. Ph.D. Thesis, University of London, 1977.

22. Jones, W. P.; and Launder, B. E.: The Prediction of Laminarization with a Two-Equation Model of Turbulence. Int. J. Heat and Mass Transfer, vol. 15, 1972, pp. 301-314.

23. Tennekes, H.; and Lumley, J. L.: A First Course in Turbulence, 1972, MIT Press.

24. Hirt, C. W.: Generalized Turbulent Transport Equations. Los Alamos Sci. Lab. Report 1-13, 1969.

25. Pope, S. B.: An Explanation of the Turbulent Round Jet/Plane Jet Anomaly. Report No. FS/77/12, Dept. of Mechanical Engineering, Imperial College, 1977.

26. Chieng, C. C.; and Launder, B. E.: On the Calculation of Turbulent Heat Transport Downstream of an Abrupt Pipe Expansion. Numerical Heat Transfer, vol. 3, 1980, pp. 189-207.

27. Launder, B. E.; and Spalding, D. B.: The Numerical Computation of Turbulent Flows. Computer Methods in Applied Mechanics and Engineering, vol. 3, 1974, pp. 269-289.

28. Pope, S. B.; and Whitelaw, J. H.: The Calculation of Near-Wake Flows. J. Fluid Mechanics, vol. 73, 1976, pp. 9-30.

29. Spalding, D. B.: Heat Transfer from Turbulent Separated Flows. J. Fluid Mechanics, vol. 27, 1967, pp. 97-109.

30. Warren, W. R.: An Analytical and Experimental Study of Compressible Free Jets. Aeronautical Engineering Laboratory, Report 381, Princeton University, 1957.

31. Eggers, J. M.: Velocity Profiles and Eddy Viscosity Distributions Downstream of a Mach 2.22 Nozzle Exhausting to Quiescent Air. NASA TN D-3601, September 1966.

32. Broer, L. J. F.; and Rietdijk, J. A.: Measurements in Supersonic Free Jets. Applied Scientific Research, Section A, vol. 9, 1960, pp. 465-477.

33. Alexander, L. G.; Baron, T.; and Comings, E. W.: Transport of Momentum, Mass, and Heat in Turbulent Jets. Bulletin 413, University of Illinois Engineering Experiment Station, May 1953.

34. Laurence, J. C.: Scale and Spectra of Turbulence in the Mixing Region of a Free Subsonic Jet. NACA TN1292, 1956.

35. Johannesen, N. H.: Further Results on the Mixing of Free Axially-Symmetric Jets of Mach Number 1.40. R & M No. 3292, Aeronautical Research Council (G.B.) 1962.

36. Birch, S. F.; and Eggers, J. M.: A Critical Review of the Experimental Data for Developed Free Turbulent Shear Layers. Free Turbulent Shear Flows, vol. I - Conference Proceedings, NASA SP 321, 1973, pp. 11-40.

37. Abbott, D. E.; and Kline, S. J.: Experimental Investigation of Subsonic Turbulent Flow Over Single and Double Backward-Facing Steps. J. Basic Engineering, vol. 84, series D. 1962, pp. 317-325.

38. Driver, D. M.; and Seegmiller, H. L.: Features of a Reattaching Shear Layer Subject to Adverse Pressure Gradient. AIAA Paper 82-1029, AIAA/ASME Third Joint Thermophysics, Fluids, Plasma and Heat Transfer Conference, June 1982.

39. Kim, J.; Kline, S. J.; and Johnston, J. P.: Investigation of Separation and Reattachment of a Turbulent Shear Layer: Flow Over a Backward-Facing Step. Report MD-37, Thermosciences Division, Department of Mechanical Engineering, Stanford University, 1978.

40. Gessner, F. G.; and Eppich, H. M.: A Near-Wall Pressure-Strain Model for Turbulent Corner Flows. Proceedings Third Symposium on Turbulent Shear Flows, University of California, Davis, 1981, pp. 2.25-2.32.

41. Habib, M. A. and Whitelaw, J. H.: Velocity Characteristics of a Confined Coaxial Jet. Journal of Fluids Engineering, vol. 101, December 1979, pp. 521-529.

42. Spalding, D. B.: A Novel Finite-Difference Formulation for Differential Expressions Involving Both First and Second Derivatives. Int. J. Numerical Methods in Engineering, vol. 4, 1972, pp. 551-559.

43. Chaturvedi, M. C.: Flow Characteristics of Axisymmetric Expansion. Journal of the Hydraulics Division, Proc. ASCE, vol. 89, no. HY3, May 1963, pp. 61-92.

44. Schmotolocha, S. N.; and Phung, P. V.: Characteristics of Dump Combustor Flowfields With and Without Chemical Reactions. Proceedings 17th JANNAF Combustion Meeting, vol. III, Publication 329, Chemical Propulsion Information Agency, November 1980, pp. 547-584.

45. Owen, F. K.: Laser Velocimeter Measurements of a Confined Turbulent Diffusion Flame Burner. AIAA Paper 76-33, AIAA 14th Aerospace Sciences Meeting, January 1976.

46. Drummond, J. P.; and Weidner, E. G.: Numerical Study of a Scramjet Engine Flowfield. AIAA Paper 81-0186, AIAA 19th Aerospace Sciences Meeting, January 1981.

APPENDIX A

THE k-ε MODEL FORMULATION FOR THE TWODLE CODE

The mean flow and turbulence model equations for the k-ε model can be written as follows for two-dimensional elliptic planar flows:

Conservation of Mass

$$\frac{\partial \rho}{\partial t} + \frac{\partial}{\partial x} \rho U + \frac{\partial}{\partial y} \rho V = 0$$

x-Momentum

$$\frac{\partial}{\partial t} \rho U + \frac{\partial}{\partial x} \rho U^2 + \frac{\partial}{\partial y} \rho UV$$

$$= - \frac{\partial P}{\partial x} + \frac{\partial}{\partial x} \left[2\mu_T \frac{\partial U}{\partial x} - 2/3\mu_T \left(\frac{\partial U}{\partial x} + \frac{\partial V}{\partial y} \right) - 2/3\rho k \right] + \frac{\partial}{\partial y} \left[\mu_T \left(\frac{\partial U}{\partial y} + \frac{\partial V}{\partial x} \right) \right]$$

y-Momentum

$$\frac{\partial \rho V}{\partial t} + \frac{\partial}{\partial x} \rho UV + \frac{\partial}{\partial y} \rho V^2$$

$$= - \frac{\partial P}{\partial y} + \frac{\partial}{\partial x} \left[\mu_T \left(\frac{\partial U}{\partial y} + \frac{\partial V}{\partial x} \right) \right] + \frac{\partial}{\partial y} \left[2\mu_T \frac{\partial V}{\partial y} - 2/3\mu_T \left(\frac{\partial U}{\partial x} + \frac{\partial V}{\partial y} \right) - 2/3\rho k \right]$$

k transport equation

$$\frac{\partial \rho k}{\partial t} + \frac{\partial}{\partial x} \rho Uk + \frac{\partial}{\partial y} \rho Vk = \rho P - \rho \varepsilon + \frac{\partial}{\partial x} \left[\left(\frac{\mu_t}{\sigma_k} + \mu \right) \frac{\partial k}{\partial x} \right] + \frac{\partial}{\partial y} \left[\left(\frac{\mu_t}{\sigma_k} + \mu \right) \frac{\partial k}{\partial y} \right]$$

ε Transport Equation

$$\frac{\partial \rho \varepsilon}{\partial t} + \frac{\partial}{\partial x} \rho U\varepsilon + \frac{\partial}{\partial y} \rho V\varepsilon$$

$$= c_{\varepsilon_1} \rho \frac{\varepsilon}{k} P - c_{\varepsilon_2} \rho \frac{\varepsilon^2}{k} + \frac{\partial}{\partial x} \left[\left(\frac{\mu_t}{\sigma_\varepsilon} + \mu \right) \frac{\partial \varepsilon}{\partial x} \right] + \frac{\partial}{\partial y} \left[\left(\frac{\mu_t}{\sigma_\varepsilon} + \mu \right) \frac{\partial \varepsilon}{\partial y} \right]$$

where

U = streamwise mean velocity component

V = transverse mean velocity

P = pressure

k = turbulence kinetic energy

ε = turbulence kinetic energy dissipation rate

ρ = density

μ = dynamic viscosity

P = production rate of k, $\frac{\mu_t}{\rho}\left\{2\left[\left(\frac{\partial U}{\partial x}\right)^2+\left(\frac{\partial V}{\partial x}\right)^2\right]+\left(\frac{\partial U}{\partial y}+\frac{\partial V}{\partial x}\right)^2-\frac{2}{3}\left(\frac{\partial U}{\partial x}+\frac{\partial V}{\partial y}\right)^2\right\}$

$- 2/3k\left(\frac{\partial U}{\partial x}+\frac{\partial V}{\partial y}\right)$

$\mu_T = \mu_t + \mu$ (total viscosity)

$\mu_t = c_\mu \rho \frac{k^2}{\varepsilon}$ (turbulent viscosity)

σ_k and σ_ε are the Prandtl numbers for k and ε, respectively, and c_{ε_1}, c_{ε_2} and c_μ are constants.

Following Ref. 46 these equations can be put in TWODLE form by defining the $\vec{U}$, $\vec{F}$, $\vec{G}$ and $\vec{H}$ vectors as

$$\frac{\partial \vec{U}}{\partial t}+\frac{\partial \vec{F}}{\partial x}+\frac{\partial \vec{G}}{\partial y}=\vec{H} \qquad \text{(A1)}$$

where

$$\vec{U} = \begin{Bmatrix} \rho \\ \rho U \\ \rho V \\ \rho k \\ \rho \varepsilon \end{Bmatrix}$$

$$\vec{F} = \begin{Bmatrix} \rho U \\ \rho UU + \sigma_x \\ \rho UV + T_{xy} \\ \rho UK + D_{k_x} \\ \rho U\varepsilon + D_{\varepsilon_x} \end{Bmatrix}$$

$$\vec{G} = \begin{cases} \rho V \\ \rho UV + T_{yx} \\ \rho VV + \sigma_y \\ \rho Vk + D_{k_y} \\ \rho V\varepsilon + D_{\varepsilon_y} \end{cases}$$

$$\vec{H} = \begin{cases} 0 \\ 0 \\ 0 \\ \rho(P - \varepsilon) \\ \rho\varepsilon/k(c_{\varepsilon_1} P - c_{\varepsilon_2}\varepsilon) \end{cases}$$

and

$$\sigma_x = P + 2/3\mu_T D - 2\mu_T \frac{\partial U}{\partial x} + 2/3\rho k \tag{A2}$$

$$T_{xy} = T_{yx} = -\mu_T \left(\frac{\partial U}{\partial y} + \frac{\partial V}{\partial x}\right) \tag{A3}$$

$$\sigma_y = P + 2/3\mu_T D - 2\mu_T \frac{\partial V}{\partial y} + 2/3\rho k \tag{A4}$$

$$D_{k_x} = -\left(\frac{\mu_t}{\sigma_k} + \mu\right) \frac{\partial k}{\partial x} \tag{A5}$$

$$D_{\varepsilon_x} = -\left(\frac{\mu_t}{\sigma_\varepsilon} + \mu\right) \frac{\partial \varepsilon}{\partial x} \tag{A6}$$

$$D_{k_y} = -\left(\frac{\mu_t}{\sigma_k} + \mu\right) \frac{\partial k}{\partial y} \tag{A7}$$

$$D_{\varepsilon_y} = -\left(\frac{\mu_t}{\sigma_\varepsilon} + \mu\right) \frac{\partial \varepsilon}{\partial y} \tag{A8}$$

$$\mu_t = \rho c_\mu \frac{k^2}{\varepsilon} \tag{A9}$$

$$\mu_T = \mu_t + \mu \tag{A10}$$

$$P = \frac{\mu_t}{\rho}\left\{2\left[\left(\frac{\partial U}{\partial x}\right)^2 + \left(\frac{\partial V}{\partial y}\right)^2\right] + \left(\frac{\partial U}{\partial y} + \frac{\partial V}{\partial x}\right)^2 - \frac{2}{3}D^2\right\} - 2/3kD \tag{A11}$$

$$\sigma_k = 3/2\,\frac{c_\mu}{c_{k_1}} \tag{A12}$$

$$\sigma_\kappa = \frac{K^2}{(c_{\varepsilon_2} - c_{\varepsilon_1})c_\mu^{1/2}} \tag{A13}$$

$$D = \begin{cases} \dfrac{\partial U}{\partial x} + \dfrac{\partial V}{\partial y} & \text{compressible flows} \\ 0 & \text{incompressible flows} \end{cases}$$

Currently recommended values for the constants are

$c_\mu = 0.09$

$c_{k_1} = 0.22$

$c_{\varepsilon_1} = 1.44$

$c_{\varepsilon_2} = 1.92$

$K = 0.4187$

with these values σ_k and σ_ε become

σ_k[†] $\simeq 1.0$

$\sigma_\varepsilon \simeq 1.217$

[†] σ_k actually becomes 0.614, however a value of 1 is more common in the literature. There are no significant differences in the predictions obtained with these two values.

APPENDIX B

UNSUCCESSFUL APPROACHES TO THE INCORPORATION OF THE TWO-EQUATION k-ε MODEL IN THE TWODLE CODE

Several variations within the confines of one approach to the incorporation of the two-equation k-ε turbulence model in the TWODLE code were examined during this program. Although all were ultimately unsuccessful, they are outlined in this Appendix so that similar problems with other stiff equation subsets may be avoided in numerical algorithms similar to that used in TWODLE. Testing was carried out for a Mach 5 10° ducted expansion-compression case using a 21 by 21 mesh. Numerical stability problems were encountered due to the stiffness of the source - dominated k and ε transport equations (equation (A1) in Appendix A).

Within the TWODLE format there are at least two ways of incorporating the k and ε equations into the solution procedure. One is to solve them sequentially in the $L_y(\Delta t/2)\ L_x(\Delta t)\ L_y(\Delta t/2)$ symmetric operator sequence at both the intermediate $(\overline{n+1})$ and new $(n+1)$ time levels with the generation and destruction terms calculated only during the L_x operator step. The second way is to solve them only once at each time step (n to n + 1) after the velocities are advanced in time and source terms are calculated using these updated velocities. Within the first mentioned scheme, seven different variations were tested to overcome the stiffness problem. These are discussed next.

The seven schemes tested cover a range of source-sink treatments from fully-explicit to variations within a quasi-implicit formulation. The diffusion and convection terms are calculated explicitly in each case. The general form of the source-sink terms for the k and ε equations are recalled from equation (A1) as

$$\rho(P - \varepsilon) \text{ for } k, \tag{B1}$$

and

$$\rho\varepsilon/k(c_{\varepsilon_1} P - c_{\varepsilon_2}) \text{ for } \varepsilon, \tag{B2}$$

where all the terms are defined in Appendix A. Details of each treatment are summarized below in connection with these two expressions. In all cases a constant Δt of 7.5×10^{-9} sec was used throughout the computations.

Case 0

This is the fully explicit case where ρ, P, ε, and k are all evaluated at the old time level.

Calculations became unstable after 59 time steps.

Case 1

This is the first variation within the quasi-implicit formulation. P is calculated implicitly after the new velocity field is obtained. ρ, ε, and k are explicit at the old time level.

Calculations became unstable after 59 time steps.

Case 2

This is the second variation within the quasi-implicit formulation. P and ρ are calculated implicitly after the new velocity field is obtained. ε and k are explicit at the old time level.

Calculations became unstable after 59 time steps.

Case 3

This is the third variation within the quasi-implicit formulation. P and ρ are calculated implicitly after the new velocity field is obtained. The k that appears in equation (B2) is now substituted for by the new k value. ε is explicit at the old time level.

Calculations became unstable after 62 time steps.

Case 4

This is the fourth variation within the quasi-implicit formulation. P and ρ are calculated implicitly after the new velocity field is obtained. The term ε/k that appears in equation (B2) is now calculated as

$$\varepsilon/k = \frac{c_\mu \rho k^2/\mu_t}{k} = \frac{c_\mu \rho k}{\mu_t}$$

where both ρ and k are at the new time level. ε is explicit at the old time.

Calculations became unstable after 60 time steps.

Case 5

This is the fifth variation within the quasi-implicit formulation. P and ρ are calculated implicitly after the new velocity field is obtained. The terms ε/k and ε that appear in equation (B2) are now calculated as

$$\varepsilon/k = \frac{c_\mu \rho k^2/\mu_t}{k} = \frac{c_\mu \rho k}{\mu_t}$$

and

$$\varepsilon = \frac{c_\mu \rho k^2}{\mu_t}$$

respectively, where both ρ and k are at the new time level. ε in equation (B1) is explicit at the old time.

Calculations become unstable after 59 time steps.

Case 6

This is the sixth and final variation within the quasi-implicit formulation. P and ρ are calculated implicitly after the new velocity field is obtained. The term ε in equation (B1) is calculated as

$$\varepsilon = c_\mu \rho k^2/\mu_t$$

where both ρ and k are at the old time level. The ε/k and ε terms that appear in equation (B2) are calculated as

$$\varepsilon/k = \frac{c_\mu \rho k}{\mu_t}$$

and

$$\varepsilon = \frac{c_\mu \rho k^2}{\mu_t}$$

respectively, where both ρ and k are now at the new time level. Calculations go unstable after 27 time steps.

APPENDIX C

FINITE DIFFERENCE FORM OF THE k AND ε TRANSPORT EQUATIONS FOR THE TWODLE CODE

The finite difference forms given below use a "mixed" time level formulation where U, V, ρ are at the new n + 1 time level, and k, ε, μ_t are at the old time level n.

C.1 k Transport Equation

$$\frac{\partial}{\partial t}\rho k + \frac{\partial}{\partial x}\rho U k + \frac{\partial}{\partial y}\rho V k = \rho P - \rho\varepsilon + \frac{\partial}{\partial x}\left(\frac{\mu_t}{\sigma_k} + \mu\right)\frac{\partial k}{\partial x} + \frac{\partial}{\partial y}\left(\frac{\mu_t}{\sigma_k} + \mu\right)\frac{\partial k}{\partial y}$$

$$\frac{\partial \rho k}{\partial t} = -\frac{\partial}{\partial x}\rho U k - \frac{\partial}{\partial y}\rho V k + \rho P - \rho\varepsilon + \frac{\partial}{\partial x}\left(\frac{\mu_t}{\sigma_k} + \mu\right)\frac{\partial k}{\partial x} + \frac{\partial}{\partial y}\left(\frac{\mu_t}{\sigma_k} + \mu\right)\frac{\partial k}{\partial y}$$

where

$$P = \frac{\mu_t}{\rho}\left\{2\left[\left(\frac{\partial U}{\partial x}\right)^2 + \left(\frac{\partial V}{\partial y}\right)^2\right] + \left(\frac{\partial U}{\partial y} + \frac{\partial V}{\partial x}\right)^2\right\}$$

a. Temporal Term

$$\frac{\partial \rho k}{\partial t} = \frac{\rho_{i,j}^{n+1}\, k_{i,j}^{n+1} - \rho_{i,j}^{n}\, k_{i,j}^{n}}{\Delta t}$$

b. Convective Terms (with upwind differencing)

$$\frac{\partial \rho U k}{\partial x} = \begin{cases} \text{if } U > 0 & \dfrac{(\rho U k)_{i,j} - (\rho U k)_{i-1,j}}{\Delta x} \\ \text{if } U < 0 & \dfrac{(\rho U k)_{i+1,j} - (\rho U k)_{i,j}}{\Delta x} \end{cases}$$

$$\frac{\partial \rho Vk}{\partial y} = \begin{cases} \text{if } V > 0 & \dfrac{(\rho Vk)_{i,j} - (\rho Vk)_{i,j-1}}{\Delta y} \\ \text{if } V < 0 & \dfrac{(\rho Vk)_{i,j+1} - (\rho Vk)_{i,j}}{\Delta y} \end{cases}$$

c. Source-Sink Terms

$$\rho P = \rho_{i,j} P_{i,j}$$

$$\rho \varepsilon = \rho_{i,j} \varepsilon_{i,j}$$

d. Diffusion Terms (with central differencing)

$$\frac{\partial}{\partial x}\left(\frac{\mu_t}{\sigma_k} + \mu\right)\frac{\partial k}{\partial x}$$

$$= \frac{\left(\dfrac{\mu_t}{\sigma_k} + \mu\right)_{i+1/2,j} \dfrac{k_{i+1,j} - k_{i,j}}{\Delta x} - \left(\dfrac{\mu_t}{\sigma_k} + \mu\right)_{i-1/2,j} \dfrac{k_{i,j} - k_{i-1,j}}{\Delta x}}{\Delta x}$$

$$\frac{\partial}{\partial y}\left(\frac{\mu_t}{\sigma_k} + \mu\right)\frac{\partial k}{\partial y}$$

$$= \frac{\left(\dfrac{\mu_t}{\sigma_k} + \mu\right)_{i,j+1/2} \dfrac{k_{i,j+1} - k_{i,j}}{\Delta y} - \left(\dfrac{\mu_t}{\sigma_k} + \mu\right)_{i,j-1/2} \dfrac{k_{i,j} - k_{i,j-1}}{\Delta y}}{\Delta y}$$

C.2 <u>ε Transport Equation</u>

$$\frac{\partial}{\partial t}\rho\varepsilon + \frac{\partial}{\partial x}\rho U\varepsilon + \frac{\partial}{\partial y}\rho V\varepsilon$$

$$= c_{\varepsilon_1}\rho\frac{\varepsilon}{k}P - c_{\varepsilon_2}\rho\frac{\varepsilon}{k}\varepsilon + \frac{\partial}{\partial x}\left(\frac{\mu_t}{\sigma_\varepsilon} + \mu\right)\frac{\partial \varepsilon}{\partial x} + \frac{\partial}{\partial y}\left(\frac{\mu_t}{\sigma_\varepsilon} + \mu\right)\frac{\partial \varepsilon}{\partial y}$$

$$\frac{\partial \rho\varepsilon}{\partial t} = -\frac{\partial}{\partial x}\rho U\varepsilon - \frac{\partial}{\partial y}\rho V\varepsilon + c_{\varepsilon_1}\rho\frac{\varepsilon}{k}P - c_{\varepsilon_2}\rho\frac{\varepsilon}{k}\varepsilon$$

$$+ \frac{\partial}{\partial x}\left(\frac{\mu_t}{\sigma_\varepsilon} + \mu\right)\frac{\partial \varepsilon}{\partial x} + \frac{\partial}{\partial y}\left(\frac{\mu_t}{\sigma_\varepsilon} + \mu\right)\frac{\partial \varepsilon}{\partial y}$$

where

$$P = \frac{\mu_t}{\rho}\left\{2\left[\left(\frac{\partial U}{\partial x}\right)^2 + \left(\frac{\partial V}{\partial y}\right)^2\right] + \left(\frac{\partial U}{\partial y} + \frac{\partial V}{\partial x}\right)^2\right\}$$

a. Temporal Term

$$\frac{\partial \rho\varepsilon}{\partial t} = \frac{\rho_{i,j}^{n+1}\,\varepsilon_{i,j}^{n+1} - \rho_{i,j}^{n}\,\varepsilon_{i,j}^{n}}{\Delta t}$$

b. Convection Terms (with upwind differencing)

$$\frac{\partial \rho U\varepsilon}{\partial x} = \begin{cases} \text{if } U > 0 & \dfrac{(\rho U\varepsilon)_{i,j} - (\rho U\varepsilon)_{i-1,j}}{\Delta x} \\ \text{if } U < 0 & \dfrac{(\rho U\varepsilon)_{i+1,j} - (\rho U\varepsilon)_{i,j}}{\Delta x} \end{cases}$$

$$\frac{\partial \rho V\varepsilon}{\partial y} = \begin{cases} \text{if } V > 0 & \dfrac{(\rho V\varepsilon)_{i,j} - (\rho V\varepsilon)_{i,j-1}}{\Delta y} \\ \text{if } V < 0 & \dfrac{(\rho V\varepsilon)_{i,j+1} - (\rho V\varepsilon)_{i,j}}{\Delta y} \end{cases}$$

c. Source-Sink Terms

$$c_{\varepsilon_1}\rho\frac{\varepsilon}{k}P = c_{\varepsilon_1}\left(\rho\frac{\varepsilon}{k}\right)_{i,j}P_{i,j}$$

$$c_{\varepsilon_2}\rho\frac{\varepsilon}{k}\varepsilon = c_{\varepsilon_2}\left(\rho\frac{\varepsilon}{k}\right)_{i,j}\varepsilon_{i,j}$$

d. Diffusion Terms (with central differencing)

$$\frac{\partial}{\partial x}\left(\frac{\mu_t}{\sigma_\varepsilon} + \mu\right)\frac{\partial \varepsilon}{\partial x}$$

$$= \frac{\left(\frac{\mu_t}{\sigma_\varepsilon} + \mu\right)_{i+1/2,j} \frac{\varepsilon_{i+1,j} - \varepsilon_{i,j}}{\Delta x} - \left(\frac{\mu_t}{\sigma_\varepsilon} + \mu\right)_{i-1/2,j} \frac{\varepsilon_{i,j} - \varepsilon_{i-1,j}}{\Delta x}}{\Delta x}$$

$$\frac{\partial}{\partial y}\left(\frac{\mu_t}{\sigma_\varepsilon} + \mu\right)\frac{\partial \varepsilon}{\partial y}$$

$$= \frac{\left(\frac{\mu_t}{\sigma_\varepsilon} + \mu\right)_{i,j+1/2} \frac{\varepsilon_{i,j+1} - \varepsilon_{i,j}}{\Delta y} - \left(\frac{\mu_t}{\sigma_\varepsilon} + \mu\right)_{i,j-1/2} \frac{\varepsilon_{i,j} - \varepsilon_{i,j-1}}{\Delta y}}{\Delta y}$$

C.3 Wall Function Treatment

Wall functions for the modified TWODLE code are obtained using the non-equilibrium wall-functions of Chieng and Launder (Ref. 26) discussed in Section 2.9. However, since TWODLE uses nodal values rather than control volume averages†, some changes were made in implementing these wall functions. A typical near-wall region is shown in Figure C.1. Here it is assumed that node w is at the wall, and w + 1 is in the fully turbulent region

$$\frac{y_{w+1} k_v^{1/2}}{\nu} > 20,$$

where y_{w+1} is the distance from node w + 1 to the wall, and k_v is the turbulent kinetic energy at the edge of the viscous-sublayer, y_v. Following Ref. 26 the wall shear stress T_w can be expressed as

$$T_w = \kappa^* \rho U_{w+1} k_v^{1/2} / \left(\ln E^* \frac{y_{w+1} k_v^{1/2}}{\nu}\right)$$

†Chieng and Launder wall-functions use near-wall cell integration to calculate mean production and dissipation rates for those cells.

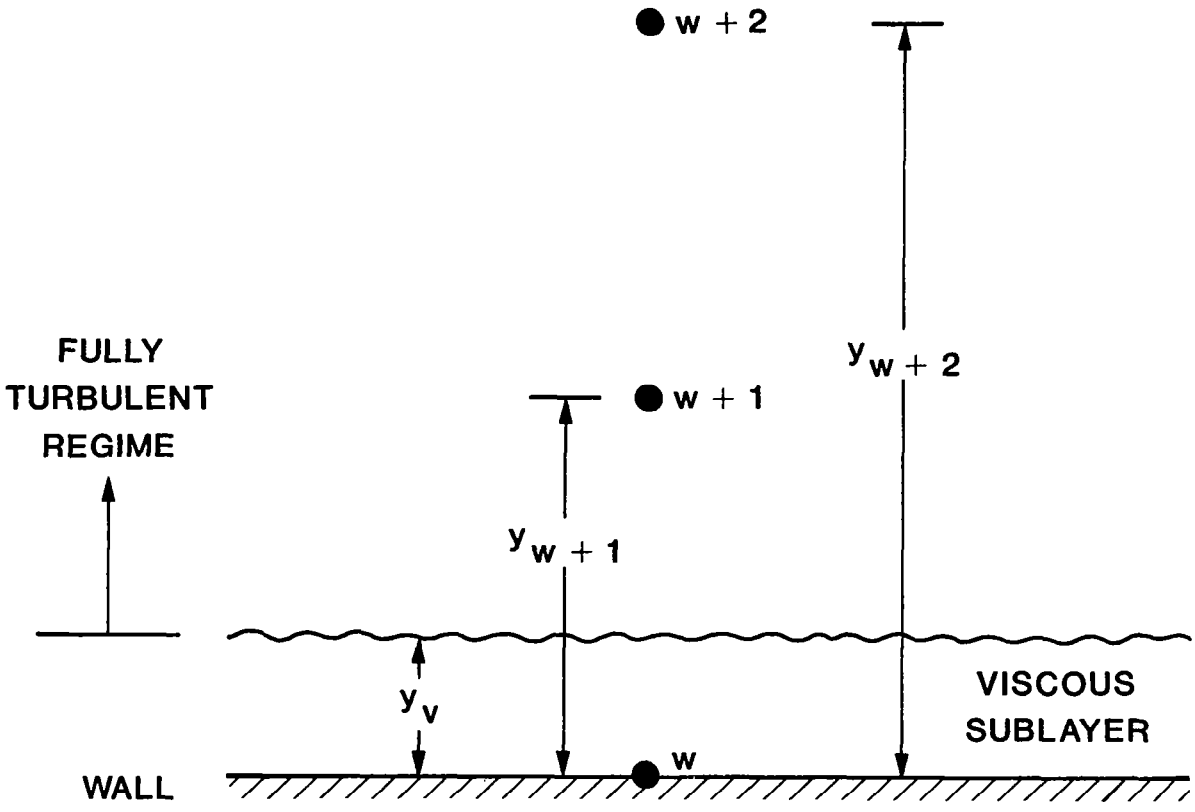

FIGURE C.1. Typical Near-Wall Region.

where $\kappa^* = 0.4187 c_\mu^{1/2}$ and $E^* = e^{\kappa^* Re_v / Re_v}$†. Also the shear stress at node w + 2 by definition is

$$T_{w+2} = \mu_T \left(\frac{\partial U}{\partial y} + \frac{\partial V}{\partial x} \right)_{w+2}$$

If it can be conjectured that the shear stress varies linearly between the wall and node w + 2 (a plausible assumption for most flows with a reasonably fine near-wall grid), the shear stress at node w + 1 can be obtained by interpolating between nodes w and w + 2

$$T_{w+1} = T_w + \frac{(T_{w+2} - T_w)}{(y_{w+2} - y_w)} (y_{w+1} - y_w)$$

Then the turbulent viscosity at w + 1 can be calculated from its definition

$$\mu_{t_{w+1}} = \frac{T_{w+1}}{\left(\frac{\partial U}{\partial y} + \frac{\partial V}{\partial x} \right)_{w+1}}$$

The production rate of turbulent kinetic energy at w + 1 now becomes

$$P_{w+1} = \frac{\mu_{t_{w+1}}}{\rho_{w+1}} \left\{ 2 \left[\left(\frac{\partial U}{\partial x} \right)^2 + \left(\frac{\partial V}{\partial y} \right)^2 \right] - \frac{2}{3} \left(\frac{\partial U}{\partial x} + \frac{\partial V}{\partial y} \right)^2 \right\}_{w+1}$$

$$- \frac{2}{3} k \left(\frac{\partial U}{\partial x} + \frac{\partial V}{\partial y} \right)_{w+1} + \frac{T_{w+1}}{\rho_{w+1}} \left(\frac{\partial U}{\partial y} + \frac{\partial V}{\partial x} \right)_{w+1}$$

and the near-wall dissipation rates are expressed as

$$\varepsilon_{w+1} = k_{w+1}^{3/2} / c_\ell (y_{w+1} - y_w)$$

and

$$\varepsilon_w = 2\nu \left(\frac{k_v}{y_v} \right)^2$$

following Spalding (Ref. 29), and Pope and Whitelaw (Ref. 28), respectively.

---

†The universal viscous-sublayer thickness constant Re_v is assumed to be 20.

1. Report No.	2. Government Accession No.	3. Recipient's Catalog No.
NASA CR-3643		

4. Title and Subtitle	5. Report Date
ASSESSMENT OF TURBULENCE MODELS FOR SCRAMJET FLOWFIELDS	November 1982
	6. Performing Organization Code
7. Author(s)	8. Performing Organization Report No.
M. M. Sindir and P. T. Harsha	SAI-82-038-CHA
	10. Work Unit No.
9. Performing Organization Name and Address Science Applications, Inc. Combustion Science and Advanced Technology Department 9760 Owensmouth Avenue Chatsworth, California 91311	11. Contract or Grant No. NAS1-15988
	13. Type of Report and Period Covered Contractor Report
12. Sponsoring Agency Name and Address National Aeronautics and Space Administration Washington, DC 20546	14. Sponsoring Agency Code

15. Supplementary Notes

Langley Technical Monitor: John Evans

16. Abstract

Turbulence models useful for computation of the flowfields in advanced scramjet combustion systems must account for a variety of phenomena. In this report, an investigation of the behavior of several turbulence models applied to the prediction of aspects of scramjet combustor flows is described. These models include the basic two-equation model, the multiple-dissipation length scale (MDLS) variant of the two-equation model, and the algebraic stress model (ASM). Predictions have been made of planar backward-facing step flows and axisymmetric sudden expansion flows using each of these approaches. Details of the formulation of each of these models are discussed, and the application of the different approaches to supersonic flows is described. A modified version of the ASM is found to provide the best prediction of the planar backward facing step flow in the region near the recirculation zone, while the basic ASM provides the best results downstream of the recirculation. The modified ASM does not provide as good results in axisymmetric flow, but this comparison is possibly affected by numerical diffusion. No advantage of the MDLS approach over the basic two-equation model is observed. Aspects of the interaction of numerical modeling and turbulence modeling as they affect the assessment of turbulence models are discussed.

17. Key Words (Suggested by Author(s))	18. Distribution Statement
Turbulence Modeling Turbulence Mixing Recirculating Flow Numerical Solution Procedures	Unclassified - Unlimited Subject Category 34

19. Security Classif. (of this report)	20. Security Classif. (of this page)	21. No. of Pages	22. Price
Unclassified	Unclassified	138	A07

For sale by the National Technical Information Service, Springfield, Virginia 22161

NASA-Langley, 1982